The Active Wave Packet Injection Diagnostic for Measuring Plasma Dispersion Relations

Sebastián Rojas Mata

A Dissertation
Presented to the Faculty
of Princeton University
in Candidacy for the Degree
of Doctor of Philosophy

Recommended for Acceptance
by the Department of
Mechanical and Aerospace Engineering
Adviser: Professor Edgar Y. Choueiri

September 2020

Abstract

A probe-based diagnostic which uses harmonically-rich wave packets to measure the dispersion relation in low-temperature laboratory plasmas is presented. Dispersion relation measurements provide the necessary experimental verification for theoretical models describing plasma wave physics; however, existing techniques exhibit fundamental and technical drawbacks some of which the Active Wave Packet Injection (AWPI) seeks to address. Using a frequency-domain analysis of ion-saturation-current probe time traces, which uses coherence metrics to identify wave propagation and interferometry to calculate wavenumber as a function of frequency, the AWPI diagnostic is developed to measure dispersion relations simultaneously at multiple frequencies. A comb generating circuit is designed to excite harmonically-rich wave packets by producing tens of harmonics of an input square wave's fundamental frequency.

A proof-of-concept implementation of the diagnostic is used to measure the dispersion relation of electrostatic ion-cyclotron waves in a 250 W magnetized RF plasma source. In an argon plasma, the diagnostic is used to measure the perpendicular propagation and decay of electrostatic ion-cyclotron waves with wavelengths greater than $\sim$ 3 cm and characteristic decay length-scales of 4.5-6 cm. The nearly three dozen simultaneously measured wavenumbers agree with the prediction of a fluid plasma wave model for frequencies spanning 6 harmonics of the ion-cyclotron frequency (20-120 kHz). In a helium plasma, the diagnostic is used to measure the perpendicular and parallel propagation of the same wavemode with perpendicular wavelengths in the 1.4-3 cm range and a roughly constant parallel wavelength of 7.8 cm. Nearly five dozen simultaneously measured wavenumbers agree with the prediction of a kinetic plasma wave model for frequencies spanning 2 harmonics of the ion-cyclotron frequency (400-800 kHz).

Acknowledgements

I would like to acknowledge my advisor, Prof. Edgar Choueiri, for giving me the opportunity to work in the EP lab. I would like to thank my Ph.D. committee members/examiners Prof. Sam Cohen and Dr. Yevgeny Raitses for their time spent discussing my research throughout the years. I would also like to thank Prof. Ben Jorns and Prof. Luc Deike for reading my thesis and providing valuable feedback. I also want to thank Jill Ray and Theresa Russo for the invaluable services they pay to help make grad life better.

I want to thank all my fellow EPPDyL colleagues for your camaraderie in research but really mostly for the vast quantity of inane arguments or discussions we had. Will, thank you for being a great desk neighbor whose jerry-rigging abilities are an artform I admired and benefitted from. Pierre-Yves, thank you for always listening to my experimental woes and odd playlist selections (especially the WPRB madness). Chris and Feldman, thank you for telling me to take Dodin's class and GR, as well as entertaining me with your experimental shenanigans. I also want to thank the various undergrads that did projects in our lab for being as much a source of fresh energy as a source of fresh problems to figure out.

I want to thank my cohort in the MAE Department for the shared experiences across the years. Matt Fu and Christine, moving over to a different coast with friends (and a surprise cat) made life better, yielding quality memories of Panda Express Family Meals, Matt Fu and I sucking at videogames, and Christine feeling bad for Zoe sitting on me. Yao and Yibin, you were great travel buddies but terrible all-you-can-eat sushi buddies. Mark, Clay, and Mike, I can always count on you for Ivy beers and relaxing outdoor fires, whether in a trash can or in a pit. Matthew Edwards and Cody, I guess you were both part of a packaged deal.

I was very lucky to have been part of a department with a great sense of community, particularly as enabled by the Atrium lunch table, Tuesday donuts, 4 pm

coffee/cookie, and free leftover food. From early folks like Tristen, Katie, A J, and Tyler, to latter folks like Danielle, DD, and Madeline, I appreciated the chances offered to relax and recuperate both inside and outside the workplace. Bec, you are an invaluable friend that has taught me a bunch and with whom I've shared many fun experiences (except tasting the oat yogurt). Bruce, we never saw eye-to-eye regarding the sweetness of American food, but could always enjoy whatever weird Oreo flavor came along. Alex, maybe one day you'll finally be 3 for 3 and I won't have anything to chide you for at lunch. Kerry, aprecio tus continuos esfuerzos por aprender mi lengua materna y mi cultura. Vince, we always had something to talk about during lunch, whether others liked it or not. I also want to thank the MAE softball team for the beers, the oranges, and eliminating ORFE from the playoffs that one year.

También quiero agradecer a mi familia por siempre apoyarme en mis estudios y vida lejos de Costa Rica. Mamá, desde joven me inculcaste el valor de la educación y me ayudaste a apreciar lo afortunado que soy de llevar mis estudios a estos límites. Tata, a través de los años me has ayudado a desarrollar mi afán por la ingeniería, las ciencias y las matemáticas para ayudarme ser mejor estudiante, profesor y científico. María, aunque ya sea grande sé que siempre seré 'pitillo' para vos y que siempre estás para poner a prueba mis habilidades de comunicador científico. Genia y Randall, los viajes con ustedes (ya fuera a Singapur o a Atlanta) me proveyeron bien necesitados descansos y chances para chirotear con los güilas en familia. Carmen, gracias a toda la ayuda y el apoyo que me ha prestado desde que fui chamaquillo he logrado apreciar lo que es vivir una vida ordenada y cocinar comida casera.

The research in this dissertation was carried out with the support of the Princeton Writing Program's Quin Morton Teaching Fellowship, the MAE Department's Assistantships in Instruction, the Princeton Plasma Physics Laboratory's (PPPL's) Program in Plasma Science and Technology (PPST), and the Jet Propulsion Laboratory's (JPL's) Strategic University Research Partnership (SURP). This dissertation

carries T#3391 in the records of the Department of Mechanical and Aerospace Engineering.

Para Elena y Marcelo

Contents

List of Tables

List of Figures

List of Symbols

$\perp$	Perpendicular to background magnetic field
$\parallel$	Parallel to background magnetic field
$\hat{a}$	Fourier image of quantity a
a^*	Complex conjugate of quantity a
$a^{[n]}$	Value of quantity a at n^{th} step of an iteration
$\tilde{a}$	Initial guess for value of a
$\mathbf{B}$	Magnetic field, G
c_S	Ion sound speed, m/s
$\mathcal{D}$	Dispersion relation
d	Distance, m
$\mathbf{E}$	Electric field, V/m
$f_{c,\mathrm{i}}$	Ion cyclotron frequency, cycles/s
f_{cut}	Cutoff frequency, cycles/s
f_{i}	Ion velocity distribution function
$f_{\mathrm{i}0}$	Background ion velocity distribution function
$f_{\mathrm{i}1}$	First-order perturbed ion velocity distribution function
$f_{p,\mathrm{i}}$	Ion plasma frequency, cycles/s
f_{RF}	RF frequency, cycles/s
$\mathcal{F}_W$	Windowed discrete Fourier transform
$\mathcal{I}$	Current, A
$\mathfrak{I}$	Integral for Cauchy's Argument Principle
$\mathcal{I}$	Fluorescence intensity
$\mathcal{I}^0$	Background fluorescence intensity
$\mathcal{I}^{IP}$	In-phase fluorescence intensity
$\mathcal{I}^Q$	Out-of-phase fluorescence intensity
I_n	n^{th} order modified Bessel function of the first kind

J_{ex}	Axial electron current density
J_m	m^{th} order Bessel function of the first kind
$\mathbf{k}$	Wavenumber vector, rad/m
$\mathbf{k}_r$	Real component of the wavenumber, rad/m
$\mathbf{k}_i$	Imaginary component of the wavenumber, rad/m
m_{i}	Ion mass, kg
n_{e}	Electron number density, /m^3
n_{i}	Ion number density, /m^3
p	Plasma parameter
$\mathcal{P}$	Pressure, Pa
$\mathcal{P}_{\mathrm{o}}$	Neutral pressure, torr
P_{11}, P_{22}	Autopower spectrum, V^2
P_{12}	Crosspower spectrum, V^2
$\mathcal{R}$	Region of the complex plane
T_{e}	Electron temperature, eV
T_{i}	Ion temperature, eV
u_B	Magnetic drift velocity, m/s
u_{de}	$\mathbf{E}\times\mathbf{B}$ electron drift velocity, m/s
V	Voltage, V
v_A	Alfvén velocity, m/s
$v_{d,\mathrm{i}}$	Ion drift velocity, m/s
v_g	Group velocity, m/s
$\mathbf{v}_{\mathrm{i}}$	Ion velocity, m/s
v_{ph}	Phase velocity, m/s
$v_{th,\mathrm{e}}$	Electron thermal velocity, m/s
$v_{th,\mathrm{i}}$	Ion thermal velocity, m/s
Z	Plasma dispersion function of Fried and Conte

γ	Coherence, rad/s
$\Delta\phi$	Phase difference, rad
θ	Angle of propagation in xy-plane, rad
$\lambda_{D,\mathrm{e}}$	Electron Debye length, m
ν_0	Atomic electron transition frequency, Hz
ν_{DS}	Doppler shifted frequency, Hz
ν_L	Laser frequency, Hz
ρ_e	Electron Larmor radius, m
ρ_i	Ion Larmor radius, m
τ	Mean time between collisions, s
Φ	Electric scalar potential, V
ω	Angular frequency, rad/s
$\omega_{c,\mathrm{e}}$	Electron cyclotron frequency, rad/s
$\omega_{c,\mathrm{i}}$	Ion cyclotron frequency, rad/s
ω_i	Imaginary component of the angular frequency, rad/s
$\omega_{p,\mathrm{e}}$	Electron plasma frequency, rad/s
$\omega_{p,\mathrm{i}}$	Ion plasma frequency, rad/s
ω_r	Real component of the angular frequency, rad/s

Chapter 1

Introduction

1.1 Overview and Motivation

A plasma can sustain numerous plasma wave modes which span orders of magnitude of frequency and wavelength. Unlike in regular fluids, long-range electromagnetic interactions are as important as or even dominant over hydrodynamic interactions in plasma systems, leading to markedly different behaviors. The disparity between ion and electron masses, the anisotropy induced by background magnetic fields, and particle kinetic effects are some of the characteristics particular to plasmas that allow for more complex wave phenomena. This usually means that plasmas are *dispersive* media in which the phase velocity of waves is a function of wave frequency. Plasma wave modes are present in naturally occuring systems, such as electromagnetic ion-cyclotron waves in Earth's outer magnetosphere [1], and play roles in physical processes like the acceleration of ions in Earth's ionosphere [2] or the reconnection of magnetic field lines in the solar corona [3]. On Earth, multiple engineering systems use plasma waves for a variety of purposes: to sustain plasma discharges (e.g. by depositing energy through helicon waves [4, 5, 6]), to heat plasmas (e.g. by selectively coupling to tail electrons with lower-hybrid waves [7, 8]), or to measure plasma proper-

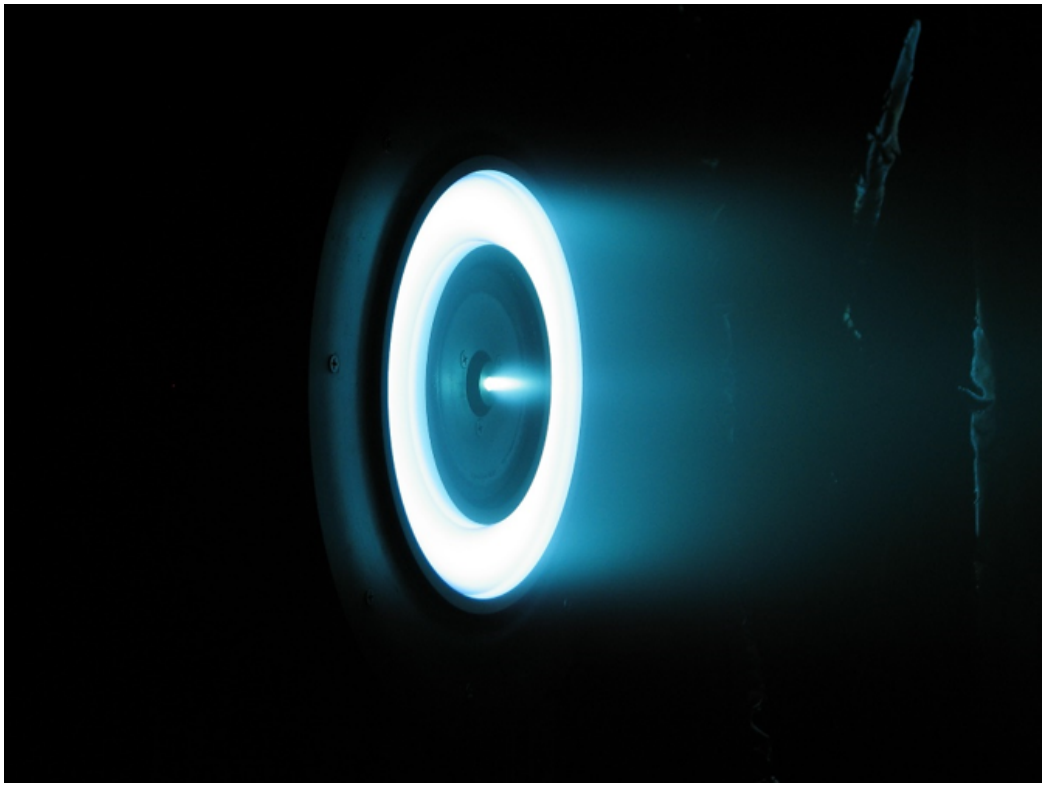

Figure 1.1. Hall effect thruster operating with xenon. Picture courtesy of jpl.nasa.gov.

ties (e.g. by conducting reflectometry of high-frequency electron Langmuir waves [9]). Additionally, unstable plasma wave modes (i.e. instabilities) affect both the theoretical understanding and operation of plasma devices (e.g. instability-induced turbulence in tokamaks [10]).

In the field of electric propulsion, research concerning plasma waves and instabilities is important as these phenomena impact the modeling, design, and certification of plasma thrusters. In particular, the Hall effect thruster (HET), pictured in Fig. 1.1, has been a focus of plasma wave research over the past decades as this device exhibits oscillations in the 1 kHz – 60 MHz frequency range [11] which affect our fundamental understanding of the plasma physics of the discharge. As shown in Fig. 1.2, the Hall effect thruster has an annular channel inside which propellant is ionized and accelerated to generate thrust [12]. The crossed electric and magnetic field ($\mathbf{E} \times \mathbf{B}$) configuration magnetizes electrons emitted by the cathode and causes them to pri-

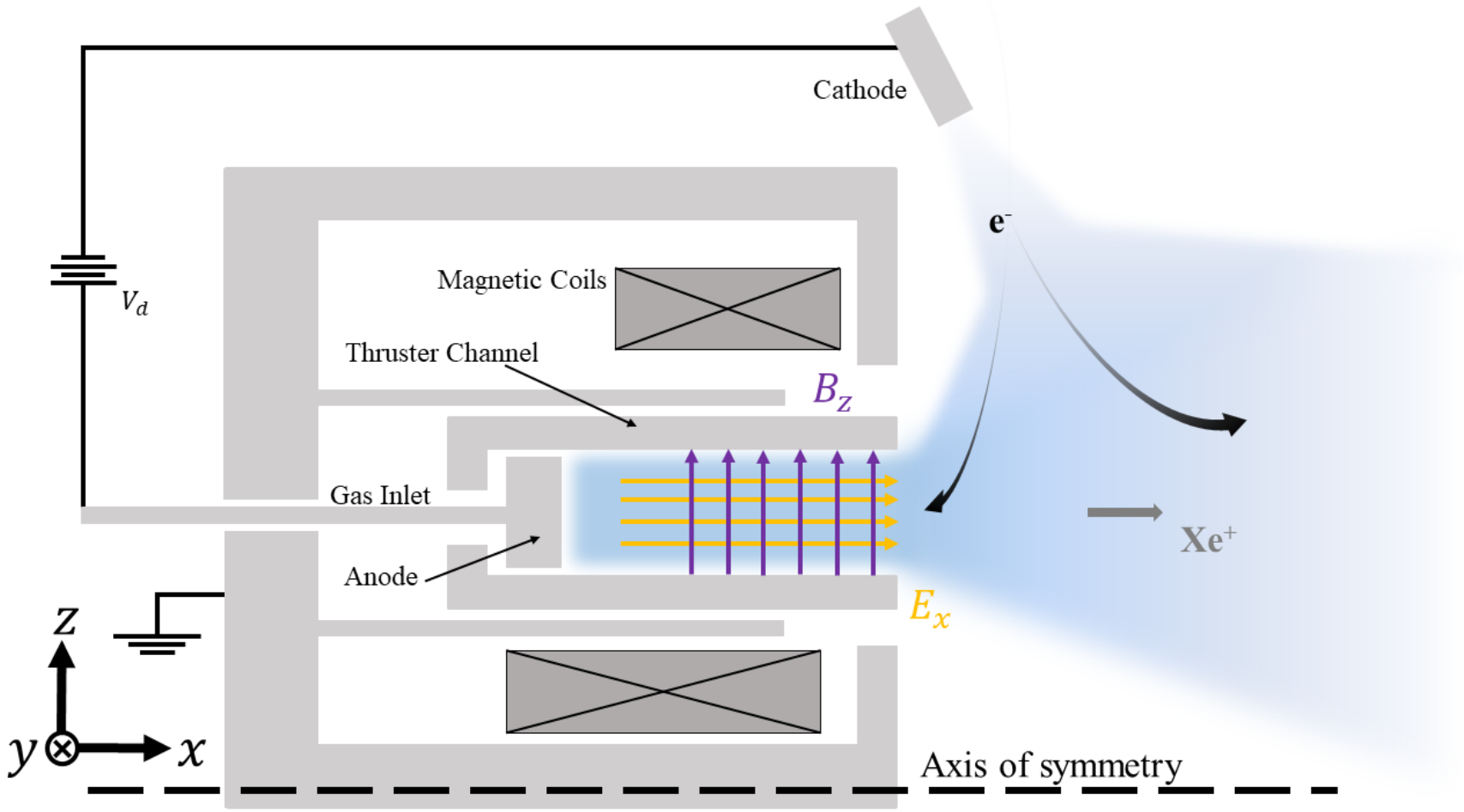

Figure 1.2. Schematic slice of Hall effect thruster

marily drift in the azimuthal direction. Due to their larger mass, the ions are not magnetized and instead are accelerated axially by the electric field, creating an ion plume that is neutralized by a portion of the electrons emitted by the cathode.

While electron motion is mostly confined to the azimuthal $\mathbf{E} \times \mathbf{B}$ direction, there is axial transport across the background magnetic field in order to close the electrical circuit between cathode and anode. The axial electron current density can be written as [13]

$$J_{\mathrm{e}x} = en_{\mathrm{e}} \left(\frac{E_x}{B_z} \right) \frac{1}{\omega_{c,\mathrm{e}}\tau}, \tag{1.1}$$

where n_{e} is the electron number density, E_x is the axial electric field, B_r is the radial magnetic field, $\omega_{c,\mathrm{e}} = eB_r/m_e$ is the electron cyclotron frequency, and τ is the mean time between electron and neutral collisions (the most relevant type of collision for classical cross-field transport). The inverse Hall parameter $1/\omega_{c,\mathrm{e}}\tau$, which is directly proportional to the cross-field electron mobility and axial electron current density, can be calculated using measurements of $J_{\mathrm{e}x}$, n_{e}, E_x, and B_z. However, as exemplified by Fig. 1.3, the measured inverse Hall parameter exceeds the values expected by classical transport models [14, 13], most notably in the region near the channel exit.

Explaining this non-classical or anomalous cross-field electron diffusion [14] which causes the higher-than-expected $J_{\mathrm{e}x}$ and associated electron mobility remains part of ongoing research [15, 16, 17, 18, 19]. So far, numerical simulations of HETs have relied on ad-hoc models of the anomalous transport with free parameters that are adjusted until the simulation matches experimental data [18, 19]. From a theoretical standpoint, it is suspected that plasma oscillations play an important role in the plasma dynamics of the discharge [20, 21, 17], resulting in microturbulence or large-scale structures [22, 23, 24]. Recent work has focused how the electron cyclotron drift instablity could produce enhanced transport in these devices [25, 26, 27, 18]. However,

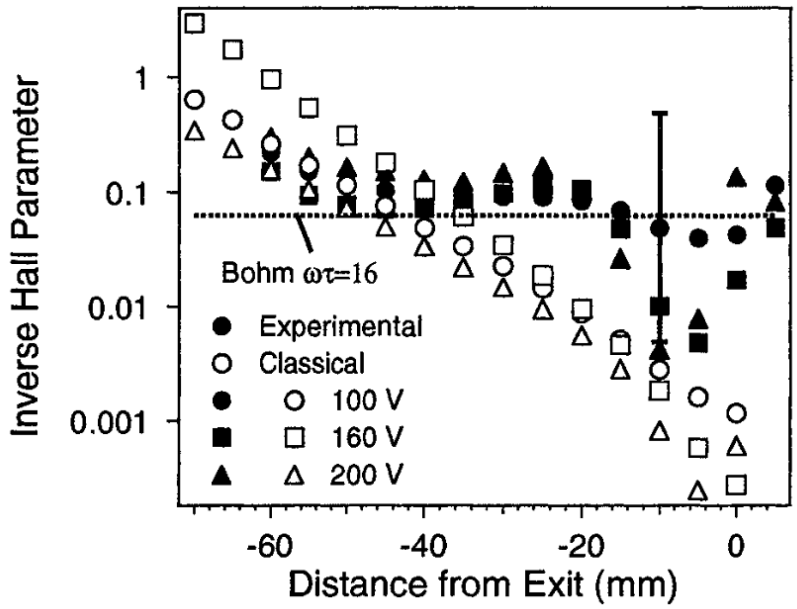

(a) Experimental measurements and classical theory predictions for the inverse Hall parameter, along with Bohm's constant value of 1/16.

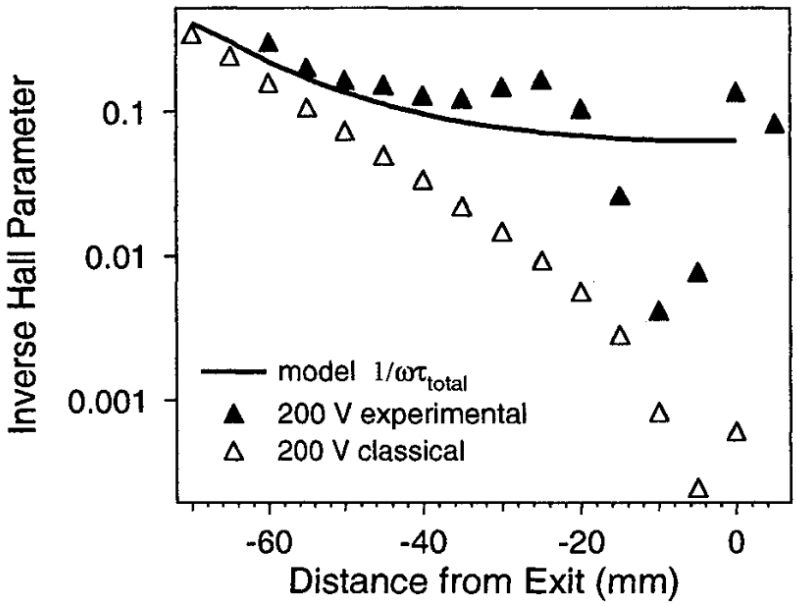

(b) Experimental and classical theory predictions for the inverse Hall parameter, along with Ref. [13]'s improved but still incomplete model.

Figure 1.3. Plots of anomalous transport as represented by the inverse Hall parameter $1/\omega_{c,\mathrm{e}}\tau$, which is proportional to electron mobility. Reproduced from Ref. [13].

Hall effect thrusters are capable of sustaining many different types of oscillations [11] and the results arising from including different wavemodes currently do not allow for "definitive conclusions about the exact physical mechanism responsible for anomolous transport" [18] to be drawn.

Though modeling and understanding (either theoretically or numerically) the effect of plasma waves and instabilities on plasma transport is a challenging task [28, 29, 19], initial steps can be taken by first characterizing the propagation and growth of plasma wavemodes of interest. Quasilinear theory, for example, "include[s] the effects of turbulence self-consistently through anomolous transport terms which depend on the unstable mode or modes and which evolve in time and space as the macroscopic plasma parameters evolve" [30]. This methodology yields turbulence-related terms for particle fluid equations which depend on an instability's propagation (which relates to the wave's frequency and wavelength) and linear growth rate (see, for example, Eqs. 11–13 in Ref. [30]). This vital information is contained in the wavemode's *dispersion relation*, which we discuss in the following section. Deriving explicit expressions for quantities such as linear growth rate from a dispersion relation is unfortunately not always analytically possible without enforcing assumptions that do not reflect the plasma discharges encountered in real propulsion systems (e.g. ignoring plasma parameter gradients or particle kinetic effects). Numerical characterizations of the plasma dispersion relations are therefore necessary to provide the input for advanced transport models like this. Similarly, measuring the plasma wavemodes' dispersion relation provides the needed verification for the models developed.

1.2 The Dispersion Relation

The fundamental concept employed to mathematically describe plasma oscillations (or oscillations in any kind of media) is the *dispersion relation*, commonly written as [31]

$$\mathcal{D}(\omega, \mathbf{k}; p_1, p_2, \ldots) = 0, \tag{1.2}$$

where the function $\mathcal{D}$ relates the wave frequency ω and the wavenumber vector $\mathbf{k}$ to plasma parameters p_i such as electron temperature T_e or background magnetic field $\mathbf{B}_0$. The roots $\omega(\mathbf{k}; p_1, p_2, \ldots)$ or $\mathbf{k}(\omega; p_1, p_2, \ldots)$ of the above function (sometimes referred to as *branches*) represent the allowed wavemodes that may arise in the plasma system which $\mathcal{D}$ models. These roots can be complex, so they are typically written as $\omega = \omega_r + i\omega_i$ or $\mathbf{k} = \mathbf{k}_r + i\mathbf{k}_i$ to distinguish the portion describing propagation (ω_r or $\mathbf{k}_r$) from that describing growth or decay (ω_i or $\mathbf{k}_i$). This interpretation corresponds to expressing a physical quantity that oscillates in space or time due to a wave's presence (such as electron density n_e or electric field $\mathbf{E}$) as

$$a(\mathbf{x}, t) = a_0(\mathbf{x}, t) + a_1 \exp(i\mathbf{k} \cdot \mathbf{x} - i\omega t), \tag{1.3}$$

where $a_0(\mathbf{x}, t)$ is the background value of $a(\mathbf{x}, t)$ and a_1 is the amplitude of the linear perturbation induced by the wave.

The exact form of $\mathcal{D}$ depends on the model chosen to describe the plasma system. For example, using the convention in Eq. 1.3 for ion density n_i, ion velocity $\mathbf{v}_\mathrm{i}$, pressure $\mathcal{P}$, and magnetic field $\mathbf{B}$, we can linearize and combine the ideal magneto-

hydrodynamic (MHD) equations

$$\frac{\partial n_{\rm i}}{\partial t} + \nabla \cdot (n_{\rm i}\mathbf{v}_{\rm i}) = 0, \tag{1.4}$$

$$n_{\rm i} m_{\rm i} \left(\frac{\partial}{\partial t} + \mathbf{v}_{\rm i} \cdot \nabla \right) \mathbf{v}_{\rm i} = \frac{(\mathbf{B} \cdot \nabla)\mathbf{B}}{4\pi} - \frac{\nabla(\mathbf{B} \cdot \mathbf{B})}{8\pi} - \nabla \mathcal{P}, \tag{1.5}$$

$$\frac{\partial \mathbf{B}}{\partial t} = \nabla \times (\mathbf{v}_{\rm i} \times \mathbf{B}), \tag{1.6}$$

$$\left(\frac{\partial}{\partial t} + \mathbf{v}_{\rm i} \cdot \nabla \right) \left(\frac{\mathcal{P}}{n_{\rm i}^{\gamma}} \right) = 0, \tag{1.7}$$

to write the dispersion relation for electromagnetic Alfvén wave modes [32, 33]

$$(\omega^2 - v_A^2 k_\parallel^2) \left[\omega^4 - (v_A^2 + c_S^2) k^2 \omega^2 + v_A^2 c_S^2 k_\parallel^2 k^2 \right] = 0, \tag{1.8}$$

where $v_A = B_0/\sqrt{\mu_0 n_{\rm i} m_{\rm i}}$ is the Alfvén velocity, $c_S = \sqrt{T_{\rm e}/m_{\rm i}}$ is the ion sound speed, and $k_\parallel$ and $k_\perp$ (with $k^2 = k_\parallel^2 + k_\perp^2$) refer to the components of $\mathbf{k}$ in the directions parallel and perpendicular to the background magnetic field, respectively. Closed-form analytical expressions are readily obtainable for the various branches of this dispersion relation.

However, not all dispersion relations can be analytically solved like Eq. 1.8 for $\omega(\mathbf{k})$ or $\mathbf{k}(\omega)$. Such is the case for the general electrostatic dispersion relation for a warm magnetized plasma [31]

$$\begin{aligned} k_\perp^2 + k_\parallel^2 + \sum_{\rm s} \frac{1}{\lambda_{D,{\rm s}}^2} \times \\ \left[1 + \sum_{n=-\infty}^{n=\infty} \frac{(\omega - k_\parallel v_{d,{\rm s}} - n\omega_{c,{\rm s}}) T_{{\rm s}\perp} + n\omega_{c,{\rm s}} T_{{\rm s}\parallel}}{\sqrt{2} k_\parallel T_{{\rm s}\perp}} e^{-b} I_n(b) Z(\zeta_{n,{\rm s}}) \right] = 0, \end{aligned} \tag{1.9}$$

where I_n is the nth order modified Bessel function of the first kind, Z the plasma dispersion function of Fried and Conte,

$$\zeta_{n,{\rm s}} = \frac{\omega - n\,\omega_{c,{\rm s}} - k_\parallel v_{d,{\rm s}}}{\sqrt{2}\, k_\parallel v_{th,{\rm s}}}, \quad b_{\rm s} = \frac{k_\perp^2 v_{th,{\rm s}}^2}{\omega_{c,{\rm s}}^2}, \tag{1.10}$$

$\lambda_{D,\mathrm{s}} = \sqrt{\epsilon_0 T_\mathrm{s}/e^2 n_\mathrm{s}}$ the species Debye length, $v_{th,\mathrm{s}} = \sqrt{T_s/n_\mathrm{s}}$ the species thermal velocity, $v_{d,\mathrm{s}}$ the species drift velocity, and $\omega_{c,\mathrm{s}} = eB/m_\mathrm{s}$ the species cyclotron frequency. Even simplifying this expression for limiting cases like isothermal species ($T_{\mathrm{s}\parallel} = T_{\mathrm{s}\perp}$) or fully magnetized electrons ($b_\mathrm{e} \ll 1$) does not produce analytically tractable results. Numerical techniques are therefore used to successfully solve for the roots of complicated dispersion relations like this.

However, even if analytically or numerically solvable, the models used to derive a particular dispersion relation may integrate assumptions which do not reflect the true nature of the plasma studied. For example, models which assume a homogeneous plasma do not capture the effects spatial gradients of plasma parameters, like those of density [34] or magnetic field [11] in Hall effect thrusters, have on the propagation or stability of wavemodes. Similarly, simpler but more analytically-tractable fluid models can fail to capture modes of propagation which rely on the inclusion of kinetic effects, such as with the neutralized ion Bernstein wave [35, 36]. Experimental measurements of the dispersion relation ultimately provide the necessary verification for the theoretical framework established to understand the plasma wave physics. This can be a challenging undertaking as experimental diagnostics can perturb the state of the plasma, particularly when physical access to the locations is not easy in real plasma systems and devices. Additionally, the advanced equipment sometimes necessary to perform these measurements can present a high financial barrier and have limited compatibility with different gases.

1.3 Thesis Objective and Structure

Motivated by the importance to experimentally characterize plasma wavemodes in engineering devices like plasma thrusters or natural settings like Earth's ionosphere to better understand the underlying physics, this dissertation presents the Active Wave

Packet Injection (AWPI) diagnostic, an experimental diagnostic used to measure dispersion relations in low-temperature laboratory plasmas using harmonically-rich wave packets. We manufacture a prototype of the diagnostic and integrate it into an existing experimental testbed to validate its perfomance. We also complement this experimental investigation with numerical characterizations of relevant plasma wave-modes using the **P**lasma **R**ocket **In**stability **C**haracterize**r** (PRINCE), a numerical software which solves for the roots of arbitrary dispersion relations over a versatile and customizable parameter space.

We begin in Chapter 2 with a review of existing techniques for measuring plasma dispersion relations along with a discussion of the procedure for numerically solving for the roots of dispersion relations. Chapter 3 details the relevant signal analysis methodologies and hardware implementation of the AWPI diagnostic, which result in the successful generation of harmonically-rich wave packets in the 1-1000 kHz frequency range. We describe in Chapter 4 the low-temperature magnetized RF plasma source in which we implement the AWPI diagnostic to measure the dispersion relation of electrostatic ion-cyclotron (EIC) waves. We discuss our results in Chapter 5, followed by concluding remarks in Chapter 6.

Chapter 2

Review of Existing Techniques

In this chapter we overview existing experimental techniques for measuring dispersion relations. We first discuss the difference between passive and active probing of a plasma. We then briefly describe the physics behind three common techniques: plasma-immersed probe interferometry, laser-induced fluorescence, and collective light scattering. We note both strengths and weaknesses of each technique to contextualize and motivate the development of the AWPI diagnostic. We also include a discussion of typical procedures to numerically solve for the roots of dispersion relations and the difficulties that arise due to the nonlinear nature of the complex functions commonly encountered in plasma physics. This is an important task to overview as it enables the direct comparison of theory to measurements and provides some of the background for the PRINCE software described in the appendices.

2.1 Measuring Plasma Dispersion Relations

Various techniques exist to experimentally characterize the spatial and temporal spectra of different plasms parameters. Depending on the plasma system studied, naturally excited plasma waves can produce sufficiently strong signals for passive diagnostics to detect or 'listen' to. Sometimes, though, the plasma modes of interest

may not be naturally excited or, if they are, do not produce signals that rise above background measurement noise, resulting in low signal-to-noise ratio (SNR) measurements which require additional processing to extract meaningful information [37, 20]. In these cases, antennae of various geometries are implemented alongside the passive diagnostics to actively inject waves into the plasma [38, 36, 39, 40] (a procedure not unique to plasma wave investigations, but also for objectives such as discharge creation [41, 42, 6] or plasma heating [8, 43]). This active injection of waves 'rings' the plasma to capture both the phase and growth components of the linear dispsersion relation, which can be obscured once naturally excited modes reach the saturation stage. Past active injection experiments have generally been limited to single- or dual-frequency wave launching [44, 36, 40, 45], so the dispersion relation is measured one frequency at a time. In the following sections we briefly review three techniques which measure dispersion relations of naturally excited or actively injected plasma waves.

2.1.1 Plasma-Immersed Probe Interferometry

Probe interferometry relies on the cross-correlation of the time-dependent voltage or current traces of two or more probes physically immersed in a plasma at known locations [46, 37]. Using a single probe or probes outside the plasma usually only provides information on the frequency spectrum of the oscillations; measuring the dispersion relation requires insight into the spatial structure of the waves. The probes implemented measure a physical quantity which the plasma wave causes to vary in time, such as ion-saturation-current probes to measure n_{i} [36, 40, 47, 20] or magnetic induction probes (also called **B**-dot probes) to measure **B** [48, 49]. At a given frequency ω, the real part of the wavenumber in the direction parallel to the line between the

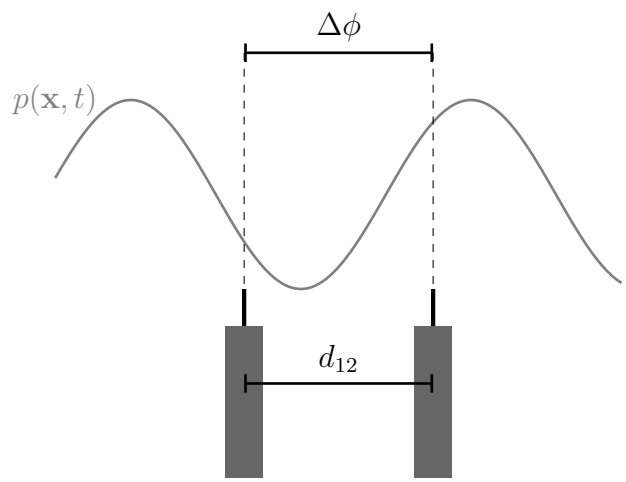

Figure 2.1. Two probes immersed in the plasma take time traces of the value of the oscillating plasma parameter $p(\mathbf{x}, t)$ at two known spatial locations.

two probe tips is

$$k_r = \frac{\Delta\phi}{d_{12}}, \tag{2.1}$$

where $\Delta\phi$ is the phase difference between the two probe signals and d_{12} is the distance between the probes. The relative signal between the probe signals also provides information on the growth or decay of the wave mode (i.e. k_i). Though simple to implement, the probes may alter the state of the plasma by locally cooling both neutral and charged species in high-density discharges, leading to lower temperatures or higher densities [50]. Even in low-density discharges, plasma sheath effects and the electrical biasing of the probes (in the case of particle flux probes) require careful consideration to correctly determine bulk plasma properties [9]. The physical scale of the probes and the possibility of sheath overlap set limits on the smallest resolvable spatial scales, which usually lie in the millimeter range (k less than ~ 650 /m) [51, 27]. A more detailed discussion of the signal analysis involved in this technique is presented in Section 3.1 as it serves as the basis for our AWPI diagnostic.

2.1.2 Laser-Induced Fluorescence

The non-intrusive laser-induced fluorescence (LIF) technique measures the background (f_{i0}) and first-order perturbed (f_{i1}) ion velocity distribution functions (IVDFs) by exploiting forced and spontaneous atomic electron transitions in the ion population [9, 52, 53]. A laser excites bound electrons to a metastable state in order to measure the intensity of the induced fluorescence from the subsequent spontaneous relaxation. If the perturbation f_{i1} is due to a traveling plasma wave, measuring the background ($\mathcal{I}^0$), in-phase ($\mathcal{I}^{IP}$) w.r.t. the plasma wave's phase, and out-of-phase or quadrature ($\mathcal{I}^Q$) components of this fluorescence as a function of laser frequency provides a way to determine the plasma wave's dispersion relation. This technique has been used, for example, to measure the parallel and perpendicular wavenumbers of electrostatic ion-cyclotron waves in linear magnetized RF plasma sources [54] or as part of investigations concerning plasma heating through beating electrostatic waves [55, 56].

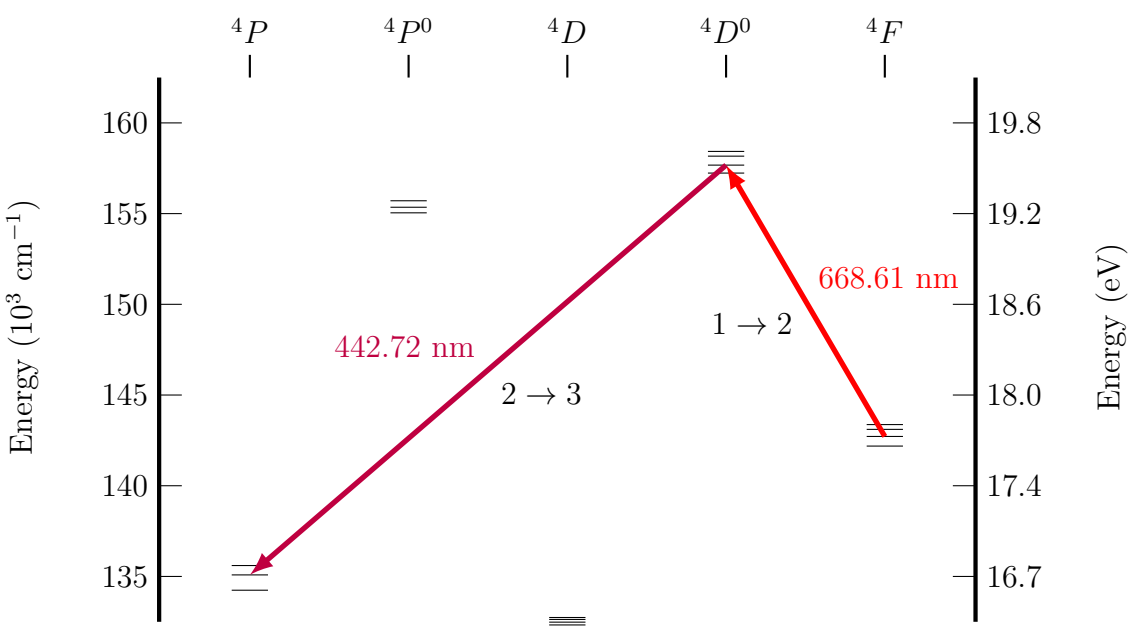

Figure 2.2. In this example Ar II scheme, the laser induces the atomic electron transition $1 \rightarrow 2$ (red). The fluorescence emitted by the relaxation $2 \rightarrow 3$ (purple) is measured. Diagram developed based on Refs. [57, 58, 53].

The atomic electron transitions for the forced excitation and spontaneous relaxation used in gas-specific LIF schemes involve easily distinguishable light wavelengths so that the input laser light does not interfere with the fluorescence measurement [52, 59, 53, 60, 61, 62]. Fig. 2.2 depicts one such example scheme for singly-charged argon ions which works with radiation in the visible spectrum. Laser light whose frequency ν_L matches the atomic electron transition frequency ν_0 (in this case corresponding to a wavelength of 668.61 nm) excites electrons from the stable $3d^4F_{7/2}$ state (1) to the metastable $4p^4D^0_{5/2}$ state (2). The excited electrons spontaneously relax from this metastable state to the stable $4s^4P_{3/2}$ state (3) by emitting fluorescent radiation at a frequency different than ν_0 (in this case corresponding to a wavelength of 442.72 nm). However, since the ion population has a non-zero temperature that gives the ion velocity distribution function a finite width, only a fraction of the ion population undergoes this process. Ions with velocity v_i parallel to the the laser beam encounter a Doppler shifted laser frequency

$$\nu_{DS} = \nu_L \left(1 + \frac{v_\mathrm{i}}{c}\right), \tag{2.2}$$

so only those with $v_\mathrm{i} = 0$ experience the transition $1 \rightarrow 2$ when the laser is tuned to ν_0. Ions with non-zero v_i along the laser scanning axis require $\nu_L = \nu_{DS}$ for excitation, which in the non-relativistic limit $|v_\mathrm{i}/c| \ll 1$ yields the relation

$$v_\mathrm{i} = \frac{c}{\nu_0}(\nu_L - \nu_0) \tag{2.3}$$

between ion velocity and laser frequency. Sweeping ν_L about ν_0 excites different portions of the ion population, allowing the optically-measured fluorescent intensities mentioned above to be correlated with ion velocities. Solutions to the ion Vlasov equation perturbed with either an electrostatic wave's potential $\mathbf{E}_1 = -i\mathbf{k}\Phi_1 \exp(i\mathbf{k} \cdot \mathbf{x} - i\omega t)$ or an electromagnetic wave's fields $\mathbf{E}_1$ and $\mathbf{B}_1$ such that $\mathbf{k} \times \mathbf{E}_1 = \omega \mathbf{B}_1$ [63]

are fit to the fluorescent intensity measurements to calculate the wave ω and $\mathbf{k}$. The full data-reduction procedure for the case of an electrostatic wave is described in Appendix A (see Refs. [54, 55, 63] as well); the case of an electromagnetic wave is covered in Ref. [63].

While attractive for its non-intrusive nature, the LIF technique takes measurements at a single spatial location in the plasma and uses the dispersion relation from Eq. 1.9 or its electromagnetic equivalent to provide closure for the fitting procedure of the data [54, 63]. These dispersion relations do not include the effects of plasma parameter gradients, which may be relevant in real plasma devices [64, 11, 65]. Additionally, the diagnostic involves costly equipment and two optical lines-of-sight access points to the plasma volume, making it challenging to implement. Its reliance on fluorescence makes it incompatible with certain gases (e.g. He II) and can limit a particular laser system's applicability to multiple gases.

2.1.3 Collective Light Scattering

Another non-intrusive technique, collective light scattering scatters laser light off oscillating plasma electrons to measure the frequency spectrum of electron plasma waves with a wavenumber vector defined by the scattering geometry [66]. In addition to dispersion relation measurements, this diagnostic can provide information on the form factor, amplitude, and spatial distribution of electron density fluctuations [67]. This diagnostic has been used in particular to investigate the $\mathbf{E} \times \mathbf{B}$ electron drift instability in Hall effect thrusters [67, 68, 25].

Free electrons undergoing oscillatory motion in the plasma scatter incident laser light with wavenumber vector $\mathbf{k}_{inc}$. The scattered light has a wavenumber vector $\mathbf{k}_{sc}$ which, as shown in Fig. 2.3, is at an angle α with respect to $\mathbf{k}_{inc}$. The signal of this scattered light depends on α and the associated analyzing wavenumber $\mathbf{k} = \mathbf{k}_{sc} - \mathbf{k}_{inc}$; measuring this scatterred light provides information on the spatial

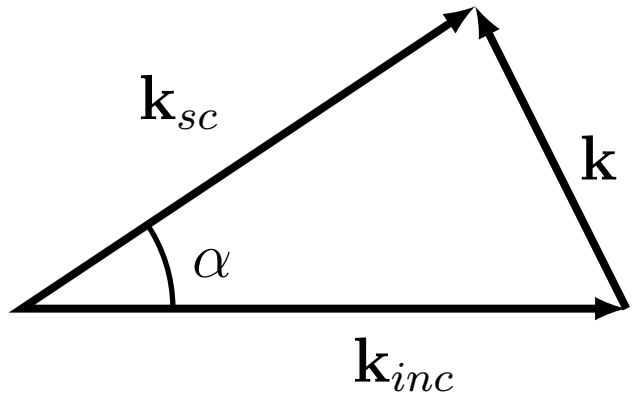

Figure 2.3. Scattering by electrons of incident light with wavenumber vector $\mathbf{k}_{inc}$ produces light with wavenumber vector $\mathbf{k}_{sc}$. Measurements of the spatial Fourier transform of electron density at different $\mathbf{k} = \mathbf{k}_{sc} - \mathbf{k}_{inc}$ are taken by varying the angle α or by rotating the scattering plane. Based on Ref. [67].

Fourier transform of the electron density at that $\mathbf{k}$ [67, 68]. Varying α or rotating the scattering plane as a whole allows for measurements at different values of $\mathbf{k}$. Recording the time-dependent scattered light signal using a superheterodyne optical interference technique provides information on the temporal Fourier transform of the electron density, yielding a measurement of the wave frequency ω as a function of the geometry-defined $\mathbf{k}$.

The full mathematical details of the collective light scattering diagnostic are presented in Ref. [67]. Similar to the LIF technique, collective light scattering requires costly equipment and optical access to the plasma volume, also making its implementation challenging. Alignment and equipment constraints have only allowed for probing wavenumbers greater than ~ 4000 /m at frequencies in the MHz range [67, 68, 25], so the ability of this technique to measure low-frequency or long-wavelength wavemodes is not certain. Moreover, since the scattering is due to fluctuations in the electron density, only compressible electrostatic wavemodes can be detected with this method.

2.2 Numerically Characterizing Plasma Dispersion Relations

Measurements taken by the above techniques are commonly compared to numerical solutions $\omega(\mathbf{k})$ or $\mathbf{k}(\omega)$ which satisfy Eq. 1.2 to validate theoretical plasma models. This entails finding the complex roots of an analytic (or meromorphic at worst) function over a multidimensional complex space. This task is commonly faced across multiple disciplines, ranging from pure or applied mathematics [69, 70, 71, 72] to various engineering fields [73, 74, 75]. Since a dispersion relation fundamentally describes oscillatory motion in a medium, numerically finding its roots in different configurations of varying media has been widely researched [76, 77, 78, 79, 80]. Given that dispersion relations many times are nonlinear functions, one strategy to simplify the problem is to construct a complex polynomial which has the same roots as the nonlinear function and pass this to a variety of efficient polynomial-root solvers [69, 70]. Alternatively, if this is not an adequate or viable simplification to perform, a common tactic is to use root-finding algorithms that can handle nonlinear functions, such as Newton-Raphson's method or the secant method [81, 82]. Typically, methods like these require the input of one or more values near the root (i.e. initial guesses) to initiate an iterative procedure which eventually convergences to the 'true' value (i.e. within numerical tolerance) of the root. While these methods generalize to higher dimensions [82], it is nevertheless common to reduce the dimensionality of the input variable space when searching for the roots of dispersion relations in plasma physics. For example, $\mathbf{k}$ components are rewritten as functions of just one $\mathbf{k}$ component (e.g. $k_y = k_y(k_x)$ and $k_z = k_z(k_x)$), removed by considering limiting cases (e.g. $k_\perp \to 0$ for purely parallel propagation), or, if possible, grouped into nondimensional variables (e.g. $k_\perp/k_\parallel$) [83, 84, 35, 31, 11, 40, 34]. Usually two independent variables remain, one of which is iterated over N steps (e.g. $k_x \in \left[k_x^{[0]}, k_x^{[1]}, \ldots, k_x^{[N-1]}\right]$)

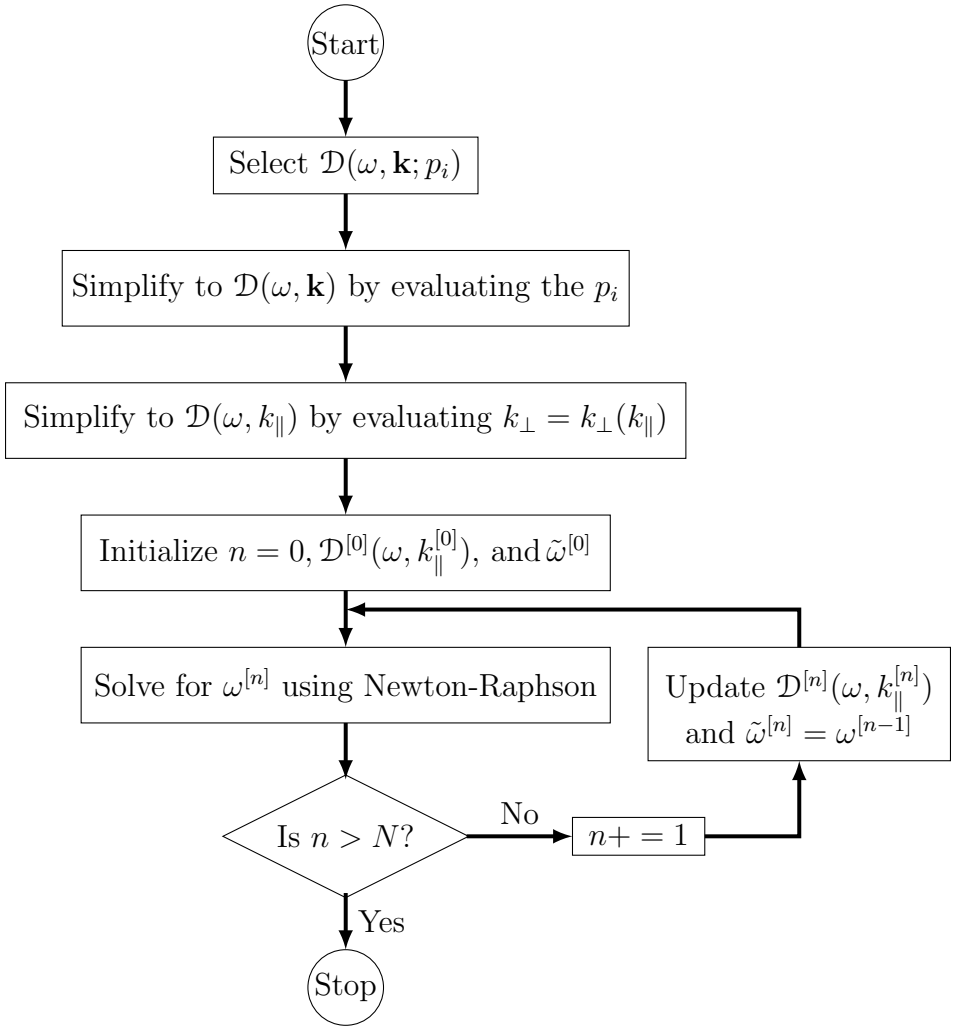

Figure 2.4. An example procedure for numerically characterizing a branch $\omega(k_\parallel)$ of the function $\mathcal{D}(\omega, \mathbf{k}; p_i)$. There are N discrete values of $k_\parallel$ for which we want to find an ω using an initial guess $\tilde{\omega}$ such that Eq. 1.2 is satisfied.

and the other which is the root sought (e.g. ω such that $\mathcal{D}^{[n]}(\omega, k_x^{[n]}) = 0$), where the superscript $[n]$ denotes evaluation at the n-th step of the iteration. Fig. 2.4 depicts the steps for an example procedure where the goal is to compute $\omega(k_\parallel)$.

As intricate as finding the complex root of a single-variable nonlinear function already is (a task "equivalent to finding the vector roots of a system of two nonlinear equations" [85]), a further difficulty arises if multiple roots of the dispersion relation are present in the region of $(\omega, \mathbf{k})$-space studied, which is not uncommon for dispersion relations in plasma physics [35, 31]. Determining the number and potential location

of these roots *a priori* is not trivial, complicating the choice of adequate initial values to input into root-finding algorithms. Additionally, even if the number of roots is somehow known, which root an iterative root-finding algorithm converges to can be a highly sensitive or even chaotic function of the input values, giving the algorithms poor global convergence properties [82]. As Fig. 2.5 illustrates, even functions as simple as complex polynomials exhibit undesired behavior if we feed a poor initial guess to an algorithm like Newton-Raphson. This means that resolving the desired branch of a dispersion relation could involve time-consuming sweeps over the input parameter space. Previous work has tried to address this complication by plotting the contours $\mathrm{Re}\,(\mathcal{D}(\omega, \mathbf{k})) = 0$ and $\mathrm{Im}\,(\mathcal{D}(\omega, \mathbf{k})) = 0$ over a region in $(\omega, \mathbf{k})$-space to identify where they intersect and thereby provide the initial guess for the root [81, 85]. A similar graphical strategy uses the argument of $\mathcal{D}(\omega, \mathbf{k})$ to generate a slope field plot in the complex plane and locate 'vortices' which encircle the roots [86, 87]. Both of these methods require (1) active human input, which can become inconvenient for investigations over larger spans of the p_i and $(\omega, \mathbf{k})$-space, and (2) repeated evaluation of $\mathcal{D}$ at unneeded locations in the complex plane, which becomes computationally costly for more advanced dispersion relations.

Instead, it is desirable to develop an automated procedure to numerically characterize the roots of arbitrary dispersion relations. Provided a specific dispersion relation $\mathcal{D}(\omega, \mathbf{k}; p_i)$ along with a set of p_i and the search region in $(\omega, \mathbf{k})$-space, two goals should be accomplished autonomously:

1. Global root-finding: Determine the number and initial location of all roots in the relevant search region.

2. Local root-tracking: Track the location of each root as the specified iteration variable varies.

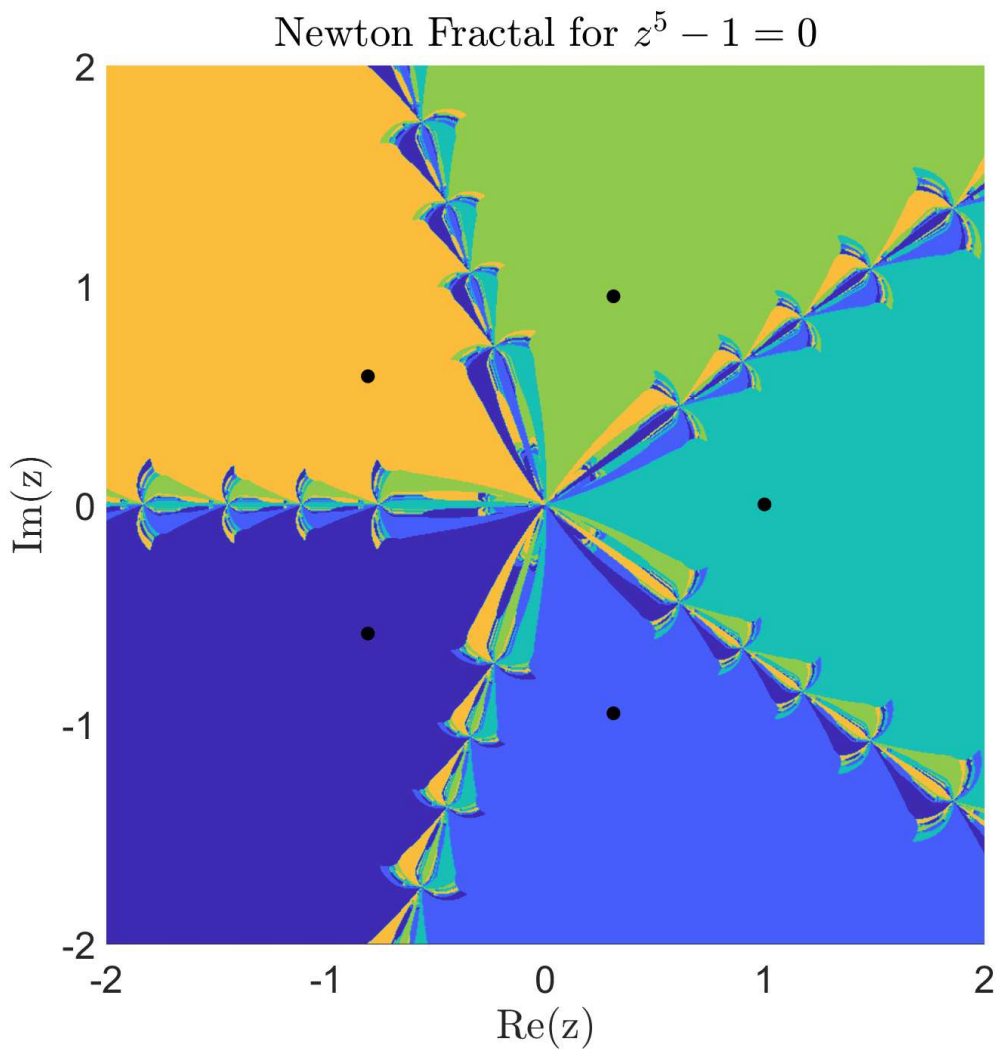

Figure 2.5. Newton fractal generated by searching for the roots of the polynomial $z^5 - 1$ using the Newton-Raphson method. The five different colors correspond to the five different roots the iteration converges to given the initial guess. The black dots depict the location of the five roots.

The nonlinear nature of dispersion relations in plasma physics especially complicates the first of these goals. Successfully accomplishing it mitigates several issues that can arise when carrying out the second goal; the numerical algorithms and PRINCE software described in Appendices B and C, respectively, are designed to have better global convergence propoerties than previous techniques in order to achieve this.

2.3 Chapter Summary

The experimental techniques reviewed in this chapter showcase the trade-off between the simplicity (both in terms of analysis and hardware implementation) and the intrusiveness of diagnostics for measuring plasma dispersion relations. The AWPI diagnostic we develop in Chapter 3 opts for simplicity but integrates waveform shaping into the signal design to provide more expedited measurement capabilities than previous intrusive diagnostics. We also overviewed several existing techniques for numerically solving for the roots of dispersion relations to provide background for the PRINCE software which we use to provide complementary numerical characterizations of the wavemodes we measure using the AWPI diagnostic.

Chapter 3

Active Wave Packet Injection Diagnostic[1]

In this chapter we describe the Active Wave Packet Injection (AWPI) diagnostic, an active diagnostic which emits harmonically-rich wave packets in a plasma in order to measure dispersion relations. We overview the frequency-space interferometric signal analysis for calculating wavenumbers as a function of wave frequency. We describe the manufacture of an AWPI diagnostic for use in a low-temperature plasma source, which involves the design of a harmonic comb generating circuit, an antenna, and receiver ion-saturation-current probes. The diagnostic produces dozens of harmonics of an input square wave's fundamental frequency in the 1-1000 kHz range.

3.1 Overview of Methodology

Active wave injection systems for measuring plasma dispersion relations have consisted of an emitter probe or antenna along with two or more receiver ion-saturation-

[1]This chapter is based on work being prepared to be submitted for publication and previously presented in [88]: Rojas Mata, S. and Choueiri, E.Y., "Plasma Dispersion Relation Measurements through Active Injection of Wave Packets," *36th International Electric Propulsion Conference*, Vienna, 2019.

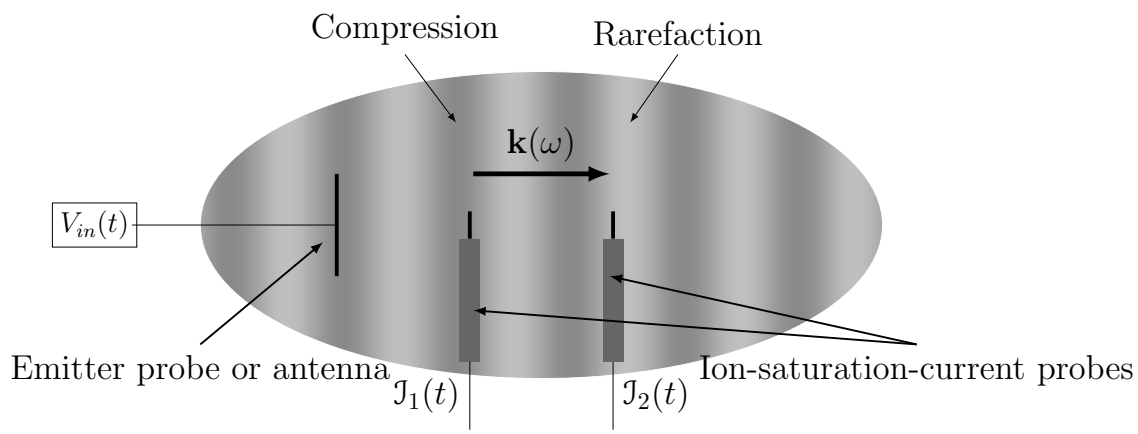

Figure 3.1. The antenna excites traveling compressions and rarefactions of plasma density which result in time-dependent ion-saturation-current traces recorded by the receiver probes downstream.

current probes [89, 36, 86, 40]. In Fig. 3.1 we show an example system with an antenna and two receiver probes immersed in the plasma. The system can be generalized to contain more receiver probes, so that each pair of receiver probes measures the wavenumber along the direction parallel to the line joining their tips. Additionally, as mentioned in Section 2.1.1, other kinds of probes such as **B**-dot probes can be used as needed to measure the relevant plasma parameter. For the case of electrostatic waves, a time-dependent voltage signal $V_{ant}(t)$ sent to the antenna excites the wave and causes traveling compressions and rarefactions of plasma density to pass by the receiver probes located downstream. Control over the harmonic content of $V_{ant}(t)$ allows targeting of the expected frequency range (e.g. from theory or numerical simulation) of the plasma wave mode in question.

Analysis of the current traces $\mathcal{I}_1(t)$ and $\mathcal{I}_2(t)$ provides information about the wavenumber $\mathbf{k}$ as a function of the wave frequency ω. Though previous work used sinusoidal excitations and our AWPI diagnostic uses harmonically-rich excitations, the frequency-domain analysis to measure the dispersion relation we use is applicable to both. To identify coherent wave propagation over background random noise in the signals recorded, we compute spectrum and correlation estimates of the digitally

recorded $\mathcal{I}_1(t_n)$ and $\mathcal{I}_2(t_n)$. We follow a nonparametric signal processing procedure similar to Welch's method for estimating power spectral densities [90] to produce estimates of auto- and crosspower spectra as well as an estimate of the coherence spectrum between two probe signals [46, 91, 92].

3.1.1 Estimation of Power and Coherence Spectra

Assume the data sets of the recorded current traces $\mathcal{I}_1(t_n)$ and $\mathcal{I}_2(t_n)$ are of length N points. Since we want a measure of the variance in the power spectra (i.e. provide error bars for the measurements), we do not calculate spectra of the entire N-long data set. Instead, we divide each set into S equal subsets of length M points to produce the sets $\{\mathcal{I}_{1,1}, \mathcal{I}_{1,2}, \ldots, \mathcal{I}_{1,j}\}$ and $\{\mathcal{I}_{2,1}, \mathcal{I}_{2,2}, \ldots, \mathcal{I}_{2,j}\}$, $j \in [1, S]$. Using several shorter data sets allows us to calculate the signals' variance and decrease the effect of random noise, but comes at the cost of increased frequency increments $\Delta f = f_n - f_{n-1}$ in the spectra (and thus increased spectral 'leakage') [92, 91]. To partially mitigate this, we overlap successive data segments by 50% as pictured in Fig. 3.2 so that we can construct longer subsets than if there was no overlap. Such overlap of data subsets is the distinguishing factor of Welch's method [90], while the specific amount of overlap is a common recommendation in the signal processing literature [91, 92].

We then take the windowed discrete Fourier transform

$$\hat{\mathcal{I}}_{1,j}(f_n) = \mathcal{F}_W\{\mathcal{I}_{1,j}(t_n)\} \quad \text{and} \quad \hat{\mathcal{I}}_{2,j}(f_n) = \mathcal{F}_W\{\mathcal{I}_{2,j}(t_n)\} \tag{3.1}$$

of each data subset. We use a Hanning window "since it provides a good compromise between amplitude accuracy and frequency resolution" [92]. We calculate the autopower spectra P_{11}, P_{22} of the current traces $\mathcal{I}_1$ and $\mathcal{I}_2$ by averaging over the au-

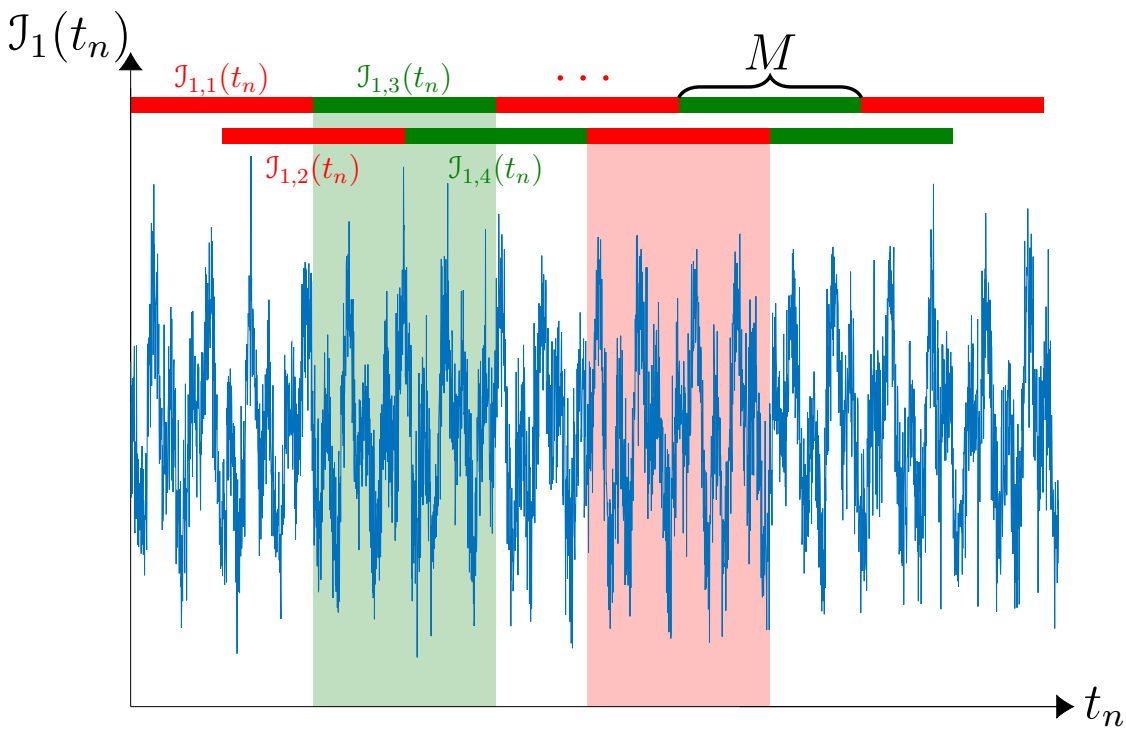

Figure 3.2. For each current trace we generate overlapping data subsets of length M whose extent is illustrated above by the red and green bars. Using more subsets gives better error estimates but a larger frequency increment for the spectra.

topower spectra of the data subsets, so that

$$P_{11}(f_n) = \frac{A}{S}\sum_{j=1}^{S}\hat{\mathcal{I}}^*_{1,j}(f_n)\hat{\mathcal{I}}_{1,j}(f_n) \quad \text{and} \quad P_{22}(f_n) = \frac{A}{S}\sum_{j=1}^{S}\hat{\mathcal{I}}^*_{2,j}(f_n)\hat{\mathcal{I}}_{2,j}(f_n), \tag{3.2}$$

where

$$A = \frac{1}{M^2 P_W^2} \quad \text{with} \quad P_W = |\mathcal{F}_W\{1\}| \tag{3.3}$$

is an amplitude correction factor to account for the power of the window P_W. Similarly, we compute the crosspower spectrum

$$P_{12}(f_n) = \frac{A}{S}\sum_{j=1}^{S}\hat{\mathcal{I}}^*_{1,j}(f_n)\,\hat{\mathcal{I}}_{2,j}(f_n) \tag{3.4}$$

and a normalized version of it called the coherence spectrum

$$\gamma_{12}(f_n) = \frac{P_{12}(f_n)}{\left[P_{11}(f_n)P_{22}(f_n)\right]^{1/2}}, \tag{3.5}$$

both of which provide information about correlated signals present in the probes. Specifically, the magnitude of the coherence spectrum measures how linearly related the two probe signals are, with $|\gamma_{12}| = 0$ denoting no relation and $|\gamma_{12}| = 1$ denoting a complete linear relation. We consider wave propagation to be coherent when $|\gamma_{12}| > 0.95$ and its error is less than 0.05. Note that, if instead of using estimates of the spectra in Eq. 3.5 we used the actual spectra of the N-long data sets, then $|\gamma_{12}| = 1 \,\forall\, f_n$ and we could not identify coherent wave propagation over random noise.

3.1.2 Dispersion Relation Measurement

The real wavenumber spectrum of coherently propagating waves is

$$k_r(f_n) = \frac{\mathrm{Arg}\{P_{12}(f_n)\}}{d_{12}}, \tag{3.6}$$

where d_{12} is the distance between the two receiver probes. The imaginary wavenumber spectrum, which represents spatial growth or decay, is given by

$$k_i(f_n) = -\frac{1}{2d_{12}} \log\left[\frac{P_{22}(f_n)}{P_{11}(f_n)}\right]. \tag{3.7}$$

We can also calculate the phase and group velocities

$$v_{ph} = \frac{\omega}{k_r} \quad \text{and} \quad v_g = \frac{d\omega}{dk_r}. \tag{3.8}$$

3.2 Harmonic Comb Generating Circuit

For sinusoidal excitations in a plasma, $\gamma_{12} = 1$ just for one value of f_n (the wave driving frequency), so the data acquisition and analysis would have to be repeated mutliple times for different driving frequencies to produce multiple measurements of k_r ad k_i. We seek to expedite the process by sending harmonically-rich excitation signals to the diagnostic's antenna, which can be particularly advantageous in pulsed plasma experiments [93, 86]. We therefore construct a circuit capable of producing dozens of harmonics with comparable amplitudes of a fundamental frequency to excite and record coherent wave packets (i.e. $\gamma_{12} = 1$ for multiple values of f_n) instead of a single coherent wave in the plasma.

We base the design of our harmonic comb generating circuit on previous work that sought a size-, weight-, and power-constrained solution to *in-situ* diagnosing of wireless devices [94]. As shown in Fig. 3.3a, the circuit contains a square wave signal generator, a high-pass filter, and a diode, the latter two of which are depicted in Fig. 3.3b. A square wave contains only odd-integer harmonics of its fundamental frequency, which decrease in amplitude inversely proportional to harmonic number. The high-pass filter acts as a differentiator and attenuates the lower-frequency harmonics

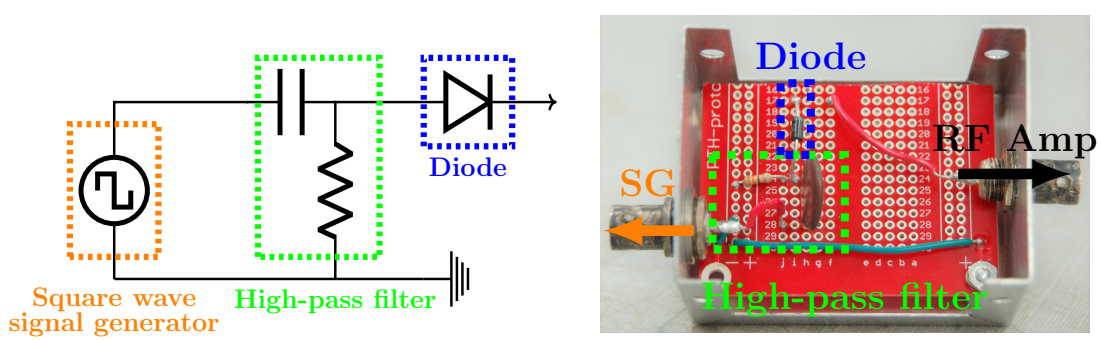

(a) Schematic (b) Hardware

Figure 3.3. The high-pass filter and diode are passive but the oscillator is a signal generator capable of outputing square waveforms. Based on the design in Ref. [94].

of the square wave to decrease the disparity between amplitudes (i.e. it accentuates the sharp edges of the square wave). The directional nature of the diode breaks the positive-negative symmetry of the signal to generate the missing even-numbered harmonics. We amplify this harmonically-rich signal with an E&I 1140LA broadband power amplifier before sending it to the diagnostic's antenna.

The expected frequency range of the plasma wavemode studied determines the high-pass filter's cutoff frequency f_{cut} and the fundamental frequency for the square wave. Since the experimental investigation described in Chapter 4 involves waves with frequencies in the tens to hundreds of kilohertz, we build the four different high-pass filters detailed in Table 3.1. We test the circuit's ability to send harmonically-rich signals to the diagnostic's antenna by inputing square wave frequencies in the 4-20 kHz range. We measure the antenna voltage $V_{ant}(t_n)$ and antenna current $\mathcal{I}_{ant}(t_n)$ to estimate these signals' autopower spectra through the same procedure as that of the probe signals in the previous section. We also calculate their linear spectra, which is the square root of the autopower spectra and correspond to measurements of voltage and current amplitudes at each frequency. Fig. 3.4 shows these four spectra for HPF 1 and an input 4 kHz square wave; Fig. 3.5 does the same but for HPF 4 and an input 10 kHz square wave. The comb structure of all the signals is clear, with hundreds of harmonics present at similar power levels. This signal structure provides a means to excite waves at multiple frequencies simultaneously and at similar power levels, thereby creating the harmonic wave packet that will propagate through a plasma so we can measure the dispersion relation in one shot.

Table 3.1. Component Values for High-Pass Filters

	HPF 1	HPF 2	HPF 3	HPF 4
Capacitance (C)	24.6 nF	9.8 nF	16.5 nF	7.8 nF
Resistance (R)	327 Ω	328 Ω	99.2 Ω	99.1 Ω
Cutoff Frequency (f_{cut})	20 kHz	50 kHz	100 kHz	200 kHz

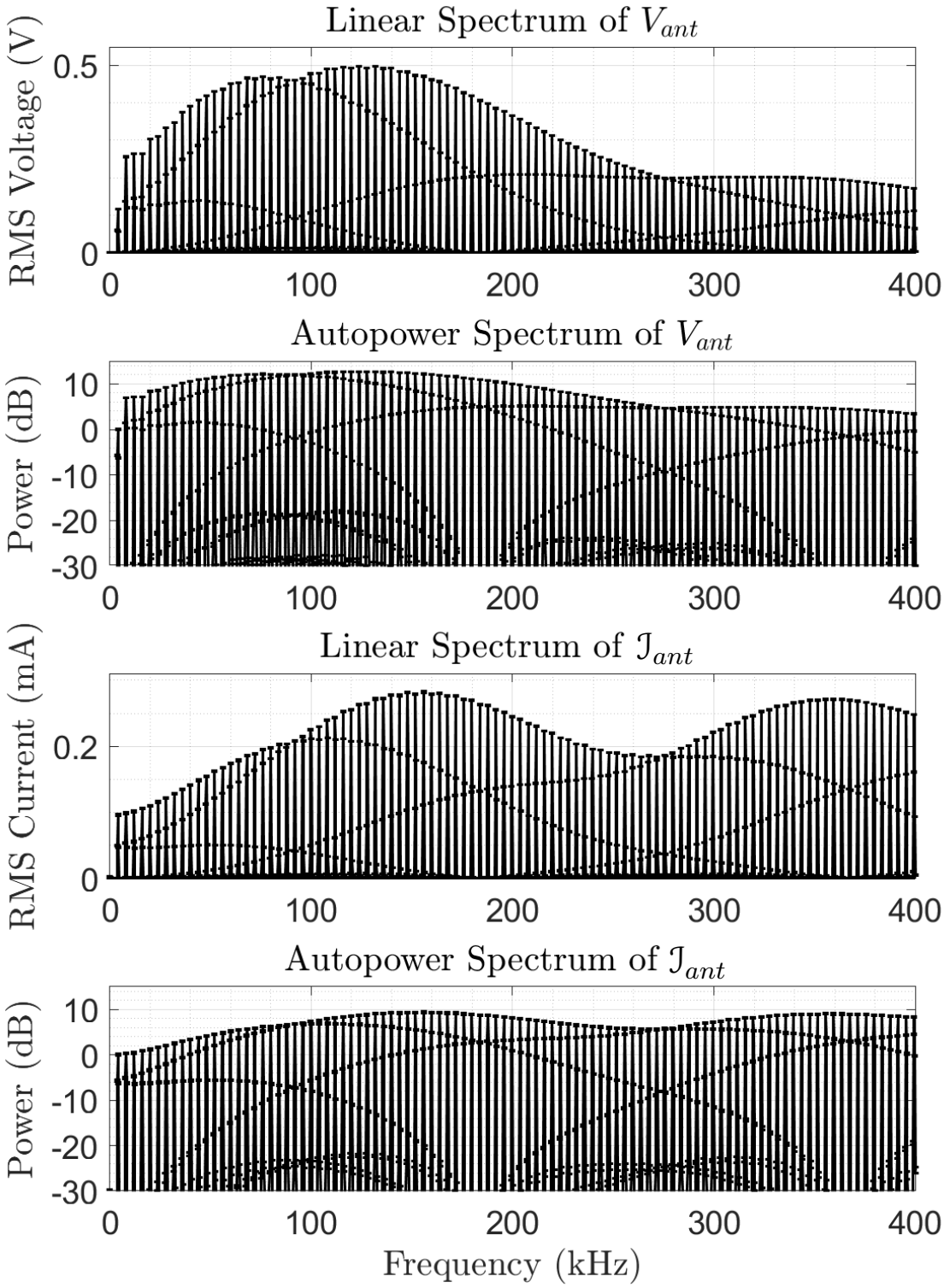

Figure 3.4. These spectra correspond to a circuit with HPF 1 from Table 3.1 and a 4 kHz square wave input. The signal at the fundamental frequency is used as the reference for the decibel normalization.

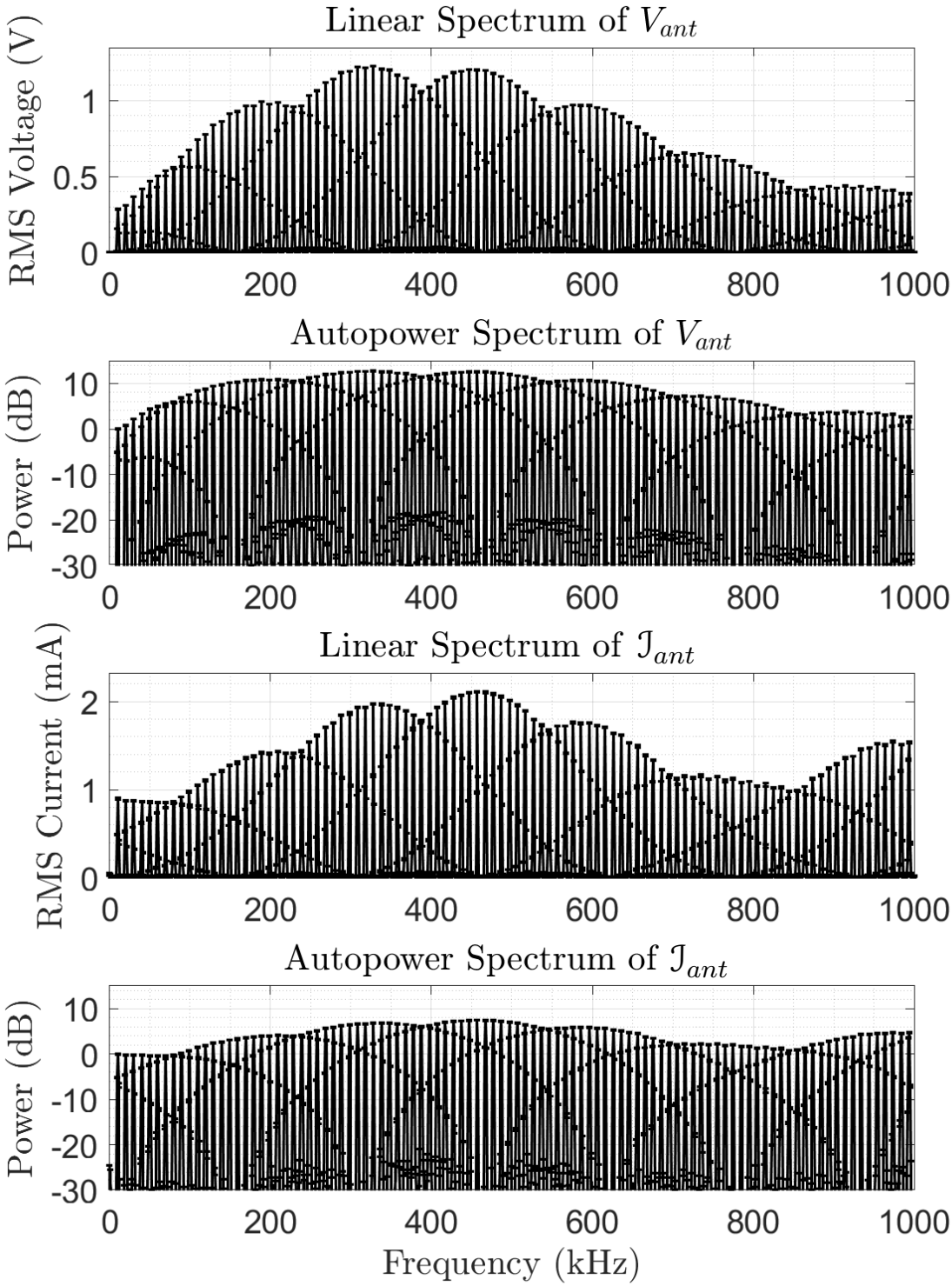

Figure 3.5. These spectra correspond to a circuit with HPF 4 from Table 3.1 and a 10 kHz square wave input. The signal at the fundamental frequency is used as the reference for the decibel normalization.

3.3 Antenna and Probes Design and Manufacture

We build the antenna and probe system photographed in Fig. 3.6 and schematically depicted in Fig. 3.7. Two 1.5 cm by 5 cm, 0.51 mm thick molybdenum plates resting on alumina stand-offs which attach to a 1.27 cm diameter G-10 tube consitute the antenna. We choose this antenna geometry as previous investigations used it to excite electrostatic modes in magnetized plasmas [36, 40]. Tungsten wires attach each plate to coaxial cables which connect the antenna back to the harmonic comb generating circuit described above. The circuit does not have a tuner for matching impedance between the antenna and the plasma load; tuners usually only achieve matching at one or two frequencies [6, 45] and we wish to couple to the plasma at multiple frequencies simultaneously. For our proof-of-concept investigation in the following chapters, we instead decide to operate our plasma source (see Chapter 4) at conditions for which we excite wave packets to validate the AWPI methodology. This tactic of matching the plasma to the antenna has been successful in past experiments which also did not have tuners in their antenna circuit [38, 36, 40].

The diagnostic has three receiver probes to measure wavenumbers in the directions parallel and perpendicular to the plane of the antenna blades which, in the experimental implementation discussed in Chapter 4, also correspond to $k_{\parallel}$ and $k_{\perp}$. The perpendicular tips are 0.1 cm apart and the parallel tip is 0.5 cm away from these; all sit $\sim$1 cm away from the antenna blades. As mentioned in Section 2.1.1, sheath overlap concerns limit the physical size and separation of plasma immersed-probes. However, even the distance between the perpendicular tips (0.1 cm) is much larger than the electron Debye length ($\sim$30 μm) in our plasma source, so we do not expect sheath overlap. These probe tips are 2 mm long, 0.254 mm thick tungsten wires housed inside alumina tubes cased in copper tubes for capacitive shielding and glass tubes for protection from the plasma environment. We bias the tips to -27 V with batteries to operate them as uncompensated ion-saturation-current probes. We use

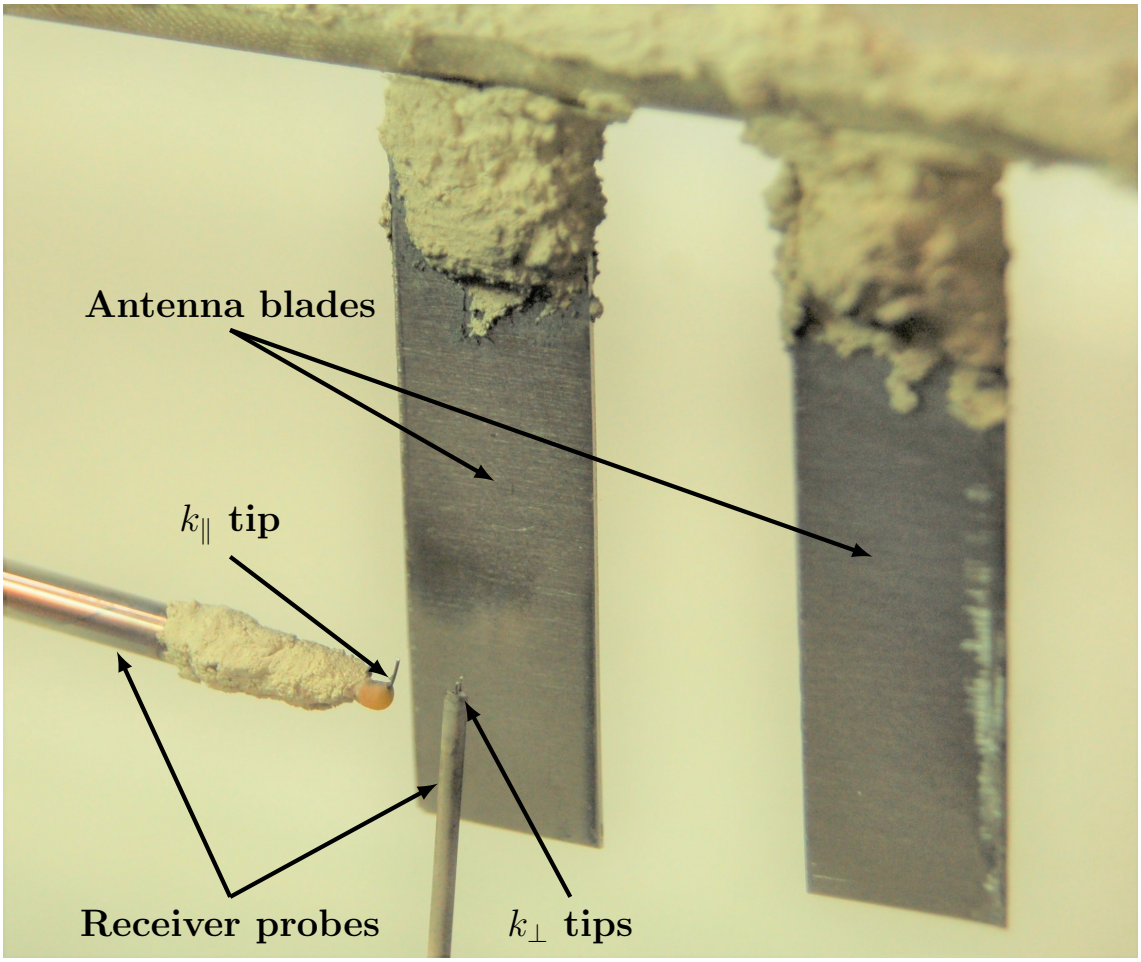

Figure 3.6. All wiring going to the antenna and probe tips runs through G-10 tubes to protect it against the plasma environment. Zirconia paste coats interfaces between wires and housing to prevent damage.

the ion saturation-current $\mathcal{I}_{sat}$ as a proxy for the ion density n_{i} which, for electrostatic modes, is related to the wave potential Φ by [20]

$$\Phi \approx \frac{T_{\mathrm{e}}}{e}\frac{n_{\mathrm{i}1}}{n_{\mathrm{i}0}} \approx \frac{T_{\mathrm{e}}}{e}\frac{\mathcal{I}_{sat1}}{\mathcal{I}_{sat0}}, \tag{3.9}$$

where T_{e} is the electron temperature and the 0 and 1 subscripts refer to the background and linear-perturbation values of the quantity, respectively (see Eq. 1.3). Assuming isothermal plasma compressions, measuring the fluctuations of $\mathcal{I}_{sat}$ at the two probes then gives us insight into spatiotemporal characteristics of electrostatic

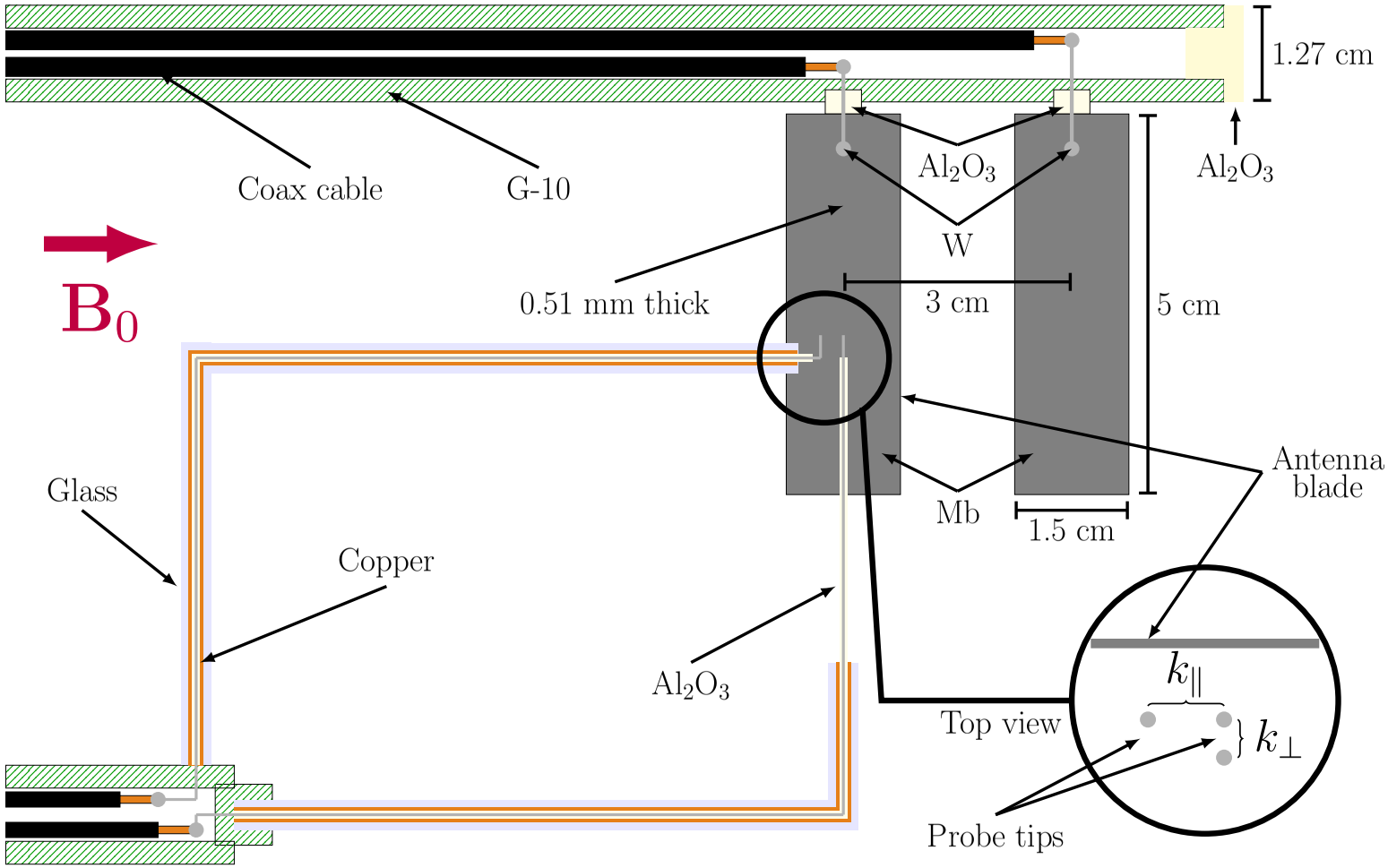

Figure 3.7. The bottom probe arm has two probe tips that measure the wavenumber in the direction perpendicular to the plane of the antenna blades, which in our experiment corresponds to $k_{\perp}$. The upper probe arm has only one probe tip, which in combination with one of the other two probes (see inset top view) measures the wavenumber in the direction parallel to the axis of the G-10 tubes, which in our experiment corresponds to $k_{\parallel}$

.

wavemodes. The wavemodes we investigate in our plasma source are under 1 MHz in frequency, which is well below the ion plasma frequency of 17 MHz for argon and 33 MHz for helium (see Tables 4.2 and 4.3). This ensures that the sheath can adjust fast enough to the varying bulk plasma density and plasma potential [6] so that our use of the ion saturation-current as a proxy for n_{i} remains valid.

3.4 Chapter Summary

In this chapter we overviewed the signal analysis procedure to measure the dispersion relation of a plasma using the active injection of wave packets. We described our design for the harmonic comb generating circuit, antenna, and probes which together constitute our AWPI diagnostic. We demonstrated the reliable generation of harmonically-rich signals in the 1-1000 kHz range which we will use to measure the dispersion relation of low-frequency ion waves in the experimental appartus described in the following chapter.

Chapter 4

Plasma Source for Low-Frequency Ion Wave Studies

In this chapter we provide a brief technical overview of the magnetized RF plasma source in which we use the AWPI diagnostic to measure low-frequency electrostatic wave modes. We provide several representative plasma parameters for the source. Based on these, we present the theory behind the electrostatic ion waves accessible for excitation when operating with argon or helium along with illustrative numerical characterizations obtained using the PRINCE software.

4.1 RF Plasma Source

We use the plasma source pictured in Fig. 4.2 in which previous studies explored ion heating through beating electrostatic waves [95, 55]. Fig. 4.1 depicts a cutaway schematic of the experiment created using the detailed design schematic found in Ref. [55]. The vacuum vessel is a 132 cm long, 15.5 cm inner diameter quartz tube (an upgrade from the previous pyrex tube) which is housed inside a 122 cm long, 10 ring solenoid. A water cooled 19.1 cm outer diameter, 22 cm long saddle antenna surrounds the quartz tube at one end of the vessel. A 1.25 kW RF source which operates at

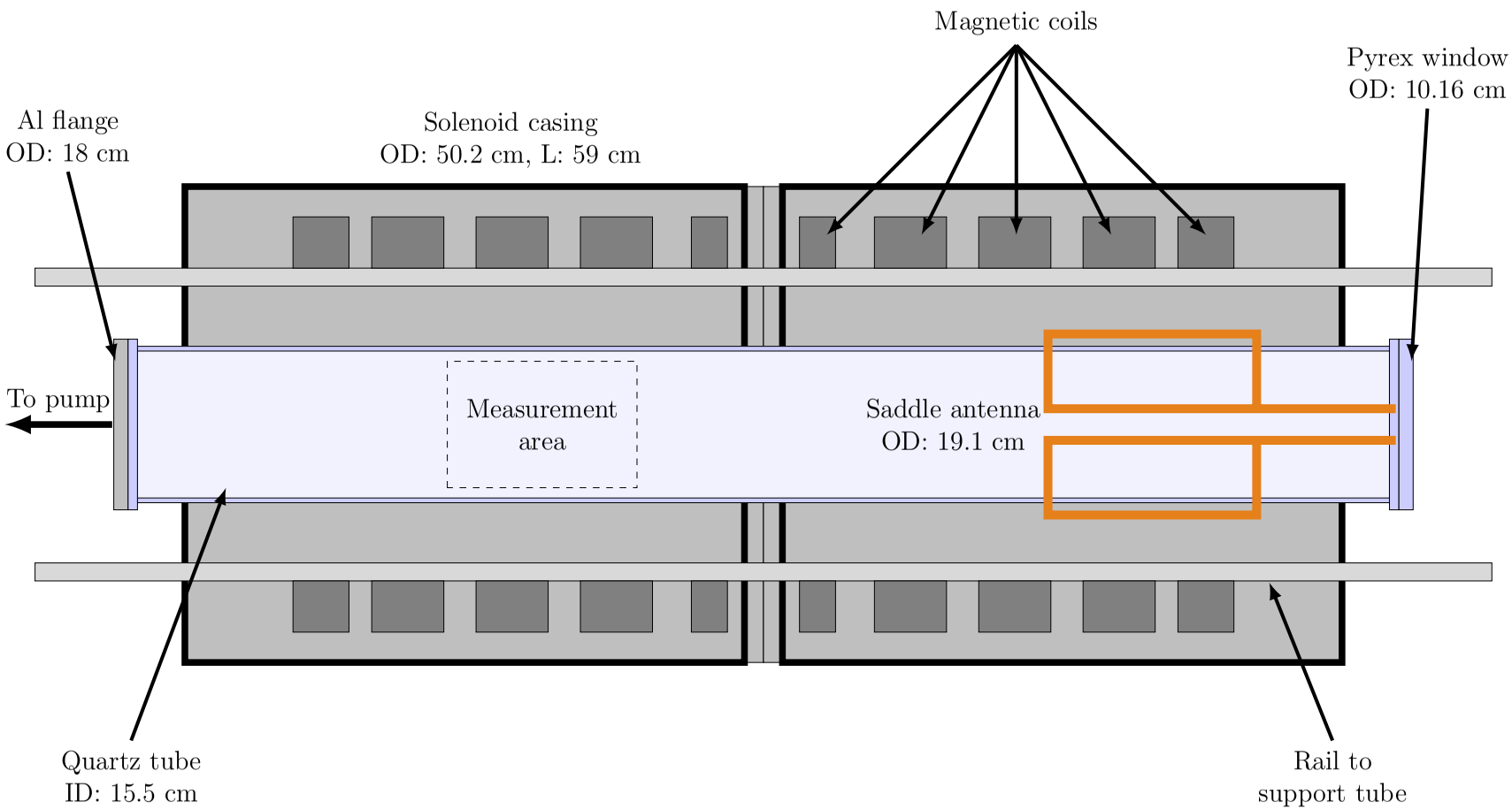

Figure 4.1. The area where we measure the dispersion relation is at the other end of the quartz tube than the RF saddle antenna to reduce the background noise. Two padded G-10 half rings (not depicted) which roll along the rails support the quartz tube.

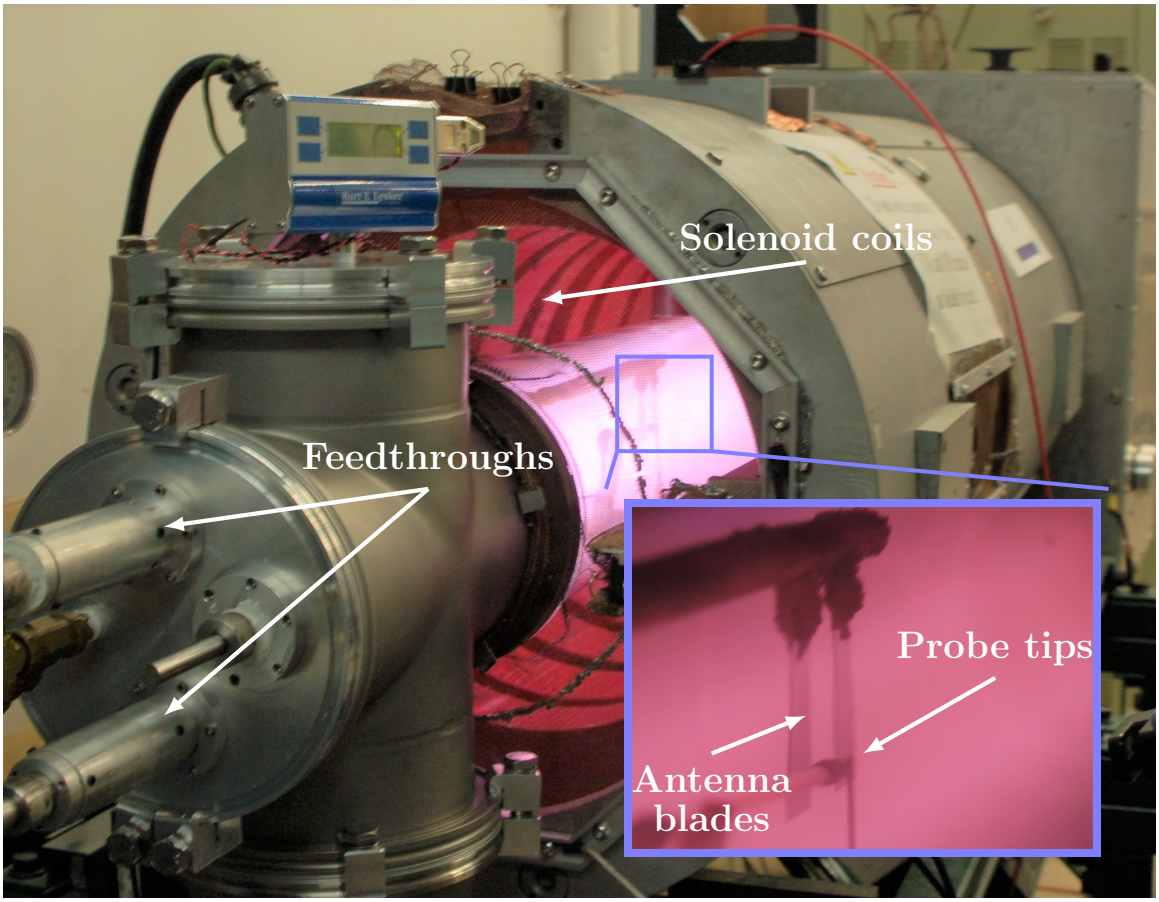

Figure 4.2. The saddle antenna sustains the 13.56 MHz argon discharge inside the quartz vessel. Feedthroughs in the aluminum cross provide physical access to the plasma. The AWPI diagnostic sits near the center of the discharge.

13.56 MHz powers the saddle antenna while an L network with two Jenning 1000 pF 3 kV variable vacuum capacitors matches the RF signal to the plasma discharge with a voltage standing wave ratio (VSWR) in the range $1 - 1.4$. At the other end of the vessel, an aluminum cross connects the quartz tube to a 140 l/s turbomolecular pump which is backed with a Varian TriScroll 300 pump. A KJLC 300 series gauge monitors the neutral pressure in the chamber; the ultimate pressure achievable is less than 0.1 mTorr. The solenoid comprises two klystron Varian 1955A magnets placed end to end, which generate an axial background magnetic field. Table 4.1 presents the source's typical operational parameters.

Table 4.1. Plasma Source Operational Parameters

Parameter	Value	Parameter	Value
RF Power (P_{RF})	250 W	RF Frequency (f_{RF})	13.56 MHz
Background Magnetic Field (B_0)	526 G	Neutral Pressure ($\mathcal{P}_\mathrm{o}$)	0.1-5 mTorr

We operate the source with either argon or helium. Radial profiles for the electron temperature and electron density when operating with argon reported in Ref. [55] are reproduced in Fig. 4.3. Along with these, we also use ion temperature and background magnetic field values reported in the same reference to construct Table 4.2 to present representative values of various plasma parameters. These reflect the plasma state in the near-centerline region $r \approx 0 - 1.5$ cm where we measure dispersion relations with the AWPI diagnostic. We do not have corresponding measurements for these plasma parameters when operating with helium, so we instead use a similarly-sized sized RF plasma source operated at comparable power levels, background pressures, and RF frequencies [96] as a reference to construct Table 4.3 with order of magnitude estimates for the helium plasma parameters. Fig. 4.4 schematically depicts the electrical diagram for the AWPI diagnostic implemented into the source as well as the data acquisition for simultaneously measuring antenna voltage, antenna current, and the current signals for two of the three AWPI receiver probes (so $k_\perp$ and $k_\parallel$ measurements are not simultaneous).

Table 4.2. Representative Argon Plasma Parameters near the Centerline

Parameter	Value	Parameter	Value
Electron Density (n_e)	2.5×10^{17} m^{-3}	Ion Plasma Frequency ($f_{p,\mathrm{i}}$)	17 MHz
Electron Temperature (T_e)	3.5 eV	Ion Sound Speed (c_S)	3.2 km/s
Ion Temperature (T_i)	0.25 eV	Ion Thermal Velocity ($v_{th,\mathrm{i}}$)	780 m/s
Ion Larmor radius (ρ_i)	6 mm	Ion Cyclotron Frequency ($f_{c,\mathrm{i}}$)	20 kHz

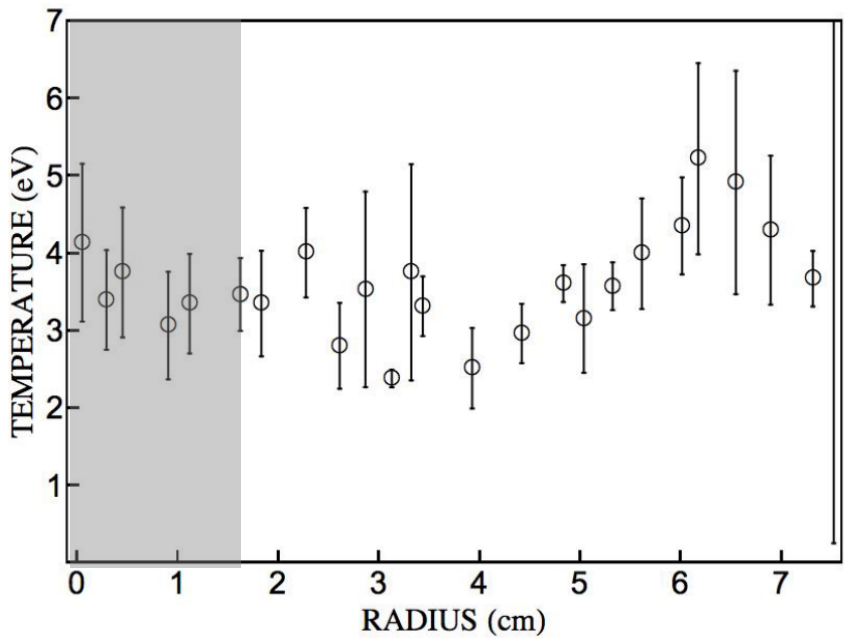

(a) Electron temperature radial profile

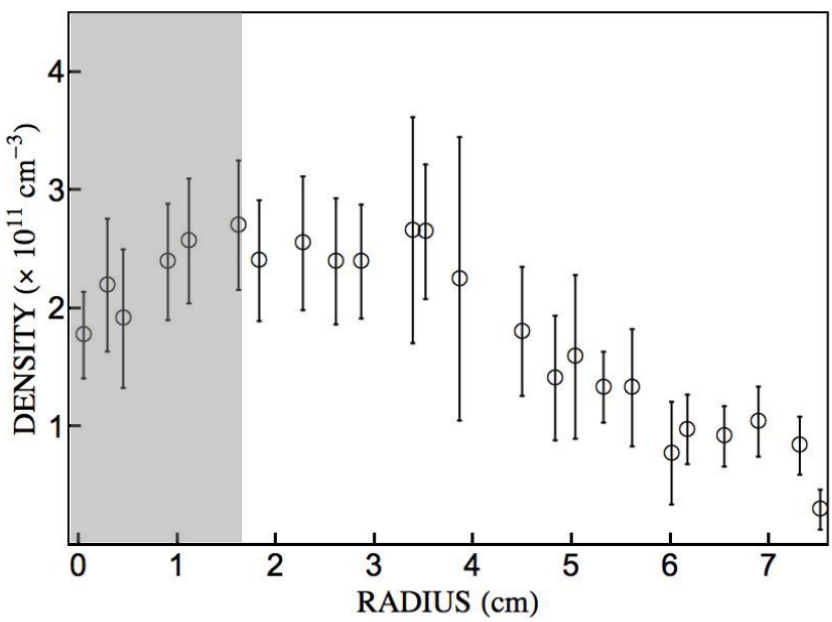

(b) Electron density radial profile

Figure 4.3. Profiles for T_e and n_e in our plasma source when running with argon. The shaded region demarks the measurement region in our work. Reproduced from Ref. [55].

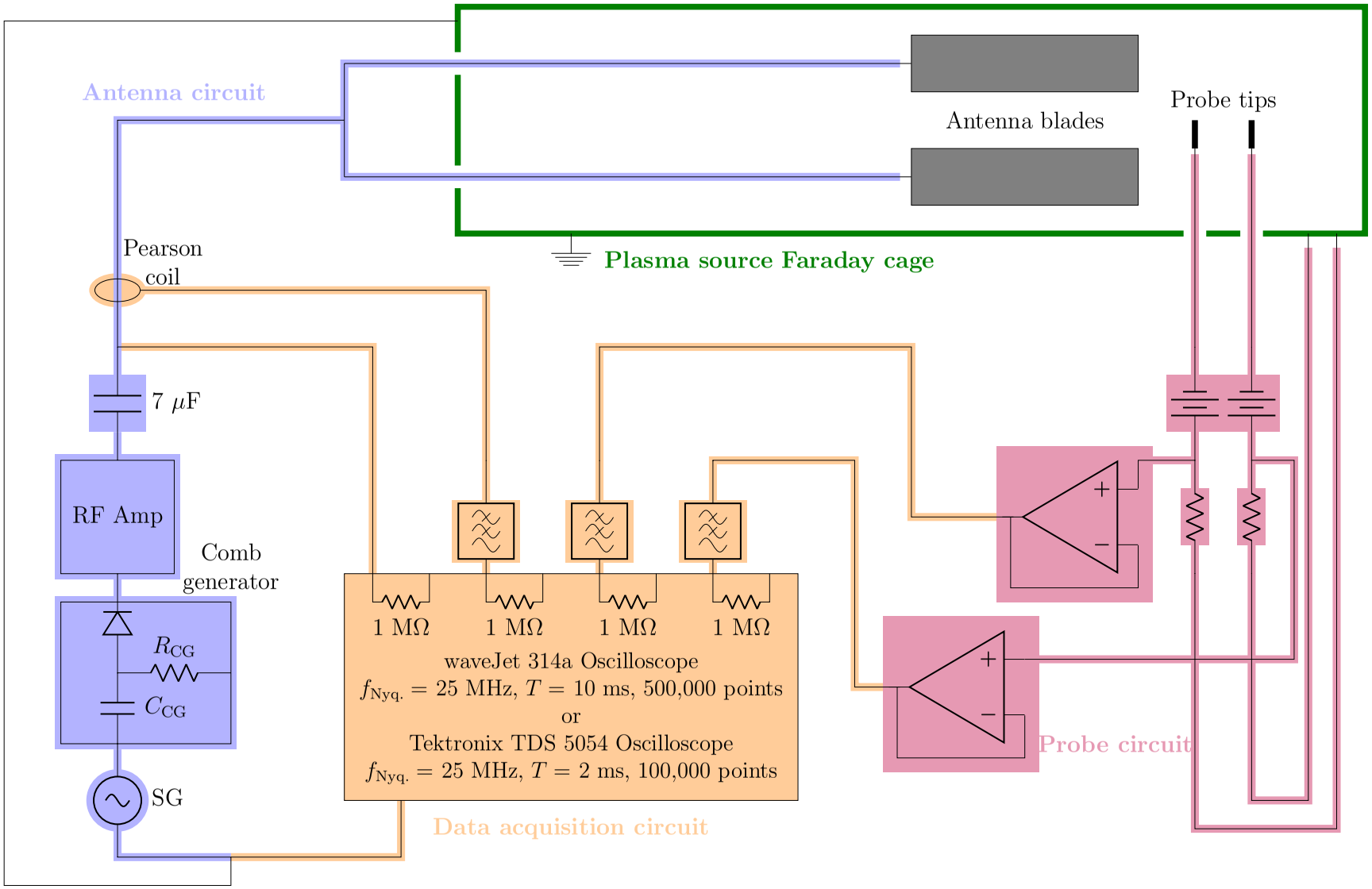

Figure 4.4. The shaded regions represent the shielding of the various circuits and their connections. The probe tips connected are either both $k_\perp$ tips or one $k_\perp$ tip with the $k_\parallel$ tip.

Table 4.3. Estimated Helium Plasma Parameters near the Centerline

Parameter	Value	Parameter	Value
Electron Density (n_e)	10^{17} m^{-3}	Ion Plasma Frequency ($f_{p,\mathrm{i}}$)	33 MHz
Electron Temperature (T_e)	4 eV	Ion Sound Speed (c_S)	10 km/s
Ion Temperature (T_i)	0.1 eV	Ion Thermal Velocity ($v_{th,\mathrm{i}}$)	1.6 km/s
Ion Larmor radius (ρ_i)	1.2 mm	Ion Cyclotron Frequency ($f_{c,\mathrm{i}}$)	200 kHz

4.2 Electrostatic Ion-Cyclotron Waves

For electrostatic waves in an isothermal ($T_\perp = T_\parallel$ for both ions and electrons) magnetized plasma Eq. 1.9 takes the form [31]

$$\mathcal{D}(\omega, \mathbf{k}) = k_\parallel^2 + k_\perp^2 + \sum_\mathrm{s} \lambda_{D,\mathrm{s}}^{-2} \left[1 + \sum_n e^{-b_\mathrm{s}} I_n(b_\mathrm{s}) Z\left(\zeta_{n,\mathrm{s}}\right) \zeta_0 \right] = 0, \tag{4.1}$$

where I_n is the nth order modified Bessel function of the first kind, Z the plasma dispersion function of Fried and Conte,

$$\zeta_{n,\mathrm{s}} = \frac{\omega - n\,\omega_{c,\mathrm{s}} - k_\parallel v_{d,\mathrm{s}}}{\sqrt{2}\,k_\parallel v_{th,\mathrm{s}}}, \quad b_\mathrm{s} = \frac{k_\perp^2 v_{th,\mathrm{s}}^2}{\omega_{c,\mathrm{s}}^2}, \tag{4.2}$$

$\lambda_{D,\mathrm{s}}$ the species Debye length, $v_{th,\mathrm{s}}$ the species thermal velocity, $v_{d,\mathrm{s}}$ the species parallel drift velocity, and $\omega_{c,\mathrm{s}}$ the species cyclotron frequency. If we consider low-frequency oscillations ($\omega \ll \omega_{c,\mathrm{e}}$) and fully magnetized electrons ($b_\mathrm{e} \propto \rho_\mathrm{e}^2/\lambda_\perp^2 \ll 1$), we can re-express the above as [36, 40]

$$\begin{aligned} k_\parallel^2 + \frac{\omega_{p,\mathrm{e}}^2}{v_{th,\mathrm{e}}^2} \left[1 + \frac{\omega}{\sqrt{2} k_\parallel v_{th,\mathrm{e}}} Z(\zeta_{0,\mathrm{e}}) \right] + \\ k_\perp^2 \left[1 + \frac{\omega_{p,\mathrm{e}}^2}{\omega_{c,\mathrm{e}}^2} + \frac{\omega_{p,\mathrm{i}}^2\, e^{-b_\mathrm{i}}}{k_\parallel\, v_{th,\mathrm{i}}\, \omega\, b_\mathrm{i}} \sum_n n^2 I_n(b_\mathrm{i}) Z(\zeta_{n,\mathrm{i}}) \right] = 0. \end{aligned} \tag{4.3}$$

Note that this dispersion relation has the symmetry $\mathcal{D}(\omega, k_\perp, k_\parallel) = \mathcal{D}(\omega, -k_\perp, k_\parallel)$.

Two wavemodes have been identified as solutions to Eq. 4.3 in the low-frequency range ($\omega \gtrsim \omega_{c,\mathrm{i}}$) we explore in our plasma source: the electrostatic ion-cyclotron (EIC) wave [89, 97, 38] and the neutralized ion Bernstein (NIB) wave [98, 36]. The EIC solution exhibits the acoustic-like relation

$$\omega^2 = \omega_{c,\mathrm{i}}^2 + k_\perp^2 c_S^2, \tag{4.4}$$

where $c_S = \sqrt{(T_\mathrm{e} + 3T_\mathrm{i})/m_\mathrm{i}}$ is the ion sound speed. This expression can be obtained by either simplifying Eq. 4.3 by assuming $b_i \ll 1$ or from a simpler warm plasma fluid model considering nearly-perpendicular propagation of ion waves [31, 32]. The NIB solution has one branch for each interval $n\,\omega_{c,\mathrm{i}} \leq \omega \leq (n+1)\,\omega_{c,\mathrm{i}}$, $n \geq 1$, which asymptotes to $n\,\omega_{c,\mathrm{i}}$ as $k \to \infty$. In the following section we provide an illustrative numerical characterization of both wavemodes using the PRINCE software.

At our low-temperature plasma's operating background neutral pressure range of $0.1 - 5$ mTorr, ion-neutral charge-exchange collisions can cause the NIB wavemodes to be highly damped [99, 55]. Targeting these wavemodes for excitation has been more difficult in past laboratory experiments [36], so we expect to primarily excite the EIC branch, which also requires that [36]

$$\omega_{c,\mathrm{i}} < \omega_{p,\mathrm{i}}, \quad T_\mathrm{i} \lesssim T_\mathrm{e}, \quad \text{and} \quad \sqrt{2} v_{th,\mathrm{i}} \ll {}^{\omega}/_{k_\parallel} \ll \sqrt{2} v_{th,\mathrm{e}}. \tag{4.5}$$

The first two conditions are always satisfied in our experiment; the third is satisfied when $k_\parallel$ is around $0.2 - 1$ cm^{-1} for wave frequencies in the $20 - 200$ kHz range for argon and in the $200 - 1000$ kHz range for helium. Adhering to this third condition informed our design of the high-pass filters and choice for the fundamental frequency of the square wave in the harmonic comb generating circuit presented in Section 3.2.

4.3 Numerical Characterization with PRINCE

We input the representative argon plasma parameters from Table 4.2 for our numerical characterization, however qualitatively similar results arise when using the helium plasma parameters. Since the NIB branches of the ion-cyclotron waves have a non-monotonic and discontinuous behavior with respect to ω [35, 40], we choose to characterize the roots $\omega(\mathbf{k})$ of Eq. 4.3 for computational tractability. We also truncate the biinfinite sum by setting $-35 \leq n \leq 35$ since the value of this $\mathcal{D}$ converges up to numerical precision at about $n \approx 25 - 30$ for the range of ω, $\mathbf{k}$, and p_i we consider. We input the argon plasma parameters from Table 4.2 into PRINCE and specify an iteration over $k_\perp = k_x$ decreasing from 1000 /m to 5 /m in steps of 5 /m with $k_y = 0$ /m and $k_\parallel = k_z = 25$ /m. We search for damping and propagating modes in the 15-205 kHz (0.75-10.25 $\omega_{c,\mathrm{i}}$) range with damping rates no larger than 20.5 kHz (1.025 $\omega_{c,\mathrm{i}}$). Searching for the initial locations of the roots at large $k_\perp$ allowed us to successfully resolve multiple branches of the NIB solution.

On the other hand, searching for roots at small $k_\perp$ yielded discontinuous solutions which seemed to hop between different NIB branches, the EIC branch, or a linear solution with the acoustic relation $\omega_r \approx k_{r\perp} v_{th,\mathrm{i}}$. This indicates that this search region has a more intricate structure for the basins of attraction of the root-finding procedure. This was also reflected by PRINCE's much larger computation time (about 20 hours compared to 2 hours). We were thus unable to resolve the EIC branch using PRINCE as all attempts resulted in discontinuous solutions. Searching for the initial roots at large values of $k_{r\perp}$ did not work either as PRINCE kept converging to NIB branches. Instead, we had to solve for ω at each value of $k_{r\perp}$ by providing a Newton-Raphson solver an initial guess calculated using the fluid theory from Eq. 4.4 and multiplied by a factor of $1 - 0.3i$ to obtain sufficiently well-behaved behavior for both ω_r and ω_i. Even this process did not yield as smooth a result as the ones for the NIB branches.

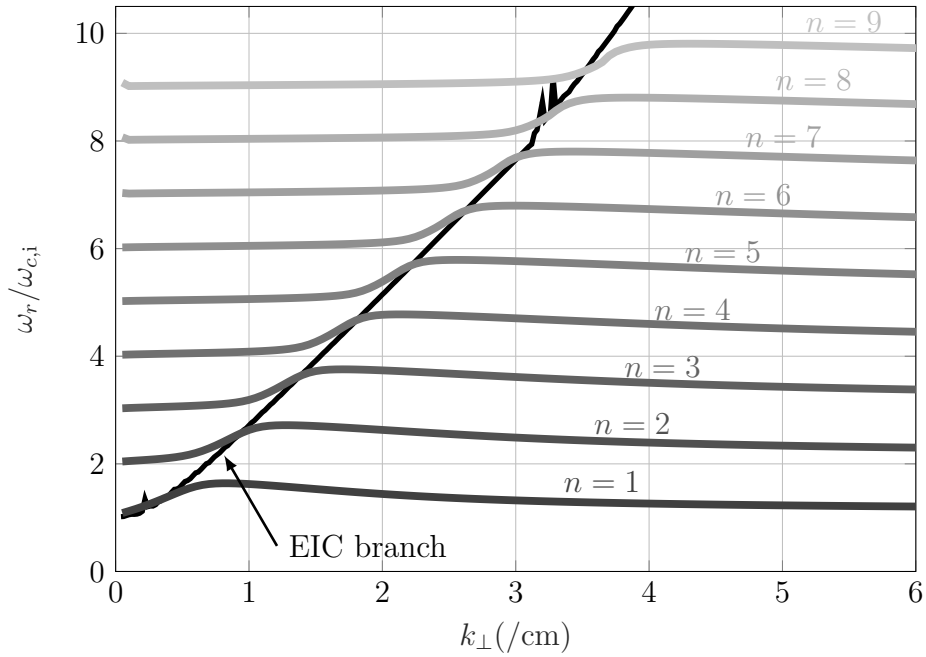

(a) Propagation of the EIC branch along with nine NIB branches.

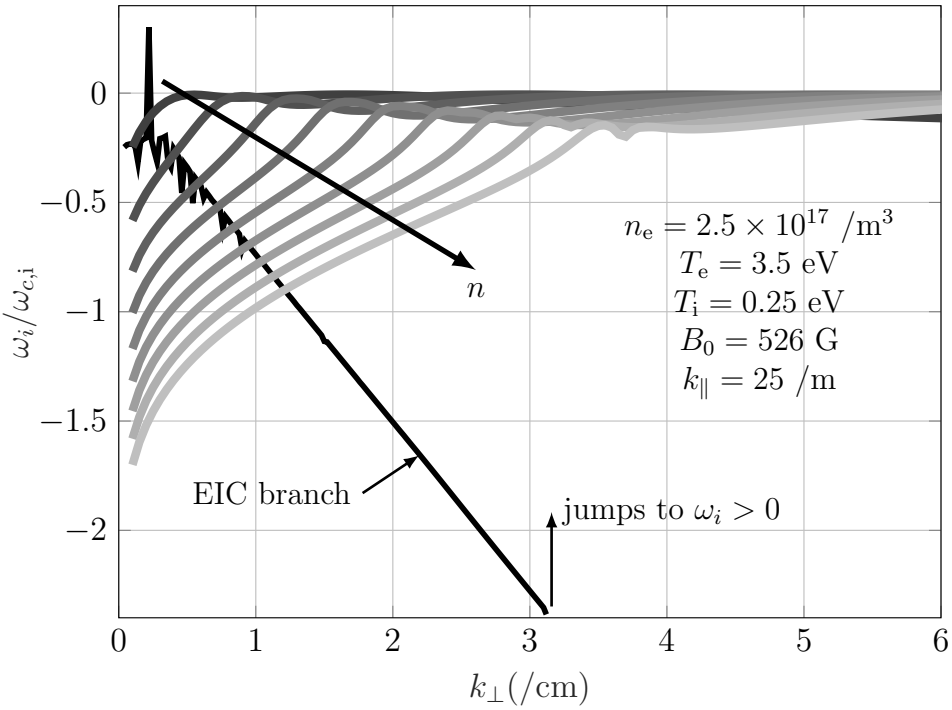

(b) Decay of the EIC branch along with nine NIB branches. The discrepancy reflects the sensitivity of the root-finding procedures in the complex plane.

Figure 4.5. Numerical solutions for Eq. 4.3 in our argon plasma source. The NIB branches (shades of gray) are better numerically behaved than the EIC branch (black).

Fig. 4.5 shows PRINCE's results for nine NIB branches along with our 'hard-coded' result for the EIC branch. Similarly to past work, for each NIB branch ω_r asymptotes to its corresponding value of $n\omega_{c,\mathrm{i}}$ as $k_{r\perp} \to \infty$. As expected from the fluid theory, the EIC branch exhibits the acoustic relation $\omega_r/k_{r\perp} \approx c_S$ for large $k_{r\perp}$ which approaches a cutoff at $\omega_{c,\mathrm{i}}$ for small $k_{r\perp}$. The propagation of the EIC branch matches that of the positive-slope portions of the NIB branches, which reflects that the fluid EIC wave theory 'smears' the ion kinetic effects (i.e. finite ion Larmor radius effects) necessary to predict the negative-slope portion of the NIB branches [35]. The ω_i are comparable for small values of $k_{r\perp}$. The difference at larger values reflects the NIB branches' shift towards a non-propagating resonance ($v_g \to 0$ for $k_{r\perp} \not\to 0$) with $\omega_r \to n\omega_{c,\mathrm{i}}$ while the propagating EIC branch experiences larger damping rates for smaller wavelengths, possibly due to Landau damping by the electrons becoming more significant [100, 97]. Just past $k_{r\perp} = 3$ /cm the solution for the EIC branch jumped from negative to positive ω_i (perhaps indicating a switch between complex-conjugate roots), again showcasing the sensitivity of the root-tracking process.

Though the case presented above is for one value of $k_\parallel$, similar results for ω_r arise when we vary $k_\parallel$ within the range stipulated by the third condition in Eq. 4.5 for wave excitation. ω_i generally remains negative and decreasing in value as shown in Fig. 4.5b, indicating decaying propagating wavemodes which damp more strongly at higher frequencies and shorter wavelengths. This suggests that higher-frequency wavemodes may not be detectable with our diagnostic or give results not in line with theory due to diminished signal strength. Abrupt jumps between positive and negative still occur. This behavior was nevertheless better than that observed with the 'hard-coded' approach, in which varying $k_\parallel$ or the inital guess for the Newton-Raphson solver had significant effects on both ω_r and ω_i. Even trying to resolve the NIB branches by starting at large values of $k_{r\perp}$ and iterating downward (like we did with PRINCE) took several trials and more time, highlighting the importance

of the initial guess fed to a root-tracking procedure and PRINCE's ability to do so autonomously.

4.4 Chapter Summary

In this chapter we described the linear RF plasma source in which we implement the AWPI diagnostic to measure dispersion relations. We overviewed the relevant kinetic wave theory which describes the EIC and NIB wavemodes that may arise in our system given its characteristic plasma parameters. We also present illustrative numerical characterizations of these wavemodes obtained using the PRINCE software described in the appendices.

Chapter 5

Results and Discussion[1]

In this chapter we present our measurements of the dispersion relation of electrostatic ion-cyclotron waves taken with the AWPI diagnostic both in argon and helium plasmas. The $k_{r\perp}$ measured in the argon plasma agree with fluid theory predictions of EIC waves (unfortunately, we did not obtain accompanying $k_{\parallel}$ measurements to compute kinetic theory predictions) while the $k_{i\perp}$ measured indicate a decaying wave mode. The $k_{r\perp}$ measured in the helium plasma coincide with predictions of the kinetic theory that we self-consistently computed by inputing the $k_{\parallel}$ measured into Eq. 4.3. Both in argon and helium the AWPI diagnostic provided simultaneous measurements of the EIC waves' dispersion relation at dozens of frequencies spanning 2-5 harmonics of the ion-cyclotron frequency.

5.1 Dispersion Relation Measurements in Argon

We use the AWPI diagnostic equipped with HPF 1 from Table 3.1 to measure the dispersion relation in our plasma source while running with argon. Fig. 5.1 presents

[1]This chapter is based on work being prepared to be submitted for publication and previously presented in [88]: Rojas Mata, S. and Choueiri, E.Y., "Plasma Dispersion Relation Measurements through Active Injection of Wave Packets," *36th International Electric Propulsion Conference*, Vienna, 2019.

the estimates of the autopower and coherence spectra of the two receiver probes which take measurements in the direction perpendicular to the antenna blades and, hence, the background magnetic field. The harmonic comb structure measured at the antenna (see Fig. 3.4) is also present in these spectra, indicating that harmonically-rich wave packets propagated through the plasma to reach the probes (similar structures arising from AC coupling were barely recordable when the plasma was absent). The measurements at the harmonics of the square wave's fundamental frequency of 4 kHz have a high coherence with low error, satisfying our criteria for coherent wave propagation. This yielded measurements of the wavenumber at nearly three dozen frequencies in one shot, a significant advance over previous procedures of using simple monochromatic sinusoidal excitations to measure wavenumbers one at a time.

To determine which wavemode carried the signal from the antenna to the probes, we look at the measured dispersion relation. Fig. 5.2a presents the measured $k_{r\perp}$ alongside predictions to the fluid dispersion relation of EIC waves from Eq. 4.4 for varying electron temperatures. The data begins to deviate away from the expected dispersion relation at around 6 ion-cyclotron harmonics (120 kHz), at which point the EIC mode does not seem to be excited. Fig. 5.2b displays corresponding measurements of $k_{i\perp}$ which indicate spatially decaying wave potential amplitudes over characteristic lengthscales around $4.5 - 6$ cm. The magnitude of $k_{i\perp}$ is comparable to that of $k_{r\perp}$ as observed before [97], but appears roughly constant instead of roughly proportional to ω. We calculate the error bars for all wavenumbers by propagating through Eqs. 3.6 and 3.7 the variance in the auto- and cross-power spectra estimates provided by Welch's method and in the distance between the probes. We unfortunately do not have the corresponding measurements of $k_{\parallel}$ necessary to self-consistently solve Eq. 4.3 and obtain kinetic theory predictions for $k_{i\perp}$. However, we took measurements of $k_{r\perp}$ and $k_{i\perp}$ one frequency at a time using purely sinusoidal excitations (i.e. monochromatic instead of harmonic excitations) over a similar fre-

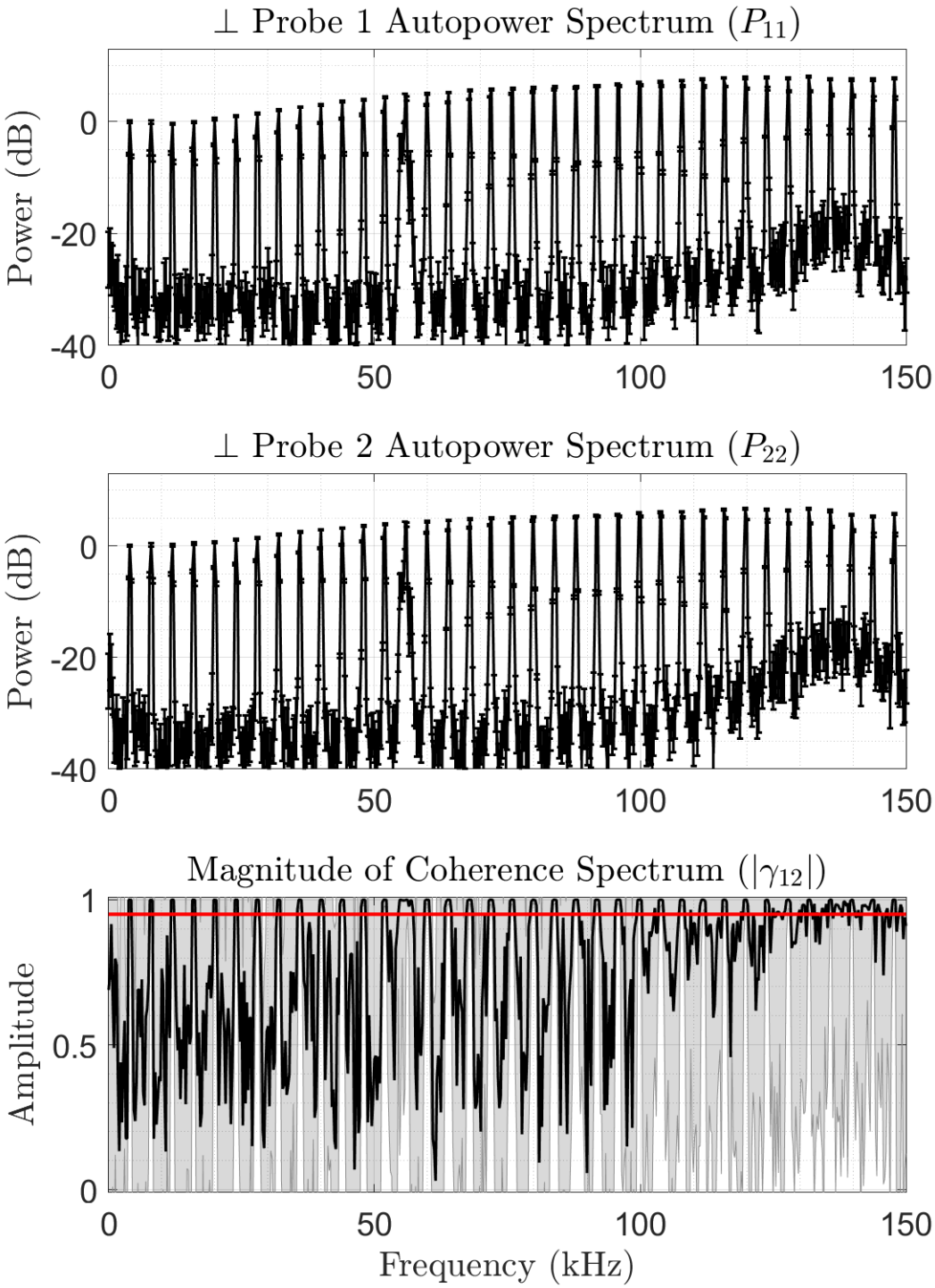

Figure 5.1. We use the power of each signal at the fundamental frequency of 4 kHz as the reference for the normalization. The shaded region in the lower plot indicates the error in $|\gamma_{12}|$. The red line is at a coherence of 0.95.

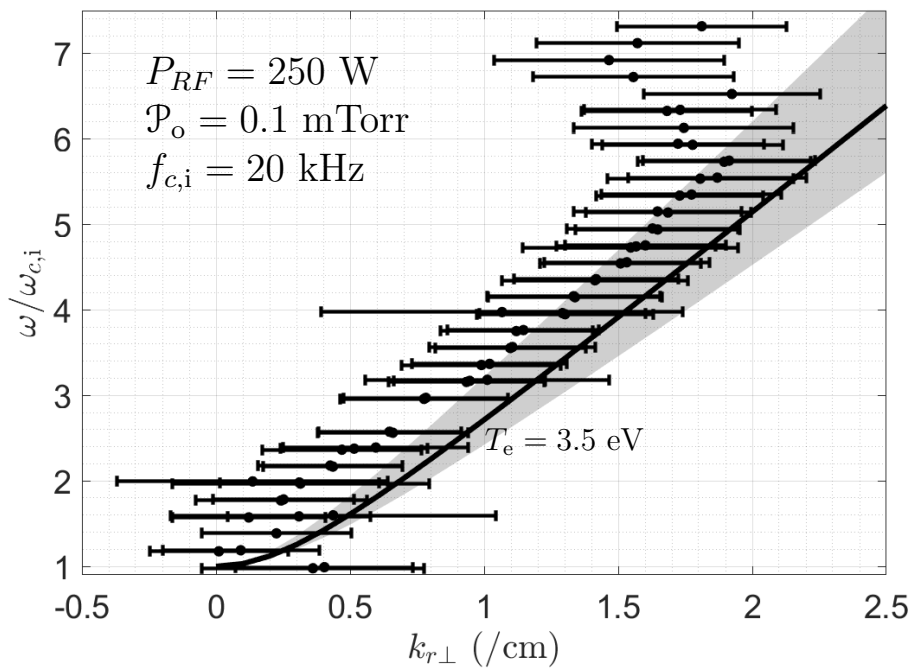

(a) The gray region represents the theoretical predictions of the fluid plasma model from Eq. 4.4 for $T_e = 2.5-5.5$ eV, $T_i = 0.25$ eV, and $B_0 = 526$ G.

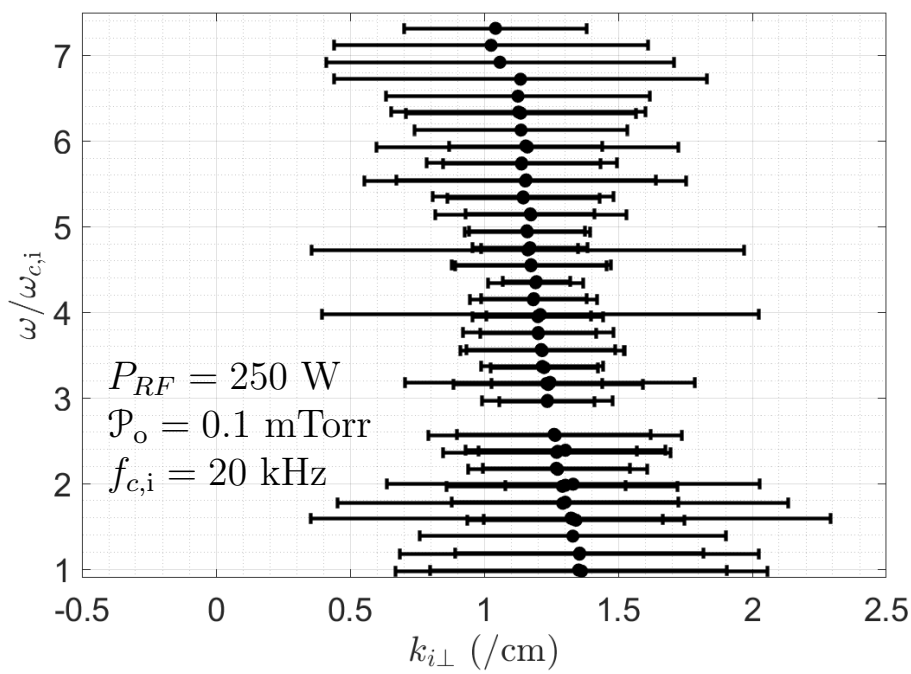

(b) The fluid theory does not predict $k_{i\perp}$ and we do not have accompanying $k_{\parallel}$ measurements to provide self-consistent kinetic theory predictions.

Figure 5.2. All measurements have $|\gamma_{12}| > 0.95$ with an error less than 0.05.

quency range and found them to agree with the measurements presented in Fig. 5.2. This upholds our claim that the AWPI technique is an expedited version of previous monochromatic active wave injection techniques to measure dispersion relations.

5.2 Dispersion Relation Measurements in Helium

Similar to the above, we use the AWPI diagnostic equipped with HPF 4 from Table 3.1 to measure the dispersion relation in our plasma source while running with helium. Fig. 5.3 presents the estimates of the autopower and coherence spectra of the two receiver probes that take measurements in the direction perpendicular to the antenna blades; Fig. 5.4, those in the direction parallel to the antenna blades and the background magnetic field. The harmonic comb structure measured at the antenna (see Fig. 3.5) is again present in these spectra only when the plasma is present, indicating as before that harmonically-rich wave packets propagated through the plasma to reach the probes. The measurements at the harmonics of the square wave's fundamental frequency of 10 kHz have a high coherence with low error, again satisfying our criteria for coherent wave propagation and yielding wavenumber measurements at several frequencies simultaneously.

Fig. 5.5a displays the measured $k_{r\perp}$ alongside solutions to the kinetic dispersion relation from Eq. 4.3 for varying electron temperatures and using the measured $k_{\|}$, the real part of which is shown in Fig. 5.5b. The data agrees with the kinetic predictions over the 2-4 ion-cyclotron harmonic range, in which $k_{\|} \approx -0.8$ /cm. As before, the deviation from theory above that frequency range indicates that the EIC wavemode is no longer excited or too damped to be correctly detected. In the 1-2 ion-cyclotron harmonic range, $k_{r\|}$ varies beyond the values for which the third condition in Eq. 4.5 stipulates EIC waves can be excited, which might explain the deviation of $k_{r\perp}$ from theory in that range. The helium plasma was noisier than the argon plasma, which

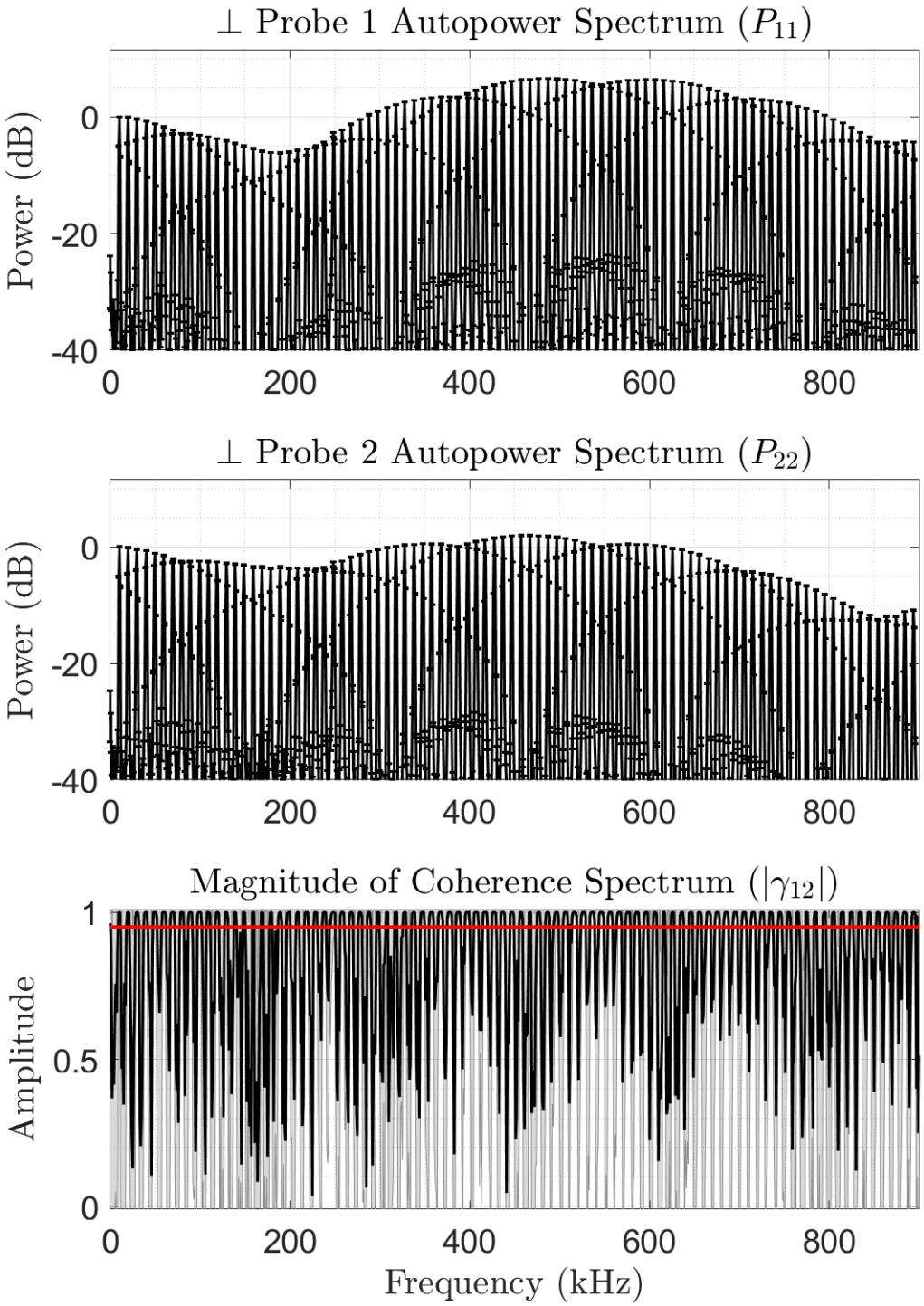

Figure 5.3. We use the power of each signal at the fundamental frequency of 10 kHz as the reference for the normalization. The shaded region in the lower plot indicates the error in $|\gamma_{12}|$. The red line is at a coherence of 0.95.

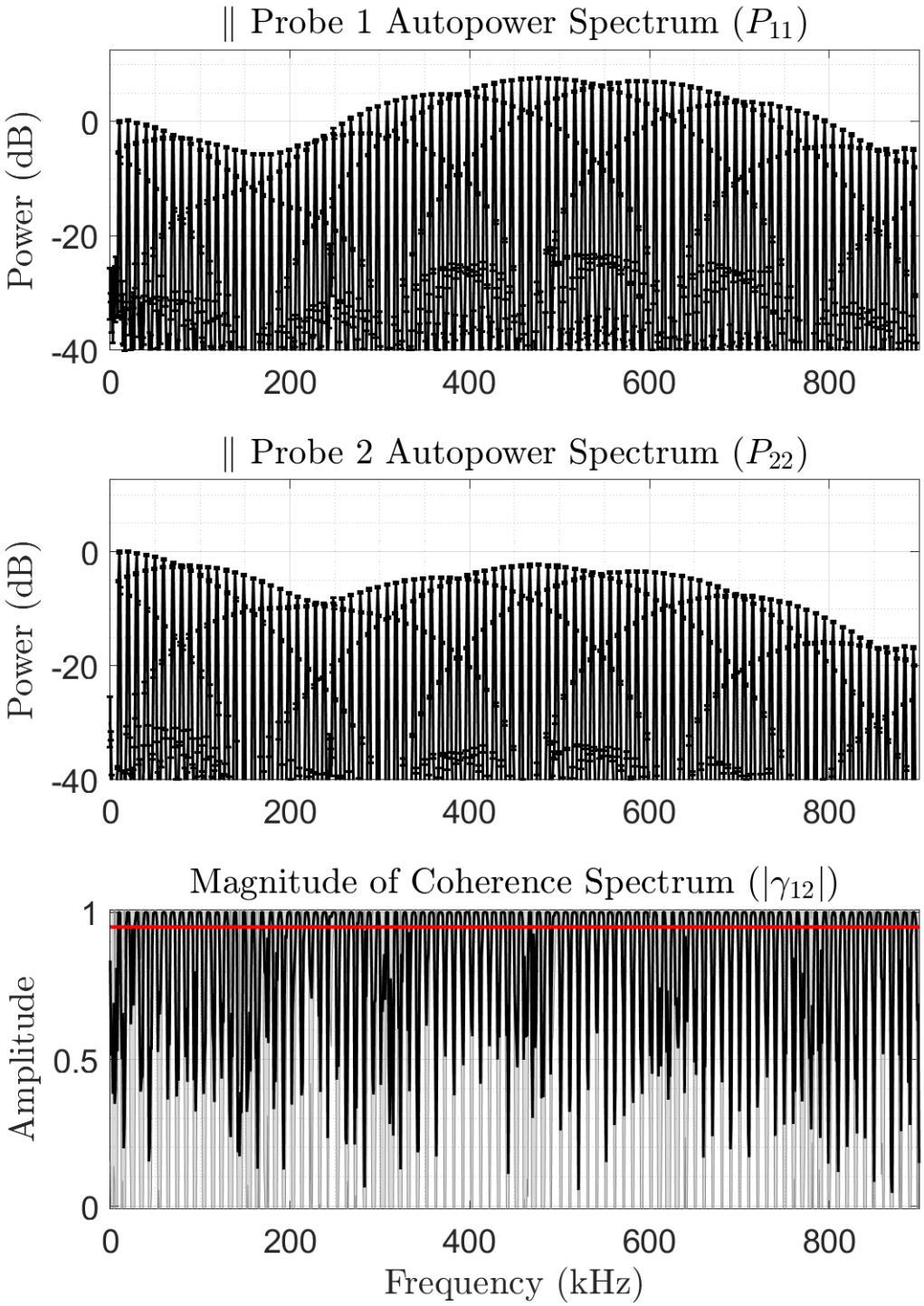

Figure 5.4. We use the power of each signal at the fundamental frequency of 10 kHz as the reference for the normalization. The shaded region in the lower plot indicates the error in $|\gamma_{12}|$. The red line is at a coherence of 0.95.

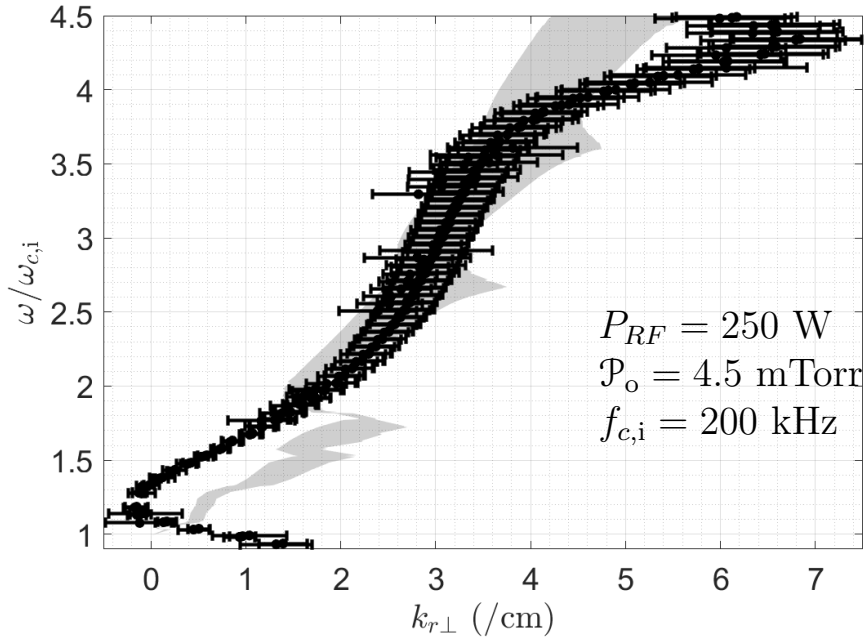

(a) The gray region represents the theoretical predictions of the kinetic plasma model from Eq. 4.3 for $T_e = 3 - 6$ eV, $T_i = 0.25$ eV, $B_0 = 526$ G, and the measured $k_{\|}$.

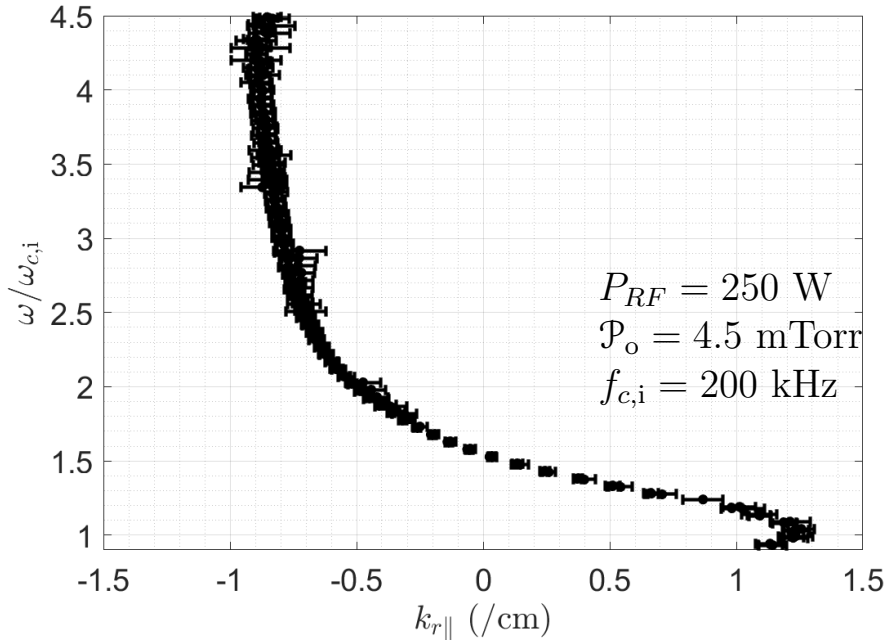

(b) The negative value of the $k_{r\|}$ indicate that the wave travels in the direction opposite to the background magnetic field.

Figure 5.5. All measurements have $|\gamma_{12}| > 0.95$ with an error less than 0.05.

did not hinder the AWPI diagnostic's ability to measure $\mathbf{k}_r$, but it did cause the $\mathbf{k}_i$ measurements to have far too much error to provide insight into the wave physics.

5.3 Discussion

The results represent an encouraging demostration of a proof-of-concept experiment for the AWPI technique. However, we have encountered limited repeatability with the excitation of electrostatic modes, regardless of whether we send harmonically-rich or sinusoidal signals to the antenna. More often than not, for experimental reasons yet to be determined, the measured dispersion relation has (1) phase velocities $\omega_r/k_r \approx c \gg c_S$, which implies that the probes are AC coupled (i.e. coupling to long-wavelength electromagnetic modes), or (2) $d\omega_r/dk_{r\perp} \ll c_S$ with $\omega(k_\perp) \neq \omega(-k_\perp)$ (i.e. no excitation of electrostatic modes, see note after Eq. 4.3). This difficulty with successfully coupling to electrostatic modes is why we do not have accompanying measurements of $k_\parallel$ in the argon plasma. However, in all cases where electrostatic modes were detected, the dispersion relation measurements were consistent with EIC wave modes and resemble the data of Figs. 5.2 and 5.5.

5.4 Chapter Summary

In this chapter we presented our measurements of the dispersion relation of electrostatic ion-cyclotron waves taken with the AWPI diagnostic both in argon and helium plasmas. These measurements agree over a wide range of frequencies with fluid and kinetic theory predictions, respectively, which we calculated using the representative plasma parameters for our RF source. The results demonstrate the diagnostic's ability to take expedited measurements of dozens of wavenumbers across different frequency ranges.

Chapter 6

Conclusions

In this dissertation, we presented the Active Wave Packet Injection (AWPI) diagnostic, a probe-based diagnostic used to measure dispersion relations in low-temperature plasmas. This diagnostic improves past active wave injection techniques by using harmonically-rich excitation signals to expedite the measurement of wavenumber as a function of frequency. We showcased the diagnostic's capabilities by manufacturing and integrating a proof-of-concept prototype into a magnetized RF plasma source to measure the dispersion relation of electrostatic ion-cyclotron waves in argon and helium.

6.1 Summary of Contributions

The AWPI diagnostic, though intrusive in nature, provides a generalizable technique to take expedited measurements of dispersion relations in plasmas. The harmonic comb generating circuit is easily adapted to produce harmonics in a variety of frequency ranges by simply changing the high-pass filter's cutoff frequency and the input square wave's fundamental frequency. Different antenna and probe designs can be implemented to excite and detect different types of wavemodes (e.g. electrostatic vs. electromagnetic or ion vs. electron waves). The ability to measure wavenumbers

at multiple frequencies simultaneously is particularly attractive for pulsed plasma experiments or experiments in which only limited exposure to the plasma environment is possible before damage occurs (e.g hollow cathode plasmas).

Our investigation of electrostatic ion-cylotron waves in a magnetized RF plasma source demostrated the AWPI diagnostic's versatile wave-shaping characteristics and compatibility with different gases. We measured the perpendicular propagation and decay of EIC waves in an argon plasma over six harmonics of the ion-cyclotron frequency. With a simple change to the circuit design, we also measured the perpendicular and parallel propagation of EIC waves in a helium plasma over two harmonics of the ion-cyclotron frequency. These measurements not only matched fluid and kinetic theory predictions, respectively, but also had a higher frequency resolution than previous work and were each obtained in a single shot.

6.2 Recommendations for Future Work

Our difficulty coupling to electrostatic modes in the RF plasma merits for a detailed investigation of broadband antenna designs for the AWPI diagnostic. While there is well-established RF matching theory to tune antennas to plasma loads [6, 101], the AWPI diagnostic requires simultaneous matching at more than one [40] or two [45] frequencies. This may be accomplished with advanced matching techniques or by exploring the effect of antenna geometry on coupling. This is also something to consider if the diagnostic is applied to real thruster systems in which the physical presence of the antenna and probes should not perturb the plasma. This means that the physical scale of the diagnostic and the frequency range probed should be appropriately scaled with respect to plasma parameters (e.g. electron Debye length or ion plasma frequency in our case) to ensure proper interpretation of the data. Our two-blade antenna geometry is adequate for the scale of our RF source and

perhaps the plume regions of plasma thrusters, but redesign would be necessary if the diagnostic were used, for example, near the channel exit of a Hall effect thruster.

Appendix A

LIF Data Reduction

A.1 f_{i0} Measurements: Ion Temperature and Drift

Using the LIF technique to resolve the background ion velocity distribution function $f_{\mathrm{i}0}$, we can determine both ion temperature and drift velocity in the direction parallel to the axis of the laser beam [9, 52, 43]. Consider the one-dimensional distribution function for a Maxwellian ion population in local thermal equilibrium,

$$f_{\mathrm{i}0}(v) = \frac{n_{\mathrm{i}}}{\sqrt{2\pi}\, v_{th,\mathrm{i}}}\, e^{-(v-v_{d,\mathrm{i}})^2/2v_{th,\mathrm{i}}^2}, \tag{A.1}$$

where $v_{th,\mathrm{i}} = \sqrt{T_{\mathrm{i}}/m_{\mathrm{i}}}$ is the ion thermal velocity and $v_{d,\mathrm{i}}$ the ion drift velocity. Sweeping the laser frequency ν_L about the atomic electron trasnsition frequency ν_0 in a plasma with this $f_{\mathrm{i}0}$ yields a Gaussian fluorescent intensity profile described by

$$\mathcal{I}^0(\nu) = \frac{\beta}{\sqrt{2\pi}\, v_{th,\mathrm{i}}}\, e^{-(\nu-\bar{\nu})^2/2\sigma^2}, \tag{A.2}$$

with peak position $\bar{\nu} = \nu_0\,(1 + {}^{v_{d,\mathrm{i}}}/_{c})$, width $\sigma = \nu_0\, v_{th,\mathrm{i}}/c$, and β a constant that depends on laser beam power, geometrical factors, and the attenuation of the collected

light. We calculate the ion drift velocity and ion tempertature by fitting $\mathcal{I}^0$ to the measured fluorescent signal and backing out its peak position and width, respectively.

A.2 f_{i1} Measurements: Plasma Dispersion Relation

If a traveling electrostatic wave with frequency ω is present in the plasma, the compressions and rarefactions of plasma density produce a time-dependent perturbation $f_{\mathrm{i}1}$ to the background distribution function [54, 63]. This perturbation causes the fluorescent signal to have two components (in-phase $\mathcal{I}^{IP}$ and out-of-phase $\mathcal{I}^{Q}$ with respect to the wave) oscillating at ω. We can use the LIF technique to resolve both f_1 components to yield wave dispersion relation measurements. We first model the effect of the electrostatic wave on the ion distribution function using the Vlasov equation for ion motion

$$\frac{\partial f_{\mathrm{i}}}{\partial t} + \mathbf{v} \cdot \frac{\partial f_{\mathrm{i}}}{\partial \mathbf{x}} + \frac{e}{m_{\mathrm{i}}}(\mathbf{E} + \mathbf{v} \times \mathbf{B}) \cdot \frac{\partial f_{\mathrm{i}}}{\partial \mathbf{v}} = 0, \tag{A.3}$$

where the electric and magnetic fields $\mathbf{E}$ and $\mathbf{B}$ have both background (0th order) and perturbation (1st order) components. We consider the case with $\mathbf{E}_0 = 0$ and, since the wave is electrostatic, $\mathbf{E}_1 = -i\mathbf{k}\Phi_1 e^{i(\mathbf{k}\cdot\mathbf{x}-\omega t)}$ and $\mathbf{B}_1 = 0$. Substituting into the above equation and asssuming a three-dimensional magnetized Maxwellian background distribution function

$$f_{\mathrm{i}0}(\mathbf{v}) = n_{\mathrm{i}} \left(\frac{1}{2\pi v_{th\parallel}^2}\right)^{1/2} e^{-(v_\parallel - v_d)^2/2v_{th\parallel}^2} \left(\frac{1}{2\pi v_{th\perp}^2}\right) e^{-v_\perp^2/2v_{th\perp}^2}, \tag{A.4}$$

we obtain the first order equation

$$\frac{\partial f_1}{\partial t} = i\frac{q_{\mathrm{i}}\phi_1}{m_{\mathrm{i}}} e^{i(\mathbf{k}\cdot\mathbf{x}-\omega t)}\, \mathbf{k} \cdot \frac{\partial f_0}{\partial \mathbf{v}} \tag{A.5}$$

for the perturbation f_1. This equation is solved through the method of characteristics to yield an expression for $f_1(\mathbf{v})$ [31]. Since the LIF diagnostic only resolves velocities in one spatial dimension (say $\hat{x}$), we integrate the full expression for $f_1(\mathbf{v})$ over v_y and v_z, giving the result $f_1(v_x) = \hat{f}_1(v_x)e^{i(\mathbf{k}\cdot\mathbf{x}-\omega t)}$, where

$$\begin{aligned}\hat{f}_1(v_x) =& \frac{q_\mathrm{i}\phi_1}{\pi m_i v_{th\perp,\mathrm{i}}^2} f_0(v_x) \sum_{n,m} \left(1 + Z(\zeta_{n+m})\zeta_0\right) J_m\left(\frac{k_\perp v_x}{\omega_{c,\mathrm{i}}}\right) \\ &\times e^{-im\pi/2} e^{i(m+n)\theta} e^{ik_\perp \sin\theta v_x/\omega_{c,\mathrm{i}}} e^{-a^2/8} e^{-g^2/4} \sum_l I_{(n+l)/2}\left(\frac{a^2}{8}\right) I_l\left(\frac{ag}{2}\right) e^{il\pi/2}\end{aligned} \tag{A.6}$$

with $a = \sqrt{2}k_\perp v_{th\perp,\mathrm{i}}/\omega_{c,\mathrm{i}}$, $g = \sqrt{2}k_\perp \cos\theta\, v_{th,\mathrm{i}}/\omega_{c,\mathrm{i}}$, $\theta = \tan^{-1}(k_y/k_x)$, $J_m(x)$ the nth order Bessel function of the first kind, and the rest of the symbols as defined in Eq. 4.1. The real and imaginary parts of $\hat{f}_1$ are related to the in-phase $\left(\mathcal{I}^{IP}_{\mathrm{meas}}\right)$ and out-of-phase $\left(\mathcal{I}^{Q}_{\mathrm{meas}}\right)$ measurements of fluorescent intensity, respectively. We can fit the analytical expression in Eq. A.6 to laser frequency sweeps of both components of the fluorescent intensity and determine the best fit values of the free parameters $k_\perp$ and θ, thereby measuring the dispersion relation of the electrostatic wave. Appendix A.3 details the data reduction and error analysis we follow in the fitting procedure, including considerations for the other free parameters ϕ_1 and $k_\parallel$, data phase correction and normalization, and the inverse χ^2 metric we use to evaluate the goodness of the fit [54, 102].

A.3 f_1 Data Reduction and Error Analysis

We follow the procedure outlined in Refs. [54, 43] to make dispersion relation measurements of electrostatic plasma waves using the LIF diagnostic. The data processing for determining $k_\perp$ and θ involves three steps: (1) data phase correction, (2) free parameter reduction, and (3) goodness-of-fit evaluation. The data sets processed are the in-phase and out-of-phase measurements of fluorescent intensity as a function of laser

frequency. While $\mathcal{I}^{IP}_{\text{meas}}$ and $\mathcal{I}^{Q}_{\text{meas}}$ are real quantities, we define $\mathcal{I}_{\text{meas}} = \mathcal{I}^{IP}_{\text{meas}} + i\,\mathcal{I}^{Q}_{\text{meas}}$ for convenience during the data processing.

Since a phase difference φ exists between the source signal used as the LIA's reference and the locally measured plasma density fluctuations, the collected fluorescent intensity profiles exhibit a phase dependence $\mathcal{I}_{\text{meas}} \propto e^{i\varphi}\hat{f}_1$ which we must remove before applying the theoretical model from Eq. A.6. We calculate the phase as [54]

$$\varphi = \tan^{-1}\frac{\int \mathcal{I}^{Q}_{\text{meas}}\,d\nu}{\int \mathcal{I}^{IP}_{\text{meas}}\,d\nu} \tag{A.7}$$

and multiply $\mathcal{I}_{\text{meas}}$ by a factor of $e^{-i\varphi}$ to produce the phase-corrected data sets $\mathcal{I}_{\text{meas,c}}$.

The real and imaginary parts of the analytical expression for $\hat{f}_1$ provide a system of two equations to which to fit our two corrected data sets $\mathcal{I}^{IP}_{\text{meas,c}}$ and $\mathcal{I}^{Q}_{\text{meas,c}}$. However, the fitting is underdetermined as there are four free parameters: $k_\perp$, $k_\parallel$, θ, and ϕ_1. To remedy this, we first note that ϕ_1 appears only as a multiplicative prefactor in Eq. A.6, so normalization of the intensity data and fitting function removes its presence. We find the largest absolute value of $\mathcal{I}^{IP}_{\text{meas,c}}$ and the frequency $\nu_{\max}$ at which it occurs. We choose to normalize the data by the largest absolute value of the in-phase component so that

$$\overline{\mathcal{I}}_{\text{meas,c}}(\nu) = \frac{\mathcal{I}_{\text{meas,c}}(\nu)}{\left|\mathcal{I}^{IP}_{\text{meas,c}}(\nu_{\max})\right|}. \tag{A.8}$$

We correspondingly normalize our fitting function to define

$$\bar{f}_1(v_x) = \frac{\hat{f}_1(v_x)}{\left|\Re\{\hat{f}_1(v_{x,\max})\}\right|}, \tag{A.9}$$

where $v_{x,\max} = \frac{c}{\nu_0}(\nu_0 - \nu_{\max})$ by Eq. 2.3. To account for $k_\parallel$, we note that we can solve the electrostatic dispersion relation in Eq. 4.1 to calculate $k_\parallel$ as a function of $k_\perp$, leaving only $k_\perp$ and θ as free parameters for fitting $\bar{f}_1$ to $\overline{\mathcal{I}}_{\text{meas,c}}$.

We search $(k_\perp, \theta)$ space for the point which gives the best parameters to fit the data. The metric we employ to find said parameters consists of a χ^2 analysis that evaluates how well $\bar{f}_1(v_x)$ matches $\overline{\mathcal{I}}_{\mathrm{meas,c}}(\nu)$ given measurement error σ [102]. For each $(k_\perp, \theta)$ point considered, we calculate

$$\chi^2 = \sum_{p=1}^{N} \frac{1}{\sigma^2_{(p)}} \left| \bar{f}_1^{(p)}(v_x) - \overline{\mathcal{I}}^{(p)}_{\mathrm{meas,c}}(\nu) \right|^2 \tag{A.10}$$

over all collected wavelength points, with each $\sigma_{(p)}$ the sum in quadrature of the error of the in-phase and out-of-phase components of the fluorescent intensity and N the number of wavelengths sampled. Plotting $1/\chi^2$ in the $(k_\perp, \theta)$ space sampled we identify the best fit parameters as the location of the peak of the distribution and their uncertainty as the full width half maximum (FWHM) of the distribution.

Appendix B

Numerical Algorithms for Finding and Tracking Complex Roots

To perform the procedure outlined in Sec. 2.2, we base our method for determining the initial locations of the roots of $\mathcal{D}(\omega, \mathbf{k})$ on previous work [86, 87] which took advantage of the analytic (or meromorphic at worst) nature of dispersion relations commonly encountered in plasma physics. We do not use any graphical methods for this task; instead, we devise a root-searching protocol that only requires input from a user at the start and has the potential for improved performance if implemented with parallel programming practices. This provides the desired versatility for numerically characterizing plasma waves and instabilities in arbitrary parameter spaces.

B.1 Global Root-Finding

Consider the meromorphic function $f(z)$ and the analytic function $g(z)$ over a simply-connected open region $\mathcal{R} \in \mathbb{C}$. Assuming that $f(z)$ is non-zero on the positively-oriented closed contour Γ which bounds $\mathcal{R}$ (see Fig. B.1), Cauchy's Argument Prin-

ciple states that [103]

$$\frac{1}{2\pi i}\oint_{\Gamma} g(\zeta)\frac{f'(\zeta)}{f(\zeta)}\,d\zeta = \sum_k m_k g(z_k) - \sum_p d_p g(z_p), \tag{B.1}$$

where z_k and z_p are the roots and poles of $f(z)$ contained in $\mathcal{R}$ with multiplicities m_k and d_p, respectively. If $\mathcal{R}$ does not contain any of the poles of $f(z)$, then the above summation over p disappears, which when combined with the choice $g(z) = z^t$ allows us to define the contour integral

$$\mathfrak{I}_t = \frac{1}{2\pi i}\oint_{\Gamma} \zeta^t\,\frac{f'(\zeta)}{f(\zeta)}\,d\zeta = \sum_k m_k z_k^t. \tag{B.2}$$

For the case $t = 0$, the integral gives the sum of the multiplicities of the roots contained in $\mathcal{R}$. If the region contains only one root, then for the case $t = 1$ the integral gives the value of the root times its multiplicity. Note that if $\mathcal{R}$ only contains a simple root of $f(z)$, then $\mathfrak{I}_0 = 1$ and $\mathfrak{I}_1$ is the value of that root.

For our application, the function $f(z)$ corresponds to a dispersion relation $\mathcal{D}(\omega, \mathbf{k}; p_i)$ after restricting it to a function of a single parameter as discussed in Section 2.2. For example, the function

$$\mathcal{D}^{[0]}(\omega) = \mathcal{D}(\omega, \mathbf{k}; p_i)\Big|_{\mathbf{k}^{[0]}, p_i^{[0]}} \tag{B.3}$$

would subsitute in for $f(z)$ above in order to search for the location of the roots $\omega^{[0]}(\mathbf{k}^{[0]}; p_i^{[0]})$ in the complex ω-plane. The poles of many $\mathcal{D}(\omega, \mathbf{k}; p_i)$ studied in plasma physics can be analytically removed from $\mathcal{D}$ or located beforehand in complex plane [104, 31], ensuring only roots contribute to $\mathfrak{I}_t$, as written in Eq. B.2. Unfortunately, it is unlikely that detailed enough *a priori* knowledge about the possible value of each root is at hand to choose contours Γ that enclose only one root (if it were, this whole procedure of global root-finding would not be needed). Moreover,

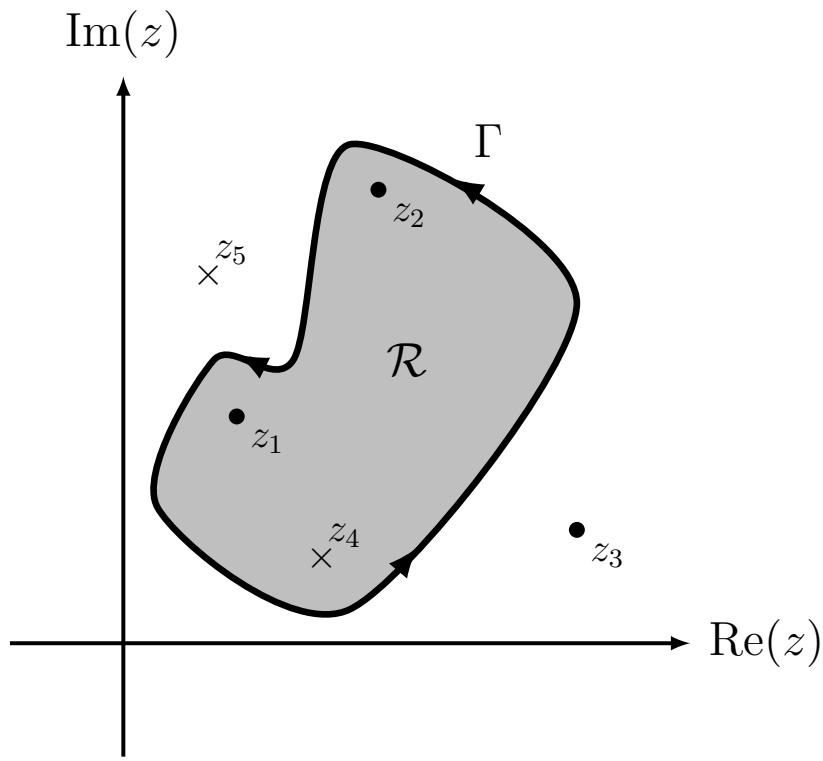

Figure B.1. The roots (•) and poles (×) of $f(z)$ are located on the complex z-plane. The contour Γ, which delimits $\mathcal{R}$, encloses two roots (z_1, z_2) and one pole (z_4), so only these will contribute to the value of the integral in Eq. B.1.

the dispersion relations studied in plasma physics can commonly have an unknown (possibly infinite) number of complex roots, so it is not even clear how many roots might be present in the region of $(\omega, \mathbf{k})$-space of interest.

Given these challenges, we design PRINCE to autonomously determine the number of roots in a region $\mathcal{R}$ and calculate initial estimates for their locations. PRINCE conducts the search-and-refine procedure described in Section B.3 to focus down on the location of a single root (whether simple or degenerate) by evaluating the contour integral in Eq. B.2 and using a series of criteria to determine whether (1) a single root has been found or (2) the region $\mathcal{R}$ needs to be divided into smaller subregions in order to isolate the roots contained in it. For simplicity, we illustrate the procedure for the specific case of Eq. B.3, though PRINCE can also handle the cases where any one of the components of $\mathbf{k}$ is left as the independent variable for the dispersion

relation (e.g. $f(z)$ is $\mathcal{D}(k_y)$ by simplifying $\mathcal{D}(\omega, \mathbf{k}; p_i)$ using initial values for ω, k_x, k_z, and the p_i).

B.2 Specification of Initial Search Region

The choice for the initial region $\mathcal{R}$ over which to search for roots of a dispersion relation depends on the physics to investigate. Typically, target frequency or wavelength ranges based on physical considerations restrict the real values of ω or $\mathbf{k}$ (for example, only looking at waves with frequencies in the MHz range or with wavelengths smaller than the system dimensions). Similarly, the types of modes to study restrict the imaginary component of ω or $\mathbf{k}$. These could be purely propgating modes (in which no energy exchanges between the wave and the plasma), damping modes (in which the wave deposits energy into the plasma), or growing modes (in which the wave extracts energy from the plasma). Fig. B.2 exemplifies the different regions over which PRINCE searches for roots in the complex ω-plane based on the type of modes investigated. Since Eq. B.1 assumes that $f(z)$ is non-zero on the contour Γ, the presence of purely propagating or purely evanescent modes (which correspond to roots located on the real axis or on the imaginary axis, respectively) precludes us from using contours that lie on the coordinate axes. While indenting the contour Γ about the root remedies this problem analytically [103], such a strategy is not viable for PRINCE since we do not know beforehand whether a root lies on the contour. Instead, we offset the contour from the axes when necessary by 1% of the upper bound for ω or $\mathbf{k}$.

Alternatively, non-relativistic and quasi-neutrality considerations (which are commonly applicable to plasma thruster discharges) can determine the extent of the search region in the real and imaginary directions if no other bounds are otherwise specified. For a search in the complex ω-plane, PRINCE bounds $\mathcal{R}$ above by roughly

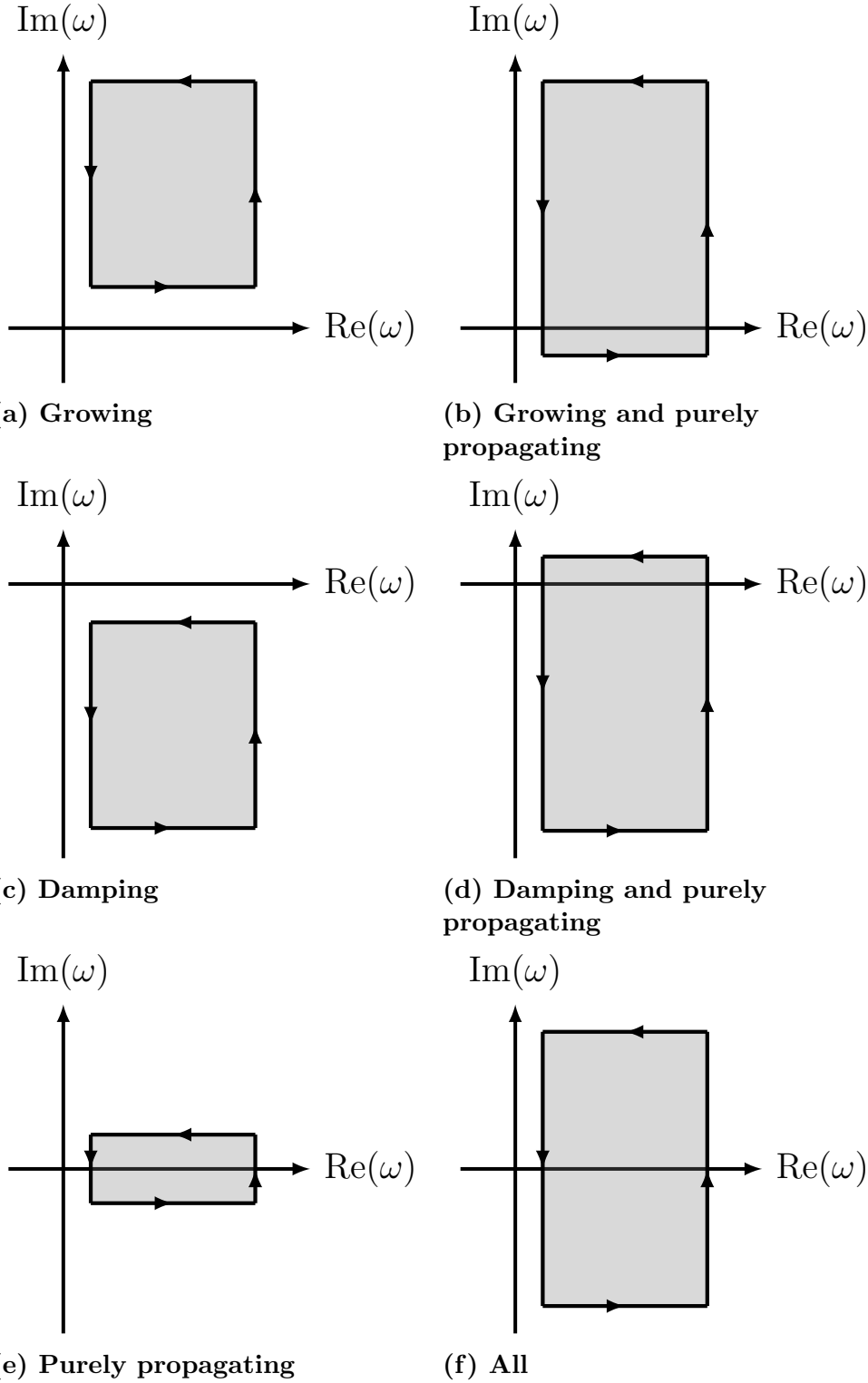

(a) Growing

(b) Growing and purely propagating

(c) Damping

(d) Damping and purely propagating

(e) Purely propagating

(f) All

Figure B.2. The different types of initial search regions correspond to searches for different types of modes. The offsets from the axes are exaggerated for clarity. The classification of stable or unstable for this example of roots in the complex ω-plane corresponds to the normal mode convention from Eq. 1.3.

non-relativistic particle motion over an electron Debye length, i.e. $\omega\lambda_{D,\mathrm{e}} \leq c$. For a search in the complex $\mathbf{k}$-plane, PRINCE bounds $\mathcal{R}$ above such that the corresponding wavelength is greater than the local Debye length, i.e. $|\mathbf{k}| = 2\pi/\lambda \leq 2\pi/\lambda_{D,\mathrm{e}}$.

B.3 Algorithm Implementation

Once the initial search region has been defined, the algorithm to find the number and locations of the initial roots of a dispersion relation $\mathcal{D}(\omega)$ is as follows [86]:

1. Divide the search region $\mathcal{R}$ in the complex ω-plane into rectangular cells.

2. For each cell, evaluate $\mathfrak{I}_0$ numerically along the delimiting contour.

3. For each cell, take one of three actions based on the value of $\mathfrak{I}_0$:

   (a) If $\mathrm{Re}(\mathfrak{I}_0) = 1$ within tolerance, a simple root was found, so calculate and store $\mathfrak{I}_1$ as the estimate for its location.

   (b) If $\mathrm{Re}(\mathfrak{I}_0) = 0$ within tolerance, no roots are contained in the cell, so disregard it.

   (c) If $|\,\mathrm{Re}(\mathfrak{I}_0)| > 0$ and $|1 - \mathrm{Re}(\mathfrak{I}_0)| > 0$ within tolerance, the cell may contain unresolved roots, so label the cell as suspect.

4. If there are no suspect cells, all roots contained in $\mathcal{R}$ were found and the search terminates. Otherwise, for each suspect cell there are two options:

   (a) If $\mathcal{D}\left(\mathfrak{I}_1/\,\mathrm{Re}(\mathfrak{I}_0)\right) = 0$ within tolerance, the cell contains a single degenerate root with multiplicity $\mathrm{Re}(\mathfrak{I}_0)$, so store $\mathfrak{I}_1/\,\mathrm{Re}(\mathfrak{I}_0)$ as the estimate for its location.

   (b) If $\mathcal{D}\left(\mathfrak{I}_1/\,\mathrm{Re}(\mathfrak{I}_0)\right) \neq 0$ within tolerance, the suspect cell contains unresolved roots, so recursively apply the algorithm to the cell.

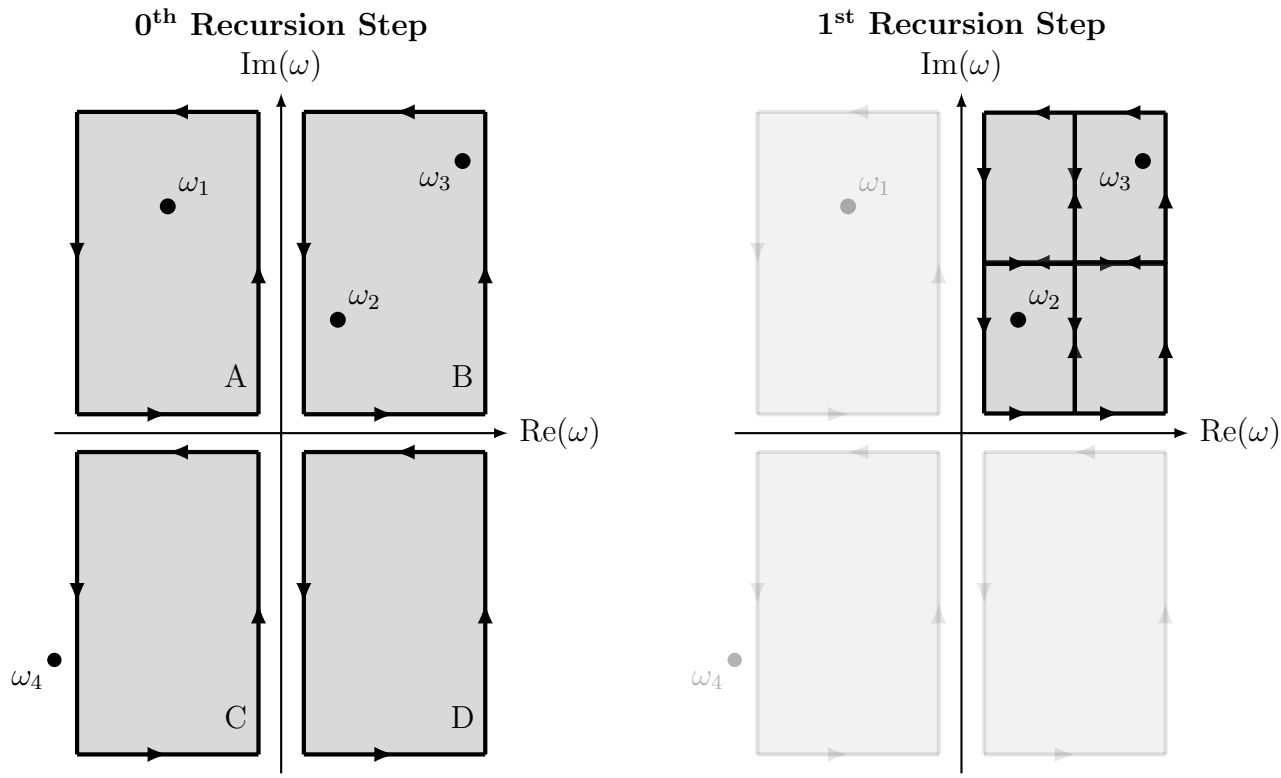

Figure B.3. PRINCE determines in the 0th Recursion Step that cells C and D contain no roots while cell A only contains root ω_1. Cell B is suspect, so it is subdivided into smaller cells in the 1st Recursion Step to resolve roots ω_2 and ω_3. As root ω_4 is not inside any of the search cells, it is ignored.

All tolerances are set to 0.01, i.e. $\text{Re}(\mathfrak{I}_0) = 1$ is within tolerance if $|\text{Re}(\mathfrak{I}_0) - 1| < 0.01$.

Figure B.3 illustrates this procedure for the example of four zeros, three of which correspond to physically-relevant linearly unstable wavemodes. The sign of the real part of the root indicates whether the wave's phase velocity is parallel or anti-parallel to $\mathbf{k}$. The initial search region $\mathcal{R}$ is the union of the four disjoint rectangular regions, one in each quadrant of the complex plane and each off-set from the real and imaginary axes by the predefined distances discussed in Section B.2. PRINCE recursively applies the search algorithm only to the suspect cells containing unresolved roots (Cell B in this example). The other cells are discarded once the number and locations of any resolved roots are stored.

B.4 Iterative Local Root-Tracking

The global root-finding algorithm determines the number of roots contained in $\mathcal{R}$ and estimates their values for the initial set of conditions $\mathbf{k}^{[0]}$ and $p^{[0]}$. With this information, a more efficient root-finding algorithm (the Newton-Raphson method in PRINCE) can now be used to calculate the value of the roots as we iteratively vary one of the wave parameters away from these initial conditions. For example, once the roots $\omega_j^{[0]}$ of $\mathcal{D}^{[0]}(\omega) = \mathcal{D}(\omega, \mathbf{k}^{[0]}; p_i^{[0]})$ are located, we can track their location in the complex ω-plane as we vary k_x away from $k_x^{[0]}$. At the nth step of the iteration, we first re-evaluate the dispersion relation for the new value $k_x^{[n]}$ to obtain $\mathcal{D}^{[n]}(\omega)$. To find the new locations $\omega_j^{[n]}$ of each root, we use $\omega_j^{[n-1]}$ as the initial guess for the root-finding algorithm. The procedure based on complex integration described in the previous section could be applied again, but its computation is significantly more costly, particularly compared to the Newton-Raphson method. This iteration produces a numerical characterization of each wavemode $\omega_j(k_x)$ that was initially found.

Appendix C

Plasma Rocket Instability Characterizer[1]

In this appendix we describe the initial implementation of the **P**lasma **R**ocket **In**stability **C**haracterize**r** (PRINCE), an interactive software tool which enables the numerical characterization of plasma waves' and instabilities' dependence on plasma parameters across relevant frequency or wavenumber domains. We describe the frontend graphical user interface (GUI) which allows for versatile data input and parametric control of the search parameters. We also present a proof-of-concept reproduction of previous work which studied unstable Esipchuk-Tilinin wavemodes present in Hall effect thrusters to validate the performance of PRINCE.

C.1 Frontend Graphical User Interface

We integrate the procedures described in the previous appendix into a software program written in Wolfram's Mathematica 10.4. While other platforms or coding lan-

[1]This chapter is based on work previously presented in [105]: Rojas Mata, S., Choueiri, E. Y., Jorns, B. A., and Spektor, R., "PRINCE: A Software Tool for Characterizing Waves and Instabilities in Plasma Thrusters," *52nd AIAA/SAE/ASEE Joint Propulsion Conference, Salt Lake City, UT, 2016.*

guages provide better computational performance, we made a trade-off between optimal computational power and the built-in ease for GUI design and analytical manipulations which Mathematica provides. The resulting 3-panel interactive interface controls the input of the specific dispersion relation $\mathcal{D}$ to study, the region in $(\omega, \mathbf{k})$-space to search for roots, and the plasma parameters p_i.

C.1.1 Plasma Parameters Panel

The import of the plasma parameters p_i is done through the panel shown in Fig. C.1. Each plasma parameter available has a small unfolding menu for specifying spatial dependencies and the filepath to access the data files. If the plasma parameter does not have a spatial dependence (0D), then just a value input box appears. Whether the input of a particular parameter is necessary or optional depends on the dispersion relation chosen (see Section C.1.2). Fig. C.2 shows the different levels of the parameter menus for one- or two-dimensional spatial dependencies. Checking a parameter's box will select the parameter for import. The information requested in the menu must be specified for proper import of the data (see below for formatting notes); if not, an error dialog will appear when the 'Import' button is pressed. Each 'Clear' button clears all import information for that parameter. Unchecking the check box removes the parameter from import but does not clear any specified information.

For each plasma parameter checked, the following must be specified:

- Dimensionality: what the spatial dimensionality of the data is
- Variable dependence: on which Cartesian variables does the data depend
- Filepath: where in the computer is the data stored

In addition to the plasma parameters, the gas and the units of the spatial coordinates are selected in this panel. If all necessary information is specified, pressing the 'Import' button on the bottom right will read the data into PRINCE and display

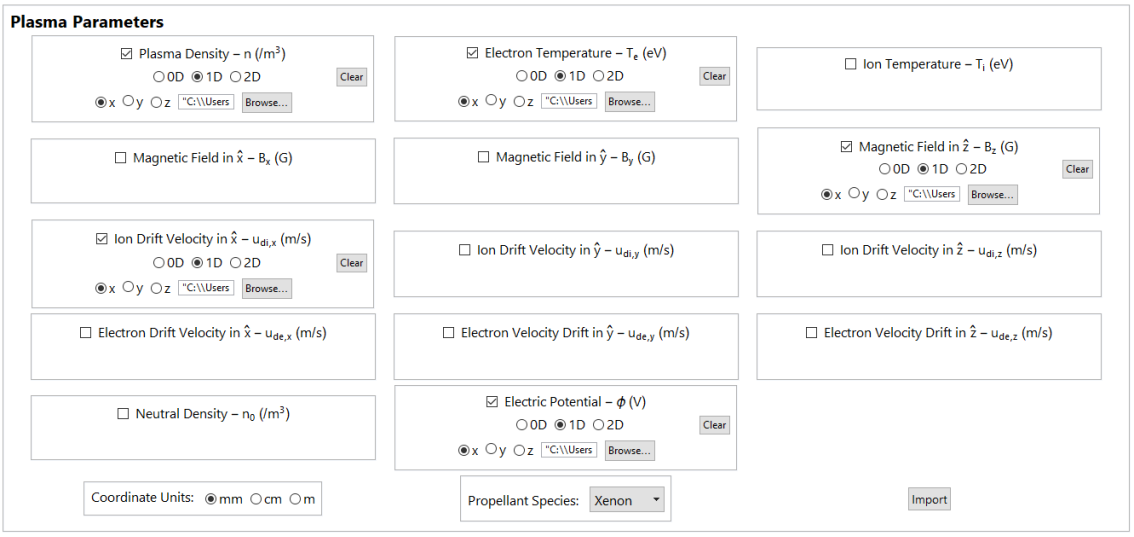

Figure C.1. PRINCE offers several dimensionality and Cartesian-coordinate-dependence options for fourteen different input plasma parameters. The user also specifies the units of the input spatial discretization as well as the gas.

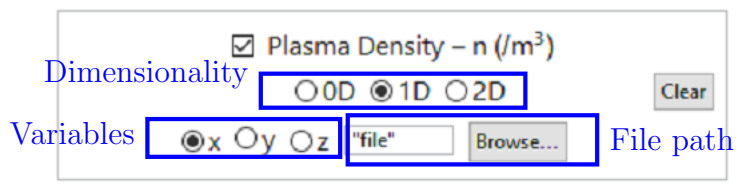

Figure C.2. The user must specify all fields in order to import the file.

a success dialog. Otherwise, an error dialog detailing the missing information will appear.

If the plasma parameter has no spatial dependence (0D dimensionality), only a scalar value needs to be provided in the input value field.[2] If there is a spatial dependence, then the data file must be a CSV text file where the last column is the parameter values and the preceding columns (one for a 1D dependence or two for a 2D dependence) are the spatial coordinate values. For 2D data, the order of the variables in the columns of the data file must match the order of the variables selected in the variable dependence section of the menu. So, if the variable dependence chosen is "x, z", the first column in the data file should be the x-coordinate values and the

[2]Note that Mathematica does not recognize "E" notation for order of magnitude. Instead a number like 5×10^{18} needs to be input as 5*10^18, not 5E18.

second the z-coordinate values. The number of coordinates and their values in any one direction must be the same for all parameters which depend on that direction; PRINCE is not designed to interpolate or extrapolate values for missing coordinate points. The units of the parameter must match those displayed in the header of the parameter's menu (e.g. eV for ion or electron temperature).

C.1.2 Solver Settings Panel

The dispersion relation to study is selected in the panel shown in Fig. C.3. The dropdown menu contains the following pre-programmed dispersion relations:

- Simplified Esipchuk-Tilinin waves
- Long wavelength gradient drift waves
- High-frequency $\mathbf{E} \times \mathbf{B}$ drift waves
- Damped warm Langmuir waves
- (Simplified) Magnetized electrostatic waves in a warm plasma
- Low-frequency MHD waves
- Forward electrostatic ion-cyclotron waves
- Electrostatic ion acousitc modes

There is also an option for a user-specified dispersion relation which is easily defined in an auxiliary file (see Appendix D). Each pre-programmed dispersion relation displays in red until all the necessary plasma parameters are checked in the 'Plasma Parameters' panel. The necessary and optional parameters or gradients of parameters display in the box to the right of the dispersion relation. To the left is a graphical depiction of the coordinate geometry and vector fields selected which provides a check that the spatial configuration of the system is set up correctly.

In the bottom half of the panel, the bounds for the search region in the complex plane and details of the iteration process are specified. PRINCE can either solve for complex values of ω over an iteration of real values of one of the $\mathbf{k}$ components or for complex values of one of the $\mathbf{k}$ components over an iteration of real values of ω. The iteration variable as well as its range and resolution should be specified first. An iteration over ω requires specification of which component of $\mathbf{k}$ to solve for; similarly, an iteration over a $\mathbf{k}$ component requires specification of which component to iterate over. Both options leave two of the three $\mathbf{k}$ components as free parameters, so their values must be specified either as constant or propotional to the third solved for/iterated over component. The labels in the panel dynamically update as the choices are made to provide clarity in the process. In the bottom left corner, the bounds for the real and imaginary parts of the solved for variable are specified to define

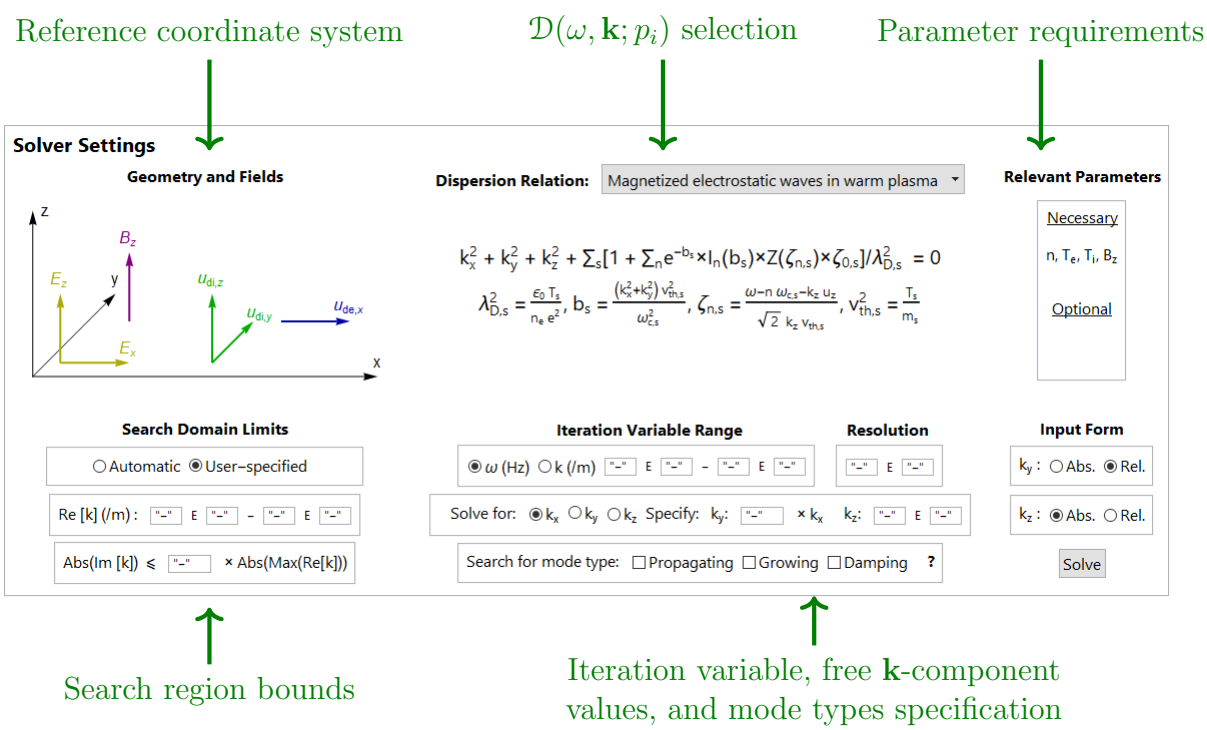

Figure C.3. The user specifies the dispersion relation to study from the drop-down menu and the details of the $(\omega, \mathbf{k})$-space sweep in the various fields.

the initial search region. Alternatively, automatic limits based on quasineutrality and relativistic considerations can be used (see Section B.2).

The final step is to choose which types of modes to search for: purely propagating, growing, damping, or a combination of these. The sign convention used to define whether wavemodes are growing or damping is that of Fourier modes of the form $\exp[i(\mathbf{k}\cdot\mathbf{x}-\omega t)]$ (see Eq. 1.3). This means that modes with a positive ω_i are growing modes while damping modes have the opposite signature. Analogously, modes with a negative $\mathbf{k}_i$ are growing modes while damping modes have the opposite signature. Purely propagating modes have $\omega_i = \mathbf{k}_i = 0$. The signature of either ω_r or $\mathbf{k}_r$ indicate the direction of propagation relative to the coordinate system used.

Once all the necessary information in this panel is set, pressing the 'Solve' button starts the search for all the roots of the dispersion relation located inside the specified complex-plane region at each spatial coordinate point. If there is an error with the input information an error dialog will appear detailing the problem. Once the global root-finding procedure resolves all the roots in the search region, the local root-tracking routine characterizes each one of them as a function of the iteration variable. Progress dialogs continuously display as PRINCE computes until a final completion dialog appears.

C.1.3 Data Visualization Panel

This bottom panel provides some simple plotting routines to study results. In the 'Heat Maps' section, the 'Binary Instability Spatializer' button brings up a spatial heat map that indicates at which grid points instabilites were found i.e. coordinate points where $\mathrm{Im}(\omega) > 0$ or $\mathrm{Im}(k) < 0$. The 'Dominant Unstable Mode' buttons bring up spatial heat maps of the real part of either the wavenumber or frequency of the unstable mode with biggest growth rate at each coordinate point.

In the 'Single Branch Options' section, pressing the 'Output Results' button creates a new subdirectory to export the results of the characterization for each root. The data file names begin with the spatial coordinates where the root was found followed by a "_BX" suffix where the X denotes the branch number of the root. The files are CSV text files where the first column contains the values of the iteration variable, the second column contains the real part of the root, and the third column contains the imaginary part of the root. Once the raw data has been output, the 'Plots' button in the 'Single Branch' section allows the user to plot the real and imaginary parts of a root as a function of the iteration variable.

C.2 Validation of PRINCE

C.2.1 Esipchuk-Tilinin Dispersion Relation Study

We validate PRINCE by reproducing previous work [11] which investigated instabilities arising in a Hall effect thruster channel from solutions to the Esipchuk-Tilinin dispersion relation [106]

$$\frac{1}{\omega_{p,\mathrm{i}}^2} - \frac{1}{(\omega - k_x v_{d,\mathrm{i}})^2} + \frac{1}{\omega_{c,\mathrm{e}}\omega_{c,\mathrm{i}}} + \frac{1}{k_\perp^2 v_A^2} - \frac{k_y(u_{de} - u_B)}{k_\perp^2 v_{d,\mathrm{i}}^2(\omega - k_y u_{de})} = 0. \tag{C.1}$$

Here $\omega_{p,\mathrm{i}}$ is the ion plasma frequency, $v_{d,\mathrm{i}}$ the axial ion drift velocity, $\omega_{c,\mathrm{e}}$ and $\omega_{c,\mathrm{i}}$ the electron and ion cyclotron frequencies, v_A the Alfvén velocity, u_{de} the azimuthal $\mathbf{E}\times\mathbf{B}$ electron drift velocity, and u_B the magnetic drift velocity. Ref. [11] restricted the frequency range considered such that $(\omega - k_x v_{d,\mathrm{i}})^2 \ll \omega_{c,\mathrm{e}}\omega_{c,\mathrm{i}} \ll \omega_{p,\mathrm{i}}^2$ and $(\omega - k_x v_{d,\mathrm{i}})^2 \ll k_\perp^2 v_A^2$ to simplify the dispersion relation to

$$\frac{1}{(\omega - k_x v_{d,\mathrm{i}})^2} + \frac{k_y(u_{de} - u_B)}{k_\perp^2 v_{d,\mathrm{i}}^2(\omega - k_y u_{de})} = 0, \tag{C.2}$$

so this is the version we analyze with PRINCE. Extracted experimental data sets with xenon as propellant [107] with a spatial resolution of 1 mm for electron density, electric potential, and radial magnetic field, reproduced in Fig. C.4(a)-(c), served as the input to calculate $v_{d,\mathrm{i}}$, $u_{de} = -E_x/B_z$, $\omega_{c,\mathrm{i}} = eB_z/m_\mathrm{i}$, and $u_B = \frac{\partial B_z}{\partial x} v_{d,\mathrm{i}}/\omega_{c,\mathrm{i}}$ in both the previous work and our reproduction.

C.2.2 Procedure and Results

Ref. [11] characterized instabilities arising in the mostly azimuthal propagation ($k_y = 10k_x$) of the mode with $k_\perp = \sqrt{k_x^2 + k_y^2} = 1/z$, where z is the local radius of curvature of the channel (refer to Fig. 1.2). The results comprise computations of the complex roots $\omega(k_x, k_y)$ using the analytical solution of Eq. C.2. Fig. 9(f) in Ref. [11] plots the real part of the roots at the locations where the root has a positive imaginary part, signifying that the mode is unstable. To reproduce this analysis, we use PRINCE to numerically characterize the zeros $\omega(\mathbf{k})$ of Eq. C.2. We set $k_z = 0$ and $k_y = 10k_x$ and vary k_x between 2 /m and 4 /m at a resolution of 0.05/m. We extract the value of ω corresponding to the mode $k_\perp = 1/z$ for each spatial point from the raw output data to produce Fig. C.4(d), our reproduction of Fig. 9(f) from Ref. [11]. The locations where instabilities arise match well, corresponding as expected to the region in the channel where the radial magnetic field gradient is negative with respect to the axial variable ($\partial B_z/\partial x < 0$). The frequency range (20-50 kHz) is also comparable, differences no larger than 10 kHz potentially due to different interpolation schemes used to calculate the gradients and secondary plasma quantities.

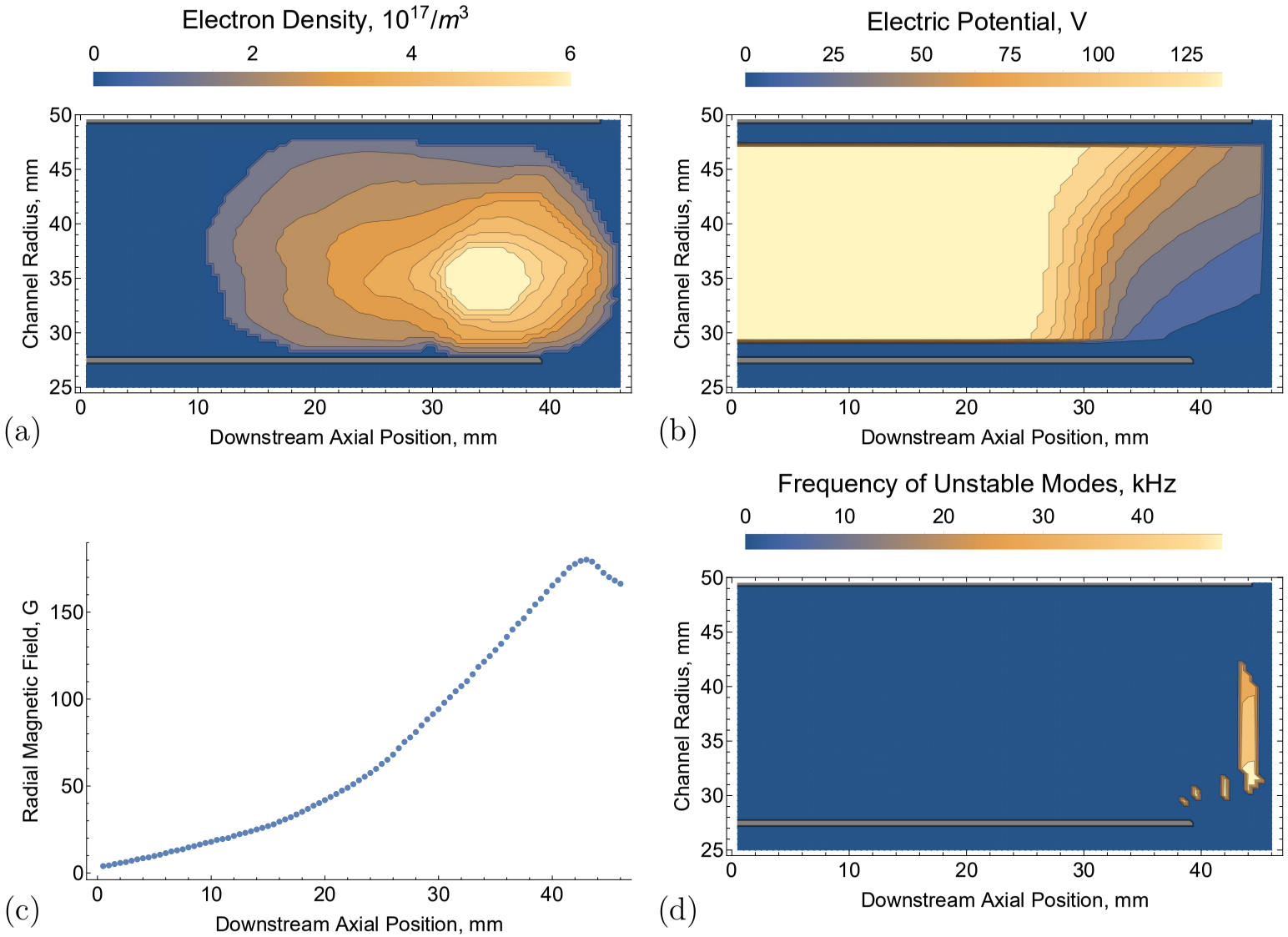

Figure C.4. Profiles of the electron density, electric potential, and radial magnetic field extracted from Ref. [107] display in panels (a), (b), and (c), respectively. The real frequency of the unstable modes of Eq. C.2 with $k_\perp = 1/z$ and mostly azimuthal propagation ($k_y = 10k_x$) are displayed in panel (d). Blue denotes stable regions.

Appendix D

PRINCE Examples

In this appendix we provide two examples of using PRINCE to characterize a pre-programmed or custom dispersion relation with sample data sets. These data extracted from Ref. [107] are axial profiles at constant radius of xenon plasma properties inside the channel of a Hall thruster.

D.1 Pre-Programmed Dispersion Relation: Esipchuk-Tilinin

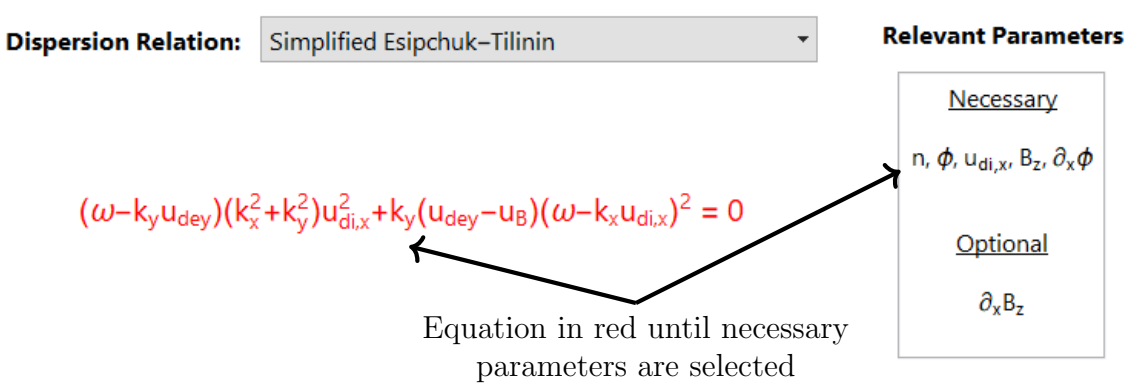

Figure D.1. Esipchuk-Tilinin Dispersion Relation Display

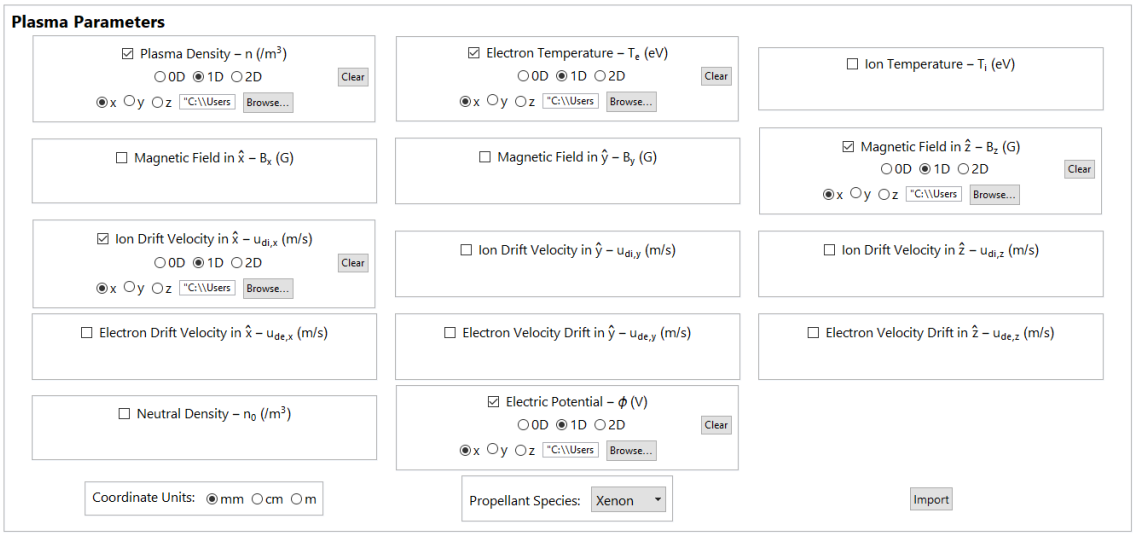

Figure D.2. Data Import for Esipchuk-Tilinin Example

In this example we will characterize wave modes arising as solutions to a simplified version of the Esipchuk-Tilinin dispersion relation [106, 11]. Instead of considering the cylindrical geometry of the thruster, this model uses a Cartesian system with $\hat{r} \to \hat{z},\ \hat{\theta} \to -\hat{y},\ \hat{z} \to \hat{x}$. Choosing this dispersion relation from the drop down menu indicates that the necessary parameters are plasma density, electric potential (and its gradient in $\hat{x}$), ion drift velocity in $\hat{x}$, and magnetic field in $\hat{z}$, as seen in Fig. D.1. A gradient in $\hat{x}$ for the magnetic field is an optional parameter which will change the form of the dispersion relation. We input the sample data files through the "Plasma Parameter" panel as seen in Fig. D.2. Note that the electron temperature data is not necessary for this dispersion relation but may be input anyway. The propellant gas is xenon and the grid units are millimeters.

Following the analysis of Ref. [11], we will solve for ω as a function of k_x for primarily azimuthal modes with $k_y = 10k_x$ and $k_z = 0$. We iterate k_x over the range 1-100 m^{-1} with a resolution of 0.1 m^{-1}. For this example we want to characterize growing wave modes in the low kHz range, so we set the search domain limits between 1 kHz and 100 kHz. Fig. D.3 shows these settings input into PRINCE.

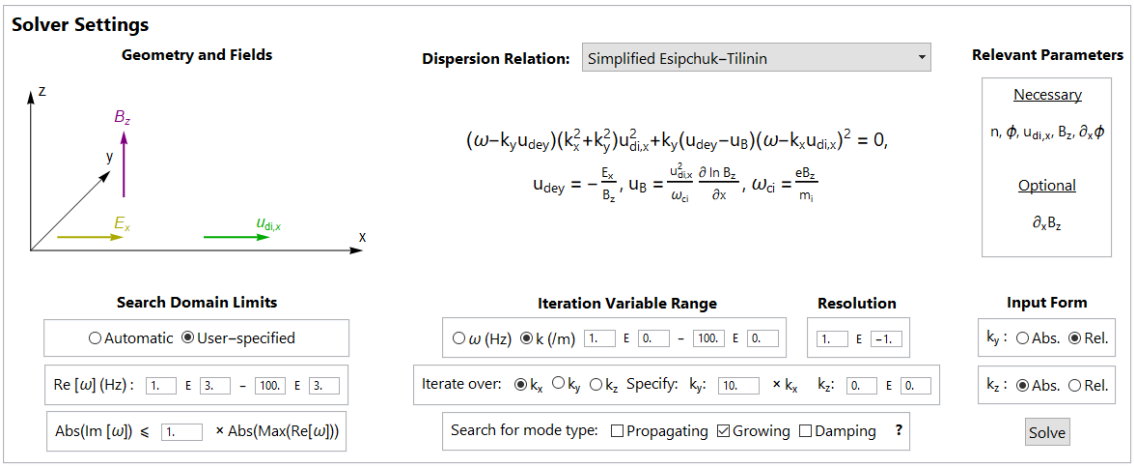

Figure D.3. Solver Settings for Esipchuk-Tilinin Example

The results of this analysis are displayed in the figures below. The "Binary Instability Spatializer" shows that unstable modes were found around $x = 44$ mm (see Fig. D.4). Clicking on the "Dominant Unstable Mode" buttons indicates that there are three grid points with unstable branches. Outputting the results and using the "Single Branch" plotter for the first (and only) branch of point $x = 44$ mm gives the dispersion relation shown in Fig. D.5.

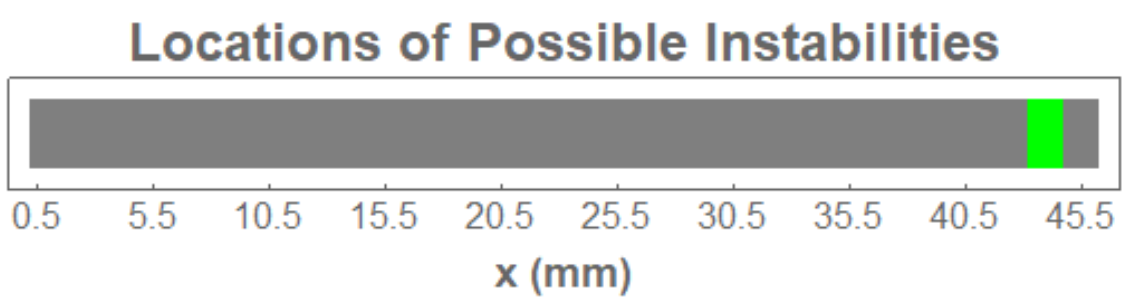

Figure D.4. Locations of Unstable Modes

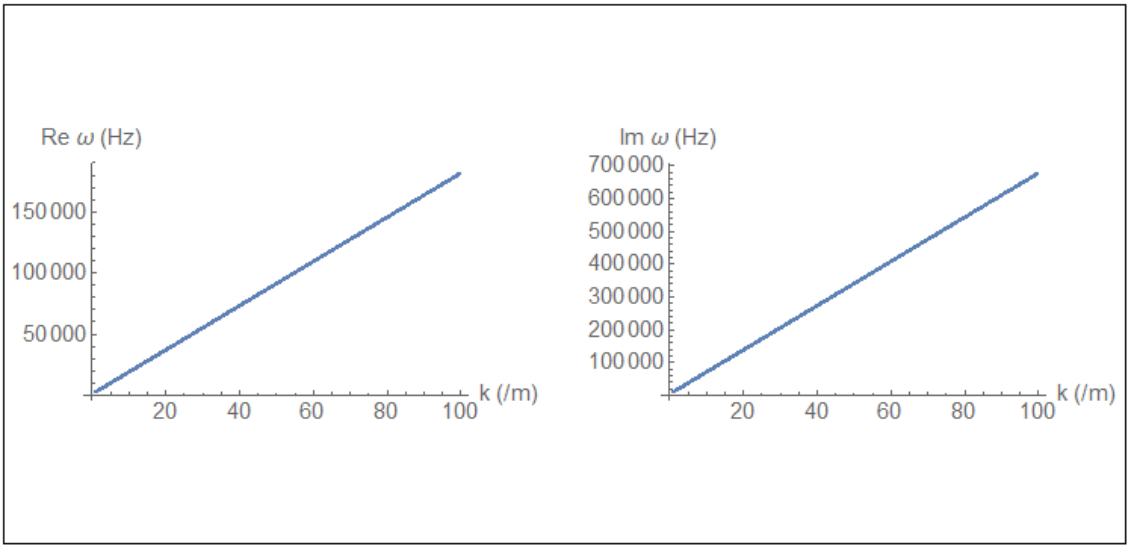

Figure D.5. Example Dispersion Relation for Branch at $x = 44$ mm.

D.2 User-Specified Dispersion Relation

Custom dispersion relations can be input using the template found in the "Custom_Relation.nb" file. This notebook should be edited and ran after the main "PRINCE.nb" notebook has been run. The "Custom Dispersion Relation" option in the drop down menu will use the function coded in the template notebook (though it will not display the function input by the user).

At the top of the document are the physical constants coded in PRINCE. Any other constants needed should be declared there with their values in SI units. Then there are three editing steps for the contents of the Block:

1. Store any input plasma parameter or gradient used in a local variable inside the function

2. Define additional local variables for calculated plasma parameters

3. Write the dispersion relation function

Any local variables used must first be declared inside the curly braces at the beginning of the Block. All lines of code must end with a semi-colon **except** the expression defining the dispersion relation, which must be at the very end of the Block.

The template file comes with example local variables and an arbitrary function declared. Note the format to access plasma parameters and gradient values, which uses the string aliases listed at the end of the template file for reference. The parameter values are accessed through the params structure while gradients are accesed through the gradMat structure. For example, to use the electron drift velocity in $\hat{\mathbf{x}}$ we would set a local variable equal to params["udex"]. Similarly, if we wanted to use the gradient of neutral density in $\hat{\mathbf{z}}$ we would set a local variable equal to gradMat["n0", "z"]. Note that the quotes around the arguments passed to params and gradMat are necessary since the aliases should be strings.

For help implementing any mathematical functions in the expression for the dispersion relation please refer to the Mathematica documentation. Note that while PRINCE provides a framework to numerically investigate arbitrary functions, there is no guarantee that function evaluations will be quick or well-behaved numerically in the region of $(\omega, \mathbf{k})$-space surveyed.

Bibliography

[1] Vines, S. K., Allen, R. C., Anderson, B. J., Engebretson, M. J., Fuselier, S. A., Russell, C. T., Strangeway, R. J., Ergun, R. E., Lindqvist, P. A., Torbert, R. B., and Burch, J. L., "EMIC Waves in the Outer Magnetosphere: Observations of an Off-Equator Source Region," *Geophysical Research Letters*, Vol. 46, 2019, pp. 5707–5716.

[2] Ram, A. K., Bers, A., and Benisti, D., "Ionospheric ion acceleration by multiple electrostatic waves," *Journal of Geophysical Research: Space Physics*, Vol. 103, No. A5, 1998, pp. 9431–9440.

[3] Khotyaintsev, Y. V., Graham, D. B., Norgren, C., and Vaivads, A., "Collisionless Magnetic Reconnection and Waves: Progress Review," *Frontiers in Astronomy and Space Sciences*, Vol. 6, No. 70, 2019, pp. 1–20.

[4] Chen, Q., Otto, A., and Lee, L. C., "Tearing instability, Kelvin-Helmholtz instability, and magnetic reconnection," Vol. 102, No. A1, 1997, pp. 151–161.

[5] Boswell, R. W. and Chen, F. F., "Helicons-The Early Years," *IEEE Transactions on Plasma Science*, Vol. 25, No. 6, 1997, pp. 1229–1244.

[6] Chabert, P. and Braithwaite, N., *Physics of Radio-Frequency Plasmas*, Cambridge University Press, New York, 2014.

[7] Yamamoto, T., Imai, T., Shimada, M., Suzuki, N., Maeno, M., Konoshima, S., Fujii, T., Uehara, K., Nagashima, T., Funahashi, A., and Fujisawa, N., "Experimental Observation of the rf-Driven Current by the Lower-Hybrid Wave in a Tokamak," *Physical Review Letters*, Vol. 45, No. 9, 1980, pp. 716–719.

[8] Cairns, R. A., *Radiofrequency Heating of Plasmas*, A. Hilger, Bristol, England, 1991.

[9] Hutchinson, I. H., *Principles of Plasma Diagnostics*, Cambridge University Press, New York, 2002.

[10] Surko, C. M. and Slusher, R. E., "Waves and Turbulence in a Tokamak Fusion Plasma," *Science*, Vol. 221, No. 4613, 1983, pp. 817–822.

[11] Choueiri, E. Y., "Plasma Oscillations in Hall Thrusters," *Physics of Plasmas*, Vol. 8, No. 4, 2001, pp. 1411–1426.

[12] Jahn, R. G., *Physics of Electric Propulsion*, Dover Publications, Inc., Mineola, New York, 2006.

[13] Cappelli, M. A., Meezan, N. B., and Gascon, N., "Transport physics in Hall plasma thrusters," *40th AIAA Aerospace Sciences Meeting and Exhibit*, No. January, Reno, NV, 2002, pp. AIAA–2002–485.

[14] Janes, G. S. and Lowder, R. S., "Anomalous Electron Diffusion and Ion Acceleration in a Low-Density Plasma," *The Physics of Fluids*, Vol. 9, No. 6, 1966.

[15] Adam, J. C., Boeuf, J.-P., Dubuit, N., Dudeck, M., Garrigues, L., Grésillon, D. M., Héron, A., Hagelaar, G. J. M., Kulaev, V., Lemoine, N., Mazouffre, S., Perez Luna, J., Pisarev, V., and Tsikata, S., "Physics, simulation and diagnostics of Hall effect thrusters," *Plasma Physics and Controlled Fusion*, Vol. 50, No. 12, 2008, pp. 124041.

[16] Heéron, A. and Adam, J. C., "Anomalous conductivity in Hall thrusters: Effects of the non-linear coupling of the electron-cyclotron drift instability with secondary electron emission of the walls," *Physics of Plasmas*, Vol. 20, No. 8, 2013, pp. 82313.

[17] Spektor, R., "Quasi-Linear Analysis Of Anomalous Electron Mobility Inside A Hall Thruster," *30th International Electric Propulsion Conference*, Florence, Italy, 2007, pp. 1–10.

[18] Martorelli, R., Lafleur, T., Bourdon, A., and Chabert, P., "Comparison between ad-hoc and instability-induced electron anomalous transport in a 1D fluid simulation of Hall-effect thruster," *Physics of Plasmas*, Vol. 26, No. 8, 2019.

[19] Mikellides, I. G. and Lopez Ortega, A., "Challenges in the development and verification of first-principles models in Hall-effect thruster simulations that are based on anomalous resistivity and generalized Ohm's law," *Plasma Sources Science and Technology*, Vol. 28, No. 1, 2019.

[20] Jorns, B. A., Mikellides, I. G., and Goebel, D. M., "Ion acoustic turbulence in a 100-A LaB6 hollow cathode," *Physical Review E*, Vol. 90, No. 6, 2014, pp. 063106.

[21] Litvak, A. A. and Fisch, N. J., "Resistive Instabilities in Hall Current Plasma Discharge," *Physics of Plasmas*, Vol. 8, No. 2, 2001, pp. 648–651.

[22] Lobbia, R. B., *A Time-resolved Investigation of the Hall Thruster Breathing Mode*, Ph.D. thesis, University of Michigan, 2010.

[23] Ellison, C. L., Raitses, Y., and Fisch, N. J., "Cross-field electron transport induced by a rotating spoke in a cylindrical Hall thruster," *Physics of Plasmas*, Vol. 19, No. 1, 2012.

[24] Koshkarov, O., Smolyakov, A., Raitses, Y., and Kaganovich, I., "Self-Organization, Structures, and Anomalous Transport in Turbulent Partially Magnetized Plasmas with Crossed Electric and Magnetic Fields," *Physical Review Letters*, Vol. 122, No. 18, 2019, pp. 185001.

[25] Cavalier, J., Lemoine, N., Bonhomme, G., Tsikata, S., Honoré, C., and Grésillon, D., "Hall thruster plasma fluctuations identified as the E x B electron drift instability: Modeling and fitting on experimental data," *Physics of Plasmas*, Vol. 20, No. 8, 2013, pp. 082107.

[26] Lafleur, T., Baalrud, S. D., and Chabert, P., "Theory for the anomalous electron transport in Hall effect thrusters. I. Insights from particle-in-cell simulations," *Physics of Plasmas*, Vol. 23, No. 5, 2016, pp. 053502.

[27] Brown, Z. A. and Jorns, B. A., "Spatial evolution of plasma waves in the acceleration region and near-field of a magnetically shielded hall thruster," *2018 Joint Propulsion Conference*, 2018, pp. 1–12.

[28] Yoshikawa, S. and Rose, D. J., "Anomalous Diffusion of a Plasma across a Magnetic Field," *Physics of Fluids*, Vol. 5, No. May 2015, 1962, pp. 334.

[29] Spitzer, L., *Physics of Fully Ionized Gases*, Dover Publications, Inc., Mineola, New York, 2006.

[30] Liewer, P. C. and Krall, N. A., "Self-consistent approach to anomalous resistivity applied to theta pinch experiments," *The Physics of Fluids*, Vol. 16, No. 11, 1973.

[31] Stix, T. H., *Waves in Plasmas*, Springer, New York, 1992.

[32] Chen, F. F., *Introduction to Plasma Physics*, Plenum Press, New York, 1974.

[33] Goldston, R. J. and Rutherford, P. H., *Introduction to Plasma Physics*, Taylor & Francis Group, New York, 1995.

[34] Frias, W., Smolyakov, A. I., Kaganovich, I. D., and Raitses, Y., "Long wavelength gradient drift instability in Hall plasma devices. I. Fluid Theory," *Physics of Plasmas*, Vol. 19, No. 5, 2012, pp. 052108.

[35] Lominadze, D. G., *Cyclotron Waves in Plasma*, Pergamon Press, Oxford, 1981.

[36] Goree, J., Ono, M., and Wong, K. L., "Observation of the backward electrostatic ion-cyclotron wave," *Physics of Fluids*, Vol. 28, No. 9, 1985.

[37] Beall, J. M., Kim, Y. C., and Powers, E. J., "Estimation of wavenumber and frequency spectra using fixed probe pairs," *Journal of Applied Physics*, Vol. 53, No. 6, 1982, pp. 3933–3940.

[38] Ohnuma, T., Miyake, S., Sato, T., and Watari, T., "Propagation of Electrostatic ion Waves Near Ion Cyclotron Harmonics," *Physical Review Letters*, Vol. 26, No. 10, 1970, pp. 541.

[39] Skiff, F. and Anderegg, F., "Direct Observation of Plasma Dielectric Motion," *Physical Review Letters*, Vol. 59, No. 8, 1987, pp. 896–899.

[40] Spektor, R. and Choueiri, E. Y., "Excitation and propagation of Electrostatic Ion Cyclotron waves in rf-sustained plasmas of interest to propulsion research," *40th AIAA/ASME/SAE/ASEE Joint Propulsion Conference and Exhibit*, Fort Lauderdale, FL, 2004.

[41] Lieberman, M. A. and Lichtenberg, A. J., *Principles of Plasma Discharges and Materials Processing*, John Wiley & Sons, New York, 2005.

[42] Boswell, R. W., "Plasma production using a standing helicon wave," *Physics Letters A*, Vol. 33, No. 7, 1970, pp. 457–458.

[43] Kline, J. L., Scime, E. E., Keiter, P. a., Balkey, M. M., and Boivin, R. F., "Ion heating in the HELIX helicon plasma source," *Physics of Plasmas*, Vol. 6, No. 12, 1999, pp. 4767.

[44] Ikezi, H. and Taylor, R. J., "Observation of First-Order Ion Energy Distribution in Ion-Acoustic Waves," *Physical Review Letters*, Vol. 22, No. 18, 1969, pp. 923–925.

[45] Jorns, B., Sorenson, R., and Choueiri, E., "Variable dual-frequency electrostatic wave launcher for plasma applications," *Review of Scientific Instruments*, Vol. 82, No. 12, 2011.

[46] Smith, D. E., Powers, E. J., and Caldwell, G. S., "Fast-Fourier-transform spectral-analysis techniques as a plasma fluctuation diagnostic tool," *IEEE Transactions on Plasma Science*, Vol. 2, No. 4, 1974, pp. 261–272.

[47] Albarède, L., Mazouffre, S., Bouchoule, A., and Dudeck, M., "Low-frequency electron dynamics in the near field of a Hall effect thruster," *Physics of Plasmas*, Vol. 13, No. 6, 2006, pp. 1–7.

[48] Lazurenko, A., Dudok De Wit, T., Cavoit, C., Krasnoselskikh, V., Bouchoule, A., and Dudeck, M., "Determination of the electron anomalous mobility through measurements of turbulent magnetic field in Hall thrusters," *Physics of Plasmas*, Vol. 14, No. 3, 2007.

[49] Stevens, J. E., Sowa, M. J., and Cecchi, J. L., "Helicon plasma source excited by a flat spiral coil," *Journal of Vacuum Science & Technology A: Vacuum, Surfaces, and Films*, Vol. 13, No. 5, 1995, pp. 2476–2482.

[50] Smy, P. R., "The use of Langmuir probes in the study of high pressure plasmas," *Advances in Physics*, Vol. 25, No. 5, 1976, pp. 517–553.

[51] Lazurenko, A., Coduti, G., Mazouffre, S., and Bonhomme, G., "Dispersion relation of high-frequency plasma oscillations in Hall thrusters," *Physics of Plasmas*, Vol. 15, No. 3, 2008, pp. 34502.

[52] Stern, R. A. and Johnson, J. A., "Plasma Ion Diagnostics Using Resonant Fluorescence," *Phys. Rev. Lett.*, Vol. 34, No. 25, 1975, pp. 1548–1551.

[53] Severn, G. D., Edrich, D. A., and McWilliams, R., "Argon ion laser-induced fluorescence with diode lasers," *Review of Scientific Instruments*, Vol. 69, No. 1, 1998, pp. 10.

[54] Sarfaty, M., De Souza-Machado, S., and Skiff, F., "Direct determination of ion wave fields in a hot magnetized and weakly collisional plasma," *Physics of Plasmas*, Vol. 3, No. 12, 1996, pp. 4316–4324.

[55] Jorns, B. A., *Experimental Characterization of Plasma Heating with Beating Electrostatic Waves*, Ph.D. Dissertation, Princeton University, 2012.

[56] Jorns, B. A. and Choueiri, E. Y., "Stochastic Threshold for Ion Heating with Beating Electrostatic Waves," *Physical Review Letters*, Vol. 110, No. 24, 2013, pp. 1–5.

[57] Saloman, E. B., "Energy levels and observed spectral lines of ionized argon, Ar II through Ar XVIII," *Journal of Physical and Chemical Reference Data*, Vol. 39, No. 3, 2010.

[58] Moore, C. E. and Merrill, P. W., "Partial Grotrian Diagrams of Astrophysical Interest," 1968.

[59] Hill, D. N., Fornaca, S., and Wickham, M. G., "Single frequency scanning laser as a plasma diagnostic," *Review of Scientific Instruments*, Vol. 54, No. 3, 1983, pp. 309–314.

[60] Hargus, W. A. and Cappelli, M. A., "Laser-induced fluorescence measurements of velocity within a Hall discharge," *Applied Physics B: Lasers and Optics*, Vol. 72, No. 8, 2001, pp. 961–969.

[61] Keesee, A. M., Scime, E. E., and Boivin, R. F., "Laser-induced fluorescence measurements of three plasma species with a tunable diode laser," *Review of Scientific Instruments*, Vol. 75, No. 10, 2004, pp. 4091–4093.

[62] Verreycken, T., Van Der Horst, R. M., Baede, A. H., Van Veldhuizen, E. M., and Bruggeman, P. J., "Time and spatially resolved LIF of OH in a plasma filament in atmospheric pressure HeH 2O," *Journal of Physics D: Applied Physics*, Vol. 45, No. 4, 2012.

[63] Kline, J. L., Franck, C., and Spangler, R., "First order perturbed velocity distribution theory and measurement," Tech. rep., West Virginia University, 2000.

[64] Wagner, H. P., Kaeppeler, H. J., and Auweter-Kurtz, M., "Instabilities in MPD thruster flows: 1. Space charge instabilities in unbounded and inhomogeneous plasmas," *Journal of Physics D: Applied Physics*, Vol. 31, No. 5, 1998, pp. 519–528.

[65] Frias, W., Smolyakov, A. I., Kaganovich, I. D., and Raitses, Y., "Long wavelength gradient drift instability in Hall plasma devices. II. Applications," *Physics of Plasmas*, Vol. 20, No. 5, 2013, pp. 052108.

[66] Holzhauer, E. and Massig, J. H., "An analysis of optical mixing in plasma scattering experiments," *Plasma Physics*, Vol. 20, No. 9, 1978, pp. 867–877.

[67] Tsikata, S., Lemoine, N., Pisarev, V., and Grésillon, D. M., "Dispersion relations of electron density fluctuations in a Hall thruster plasma, observed by collective light scattering," *Physics of Plasmas*, Vol. 16, No. 3, 2009.

[68] Tsikata, S., Honoré, C., Lemoine, N., and Grésillon, D. M., "Three-dimensional structure of electron density fluctuations in the Hall thruster plasma: E x B mode," *Physics of Plasmas*, Vol. 17, No. 11, 2010.

[69] Delves, L. M. and Lyness, J. N., "A Numerical Method for Locating the Zeros of an Analytic Function," *Mathematics of Computation*, Vol. 21, 1967, pp. 543–560.

[70] Ioakimidis, N. I. and Anastasselou, E. G., "A modification of the delves-lyness method for locating the zeros of analytic functions," *Journal of Computational Physics*, Vol. 59, No. 3, 1985, pp. 490–492.

[71] Pan, V. Y., "Solving a Polynomial Equation: Some History and Recent Progress," Vol. 39, No. 2, 1997, pp. 187–220.

[72] Kowalczyk, P., "Complex Root Finding Algorithm Based on Delaunay Triangulation," *ACM Transactions on Mathematical Software*, Vol. 41, No. 3, 2015.

[73] Hittle, D. C. and Bishop, R., "An Improved Root-Finding Procedure for Use in Calculating Transient Heat Flow through Multilayered Slabs," *International Journal of Heat and Mass Transfer*, Vol. 26, No. 11, 1983, pp. 1685–1693.

[74] Dunkel, J. and Weber, S., "Stochastic root finding and efficient estimation of convex risk measures," *Operations Research*, Vol. 58, No. 5, 2010, pp. 1505–1521.

[75] Chun, S. and Kwasinski, A., "Analysis of classical root-finding methods applied to digital maximum power point tracking for sustainable photovoltaic energy generation," *IEEE Transactions on Power Electronics*, Vol. 26, No. 12, 2011, pp. 3730–3743.

[76] Bagatur, T., "Modified Newton–Raphson Solution for Dispersion Equation of Transition Water Waves," *Journal of Coastal Research*, Vol. 23, No. 6, 2007, pp. 1588–1592.

[77] Dubbelday, P. S., "Application of a New Complex Root-Finding Technique to the Dispersion Relations for Elastic Waves in a Fluid-Loaded Plate," *SIAM Journal of Applied Mathematics*, Vol. 43, No. 5, 1983, pp. 1127–1139.

[78] Newman, J. N., "Numerical solutions of the water-wave dispersion relation," *Applied Ocean Research*, Vol. 12, No. 1, 1990, pp. 14–18.

[79] Uginčius, P. and Überall, H., "Creeping-Wave Analysis of Acoustic Scattering by Elastic Cylindrical Shells," *The Journal of the Acoustical Society of America*, Vol. 43, No. 5, 1968, pp. 1025–1035.

[80] Uginčius, P., "Creeping-Wave Analysis of Acoustic Scattering by Elastic Cylindrical Shells," Tech. rep., Dahlgren, Virginia, 1968.

[81] Hamming, R. W., *Introduction to Applied Numerical Analysis*, McGraw-Hill Book Company, New York, 1971.

[82] Press, W., Teukolsky, S. A., Vetterling, W. T., and Flannery, B. P., *Numerical Recipes: The Art of Scientific Computing*, Cambridge University Press, New York, 2007.

[83] Tataronis, J. A. and Crawford, F. W., "Cyclotron harmonic wave propagation and instabilities I. Perpendicular propagation," *Journal of Plasma Physics*, Vol. 4, No. 2, 1970, pp. 231–248.

[84] Tataronis, J. A. and Crawford, F. W., "Cyclotron harmonic wave propagation and instabilities II. Oblique propagations," *Journal of Plasma Physics*, Vol. 4, No. 2, 1970, pp. 249–264.

[85] Pfeiffer, W., "A graphical method for finding complex roots and its application to plasma physics problems," *Journal of Computational Physics*, Vol. 33, No. 3, 1979, pp. 397–404.

[86] Choueiri, E. Y., *Electron-Ion Steaming Instabilities of an Electromagnetically Accelerated Plasma*, Ph.D. Dissertation, Princeton University, 1991.

[87] EPPDyL, "DART Tool: Dispersion relation solver," 2012.

[88] Rojas Mata, S. and Choueiri, E. Y., "Plasma Dispersion Relation Measurements through Active Injection of Wave Packets," *36th International Electric Propulsion Conference*, Vienna, 2019.

[89] Hirose, A., Alexeff, I., and Jones, W. D., "Dispersion Measurements of Electrostatic Ion Waves in a Uniform Magnetic Field," *Physics of Fluids*, Vol. 13, No. 8, 1970, pp. 2039.

[90] Welch, P. D., "The Use of Fast Fourier Transform for the Estimation of Power Spectra: A Method Based on Time Averaging Over Short, Modified Periodograms," *IEEE Transactions on Audio and Electroacoustics*, Vol. 15, No. 2, 1967, pp. 2077.

[91] Stoica, P. and Moses, R., *Spectral Analysis of Signals*, Prentice Hall, Inc., Upper Saddle River, 2009.

[92] Brandt, A., *Noise and Vibration Analysis: Signal Analysis and Experimental Procedures*, John Wiley & Sons, Inc., UK, 2011.

[93] Choueiri, E. Y., Kelly, A. J., and Jahn, R. G., "Current Driven Instabilities of an Electromagnetically Accelerated Plasma," *20th International Electric Propulsion Conference*, 1988.

[94] Kolodziej, K. E., "Comb generator design for SWaP-constrained applications," *IEEE Radio and Wireless Symposium, RWS*, Vol. 2016-March, No. 1, 2016, pp. 200–203.

[95] Spektor, R., *Ion Energization By a Pair of Beating Electrostatic Waves*, Ph.D. Dissertation, Princeton University, 2006.

[96] Keiter, P. A., Scime, E. E., and Balkey, M. M., "Frequency dependent effects in helicon plasmas," *Physics of Plasmas*, Vol. 4, No. 7, 1997, pp. 2741–2747.

[97] Ault, E. R. and Ikezi, H., "Propagation of Ion Cyclotron Harmonic Wave," *Physics of Fluids*, Vol. 13, No. 11, 1970, pp. 2874.

[98] Lominadze, D. G. and Stepanov, K. N., "Induction of Low-Frequency Longitudinal Oscillations in a Plasma Contained in a Magnetic Field," *Soviet Physics Technical Physics*, Vol. 9, No. 10, 1965, pp. 1408.

[99] Spektor, R. and Choueiri, E. Y., "Measurements of Ion Energization by a Pair of Beating Electrostatic Ion Cyclotron Waves," *International Electric Propulsion Conference 2005*, 2005, pp. 1–11.

[100] Hirose, A., Alexeff, I., Jones, W. D., Krall, N. A., and Montgomery, D., "Landau damping of electrostatic ion waves in a uniform magnetic field," *Physics Letters A*, Vol. 29, No. 1, 1969, pp. 31–32.

[101] Pozar, D. M., *Microwave Engineering*, John Wiley & Sons, Inc., USA, 1998.

[102] Bevington, P. R. and Robinson, D. K., *Data Reduction and Error Analysis for the Physical Sciences*, McGraw-Hill, Boston, 2003.

[103] Brown, J. W. and Churchill, R. V., *Complex Variables and Applications*, McGraw-Hill, New York, 2009.

[104] Martin, T. J., "Root finding and the solution of dispersion equations," Tech. rep., Culham Laboratory, Abingdon Berkshire, UK, 1971.

[105] Rojas Mata, S., Choueiri, E. Y., Jorns, B. A., and Spektor, R., "PRINCE: A Software Tool for Characterizing Waves and Instabilities in Plasma Thrusters," *52nd AIAA/SAE/ASEE Joint Propulsion Conference*, Salt Lake City, UT, 2016.

[106] Esipchuk, Y. B. and Tilinin, G. N., "Drift instability in a Hall-current plasma accelerator," *Sov. Phys. Tech. Phys.*, Vol. 21, No. 4, 1976, pp. 417–423.

[107] Bishaev, A. M. and Kim, V., "Local plasma properties in a Hall-current accelerator with an extended acceleration zone," *Soviet Physics Technical Physics*, Vol. 23, No. 9, 1978, pp. 1055–1057.